

---


Electronic Theses and Dissertations, 2004-2019

---

2014

## Nanocomposite Coating Mechanics via Piezospectroscopy

Gregory Freihofer  
*University of Central Florida*

 Part of the [Mechanical Engineering Commons](#)  
Find similar works at: <https://stars.library.ucf.edu/etd>  
University of Central Florida Libraries <http://library.ucf.edu>

This Doctoral Dissertation (Open Access) is brought to you for free and open access by STARS. It has been accepted for inclusion in Electronic Theses and Dissertations, 2004-2019 by an authorized administrator of STARS. For more information, please contact [STARS@ucf.edu](mailto:STARS@ucf.edu).

---

### STARS Citation

Freihofer, Gregory, "Nanocomposite Coating Mechanics via Piezospectroscopy" (2014). *Electronic Theses and Dissertations, 2004-2019*. 1344.  
<https://stars.library.ucf.edu/etd/1344>

NANOCOMPOSITE COATING MECHANICS *via* PIEZOSPECTROSCOPY

by

GREGORY J. FREIHOFER

B.S. University of Central Florida, 2010

M.S. University of Central Florida, 2011

A dissertation submitted in partial fulfillment of the requirements  
for the degree of Doctor of Philosophy  
in the Department of Mechanical and Aerospace Engineering  
in the College of Engineering and Computer Science  
at the University of Central Florida  
Orlando, Florida

Summer Term  
2014

Major Professor:  
Seetha Raghavan

© 2014 by Gregory J. Frehofer

## ABSTRACT

Coatings utilizing the piezospectroscopic (PS) effect of alpha alumina ( $\alpha\text{-Al}_2\text{O}_3$ ) could enable on the fly stress sensing for structural health monitoring applications. While the PS effect has been historically utilized in several applications, here by distributing the photo-luminescent material in nanoparticle form within a matrix, a stress sensing coating is created. Parallel to developing PS coatings for stress sensing, the multi-scale mechanics associated with the observed PS response of nanocomposites and their coatings has been applied to give material property measurements, providing an understanding of particle reinforced composite behavior.

Understanding the nanoparticle-coating-substrate mechanics is essential to interpreting the spectral shifts for stress sensing of structures. In the past, methods to experimentally measure the mechanics of these embedded nano inclusions have been limited, and much of the design of these composites depend on computational modeling and bulk response from mechanical testing. The PS properties of Chromium doped  $\text{Al}_2\text{O}_3$  allow for embedded inclusion mechanics to be revisited with unique experimental setups that probe the particles state of stress under applied load to the composite. These experimental investigations of particle mechanics will be compared to the Eshelby theory and its derivative theories in addition to the nanocomposite coating mechanics. This work discovers that simple nanoparticle load transfer theories are adequate for predicting PS properties in an intermediate volume fraction range.

With fundamentals of PS nanocomposites established, the approach was applied to selected experiments to prove its validity. In general it was observed that the elastic

modulus values calculated from the PS response were similar to that observed from macroscale strain measurements such as a strain gage. When simple damage models were applied to monitor the elastic modulus, it was observed that the rate of decay for the elastic modulus was much higher for the PS measurements than for the strain gage.

A novel experiment including high resolution PS maps with secondary strain maps from digital image correlation is reviewed on an open hole tension, composite coupon. The two complementary measurements allow for a unique PS response for every location around the hole with a spatial resolution of 400 microns. Progression of intermediate damage mechanisms was observed before digital image correlation indicated them. Using the PS nanocomposite model, elastic modulus values were calculated. Introducing an elastic degradation model with some plastic deformation allows for estimation of material properties during the progression of failure.

This work is part of a continuing effort to understand the mechanics of a stress sensing PS coating. The mechanics were then applied to various experimental data that provided elastic property calculations with high resolution. The significance is in the experimental capture of stress transfer in particulate composites. These findings pave the way for the development of high resolution stress-sensing coatings.

*I would like to dedicate this work to everyone who supported me along this journey*

## ACKNOWLEDGMENTS

I would like to acknowledge several collaborators, colleagues and friends who assisted with me overcoming the challenges in completing this body of work. I would first like to thank my advisor for supporting me and assigning me this research project. I would like to Thank Amanda Stevenson and Emercan Ergin, whose old data proved useful in application to this work. I would like to thank Amy Van-Newkirk and Clemence Jollivet at CREOL for providing support on various tasks. I would like to thank Ankur Gupta and others at AMPAC for assisting in fabrication and characterization of plasma sprayed samples. I would like to thank our collaborators at The Boeing Company for providing samples and collecting digital image correlation data. I would like to thank Elantas PDG. for fabrication of high quality alumina nanocomposite coatings. This material is based upon work supported by the National Science Foundation under Grant No 1130837.

# TABLE OF CONTENTS

LIST OF FIGURES . . . . .	xi
LIST OF TABLES . . . . .	xix
1 INTRODUCTION . . . . .	1
1.1 Developing Piezospectroscopy . . . . .	2
1.2 Alumina nanocomposites . . . . .	4
1.2.1 Alumina Coatings . . . . .	6
1.3 Piezospectroscopy . . . . .	7
1.4 Damage Mechanics with Piezospectroscopy . . . . .	10
2 MECHANICS OF PIEZOSPECTROSCOPIC NANOCOMPOSITES . . . . .	12
2.1 Experimental Background . . . . .	12
2.2 Piezospectroscopic Nanocomposite Mechanics . . . . .	14
2.3 Analytical formulation . . . . .	16
2.4 Equivalent Composite Property Models Integrated with Dilute-Eshelby . . . . .	21
2.5 Finite Element Analysis . . . . .	28
2.5.1 Problem Statement . . . . .	29
2.5.2 Irregular particle . . . . .	33
2.5.3 Interacting particles . . . . .	34



2.5.4	Interface effects . . . . .	35
2.5.5	Microcracks . . . . .	37
2.6	Conclusion . . . . .	40
3	COATING AND DAMAGE MECHANICS FOR PIEZOSPECTROSCOPIC MA- TERIALS . . . . .	41
3.1	The Mutli-Scale Problem of PS Nanocomposite Coatings . . . . .	41
3.2	Fundamentals of Piezospectroscopy . . . . .	42
3.3	Piezospectroscopic Coating Mechanics . . . . .	44
3.3.1	Coating Mechanics for 1-D systems . . . . .	44
3.3.2	Coating Mechanics for 2-Dimensional Systems . . . . .	47
3.4	Mechanical Property Measurements with Piezospectroscopy . . . . .	51
3.4.1	Damage Monitoring with the PS response . . . . .	54
3.5	Conclusion . . . . .	58
4	PIEZOSPECTROSCOPY OF PLASMA SPRAY COATINGS . . . . .	59
4.1	Introduction . . . . .	60
4.2	Experimental . . . . .	61
4.3	Results . . . . .	63
4.4	Elastic Modulus of the Damaged Coating . . . . .	68
4.5	Conclusion . . . . .	71

5	PIEZOSPECTROSCOPY OF COATED OPEN HOLE TENSION SAMPLES	72
5.1	Experimental Setup . . . . .	72
5.2	Results . . . . .	75
5.2.1	Qualitative Inspection . . . . .	76
5.2.2	Inspection of the Damaged Zone . . . . .	78
5.2.3	Correlation to Progressive Composite Failure . . . . .	80
5.3	Applied Damage Mechanics . . . . .	82
5.3.1	Degradation and Plastic Deformation . . . . .	83
5.3.2	Material Property Calculations . . . . .	86
5.4	Modeling the PS response . . . . .	89
5.4.1	Yield and Damage Functions . . . . .	90
5.4.2	The Secant PS State . . . . .	94
5.5	Conclusion . . . . .	96
6	CONCLUSION . . . . .	97
	APPENDIX A CURVE FITTING . . . . .	102
A.1	The pseudo-Voigt function . . . . .	103
A.2	Curve fitting Algorithm Architecture . . . . .	104
	APPENDIX B IMAGE PROCESSING . . . . .	110
B.1	Signal to Noise Ratio . . . . .	110

B.2 Open Hole Tension PS-DIC map Alignment . . . . .	112
LIST OF REFERENCES . . . . .	115

## LIST OF FIGURES

2.1	(a) A schematic representing hyperspectral imaging of a PS nanocomposite under compressive loading, (b) corresponding peak position downshifts with compressive loading, and (c) the composite PS coefficient ( $\Pi_c$ ) relating a peak position shift with applied stress. . . . .	13
2.2	The Piezospectroscopic relationships for different loading conditions of a PS constituent. . . . .	15
2.3	The theoretical Eshelby [15, 26] model predicting the PS properties for a composite and compared to experimental data from the works of Ergin [24] and Stevenson [92]. . . . .	20
2.4	This is the iterative loop developed originally by Kim et. al [53] to predict the elastic properties of composites. Here, the iterative loop is used to calculate the PS properties for varying volume fractions. . . . .	22
2.5	The PS properties as predicted by the non-dilute Eshelby [26, 15] compared to the results from Kim et. al [53] and experimental data from the works of Ergin [24] and Stevenson [92]. . . . .	23
2.6	A modified Esheby Scheme which has the potential to combine any material properties prediction model for composites. . . . .	24
2.7	Experimental data from alumina epoxy nanocomposites from the works of Ergin [24] compared to the estimated composite properties of Mori-Tanaka and Kim. . . . .	26

2.8	The equivalent composite properties model utilizing the Dilute Eshelby [15] compared to Kim’s method [53], Non-Dilute Eshelby, and experimental data from Ergin [24] and Stevenson [92]. . . . .	27
2.9	Modifying an idealized RVE by introducing a variety of different micro-structural features. . . . .	28
2.10	(a) The RVE for an alumina nanocomposite. (b) Details are presented for constructing the interface and constraints and (c) the loads and boundary conditions, as well as (d) meshed assembly of the matrix and particle with the method of predicting the composite’s PS properties. (e) The stress ratio obtained from a 5% alumina volume fraction composite in an axisymmetric model simulated Eshelby stress ratio exactly. . . . .	30
2.11	(a) Stress Ratio results for varying volume fractions and different interface boundary conditions. (b) A Variety of models predicting volume fraction effects. . . . .	32
2.12	(a-b) A non circular particle generated using a Matlab algorithm which given rotation and irregularity. (b) Results are plotted for an irregular ~23% volume fraction composite with varying degrees of rotation. . . . .	34
2.13	(a) Different number and orientations of interacting particles with (b) the corresponding stress ratio increase with respect to the idealized FEM model.	35
2.14	(a) The effects of an isotropic interface on the stress ratio and (b) the RVE with simulated isotropic interfaces. . . . .	36

2.15	Straight cracks investigated in a (a) vertical and (b) horizontal configuration were (c) plotted with respect to the experimental data and the idealized FEM model for 5% volume fraction alumina. (d-f) Curved microcracks were investigated in terms of a few geometric parameters and (g) plotted with respect to the experimental data. . . . .	37
2.16	(a) Summary of the different microcrack configurations plotted with respect to volume fraction. (b) A closer look at the microcrack model that yielded a low stress ratio which correlates with lower volume fraction experimental data. . . . .	38
3.1	A series of illustrations that show the connection between the multi-scale problem for a PS nanocomposite coating. . . . .	42
3.2	(a) Strain based and (b) stress based PS responses for different secondary mechanical measurements from (c) a 1-D tensile test. . . . .	45
3.3	An element to perform a force balance in relating the PS shifts to coating mechanics. . . . .	46
3.4	An 2-D element to perform the interface relationships between the coating and substrate in relating the PS shifts to coating mechanics. . . . .	49
3.5	Experimental PS response and Mechanical response for varying volume fraction of alumina in epoxy nanocomposites from the work of Ergin [24].	52

3.6	(a) Composite modulus based from calculation of the PS response with uniaxial stress/strain, the load cell/strain gage response, and the analytical Mori-Tanaka solution [72]. (b) A schematic is shown to give a physical representation on the differences between the uni-axial stress and strain assumption used to calculate the composite modulus with the PS response.	54
3.7	(a) The initial and final PS states marked on the PS response to be a function of the elastic states. (b) The elastic degradation computed from the PS states in (a) using Equation 3.21. . . . .	56
3.8	The degradation of the elastic modulus calculated from both the load cell/strain gage and PS response data for each volume fraction. The mechanics was applied to data obtained in previous work [24]. . . . .	57
4.1	The coupled load frame and spectrometer probe setup (a), view of the gauge section (b), the tensile load cycle (c), peak shift distribution map before the third cycle begins (d), and a highlighted section of the load cycle with corresponding peak shift distribution maps (e). [29] . . . . .	62
4.2	FBG sensor stress on the coating surface (a) and the PL peak shift for R1 (b) for all three substrate thicknesses. The error bars represent one standard deviation of the peak shift in the mapped area. [29] . . . . .	64
4.3	SEM images of the APS $Al_2O_3$ coating on the 1/5 inch substrate with a cross sectional (a) and top surface (b) view. [29] . . . . .	65

4.4	The cyclic response of the peak shift with respect to substrate stress for the 1/8 inch (a), 1/4 inch (b), and the precycled 1/5 inch substrate (c). The first order PS coefficients for each substrate thickness as a function of cycle number (d). The error bars represent one standard deviation of the peak shift in the mapped area. [29] . . . . .	66
4.5	A schematic of the coating-substrate system and some insights into the micro-mechanical damage mechanisms suggested by the behavior of the PS response. [30] . . . . .	67
4.6	(a) A schematic illustrating the two sources of the elastic modulus measurements and (b) a comparison between the elastic modulus calculated from the two methods. . . . .	69
4.7	(a) Peak position photoluminescence map and (b) SEM images of the APS coating surface. . . . .	70
5.1	High spatial resolution intensity map quantifies coating dispersion. . . . .	73
5.2	(a) The load history plot indicating the displacement control holds. (b) Front side PS and (c) backside DIC data were collected on opposing faces. PS shift and biaxial strain ( $\epsilon_x + \epsilon_y$ ) maps are shown for 96% failure load. The hood around the optical probe was implemented to reduce the noise resulting from room lights. . . . .	74
5.3	The evolution of PS shift and biaxial strain maps for half of the open hole tension sample with percent failure loads listed. . . . .	77



5.4	PS shift maps for a region close to the open hole which was highly damaged during loading. The percentage of failure load is indicated to the right of each map. . . . .	78
5.5	(a) Selected PS shift maps of highlighted region for further analysis. (b) The PS shifts of selected highlighted regions plotted with respect to distance from open hole. (c) PS gradient distance from pixel count and across the highlighted region. . . . .	79
5.6	(a) The PS shift map and (b) DIC biaxial strain map for 92% failure load. (c) The PS response for the marked region in (a) and (b). These figures were created with a post processing procedure described in the Appendix. . . . .	81
5.7	(a) The simulation of the unloading curves for a PS response using purely elastic degradation and (b) elastic degradation with plastic deformation until the max PS shift. . . . .	83
5.8	(a-d) Selected loads for the elastic degradation model and (e-h) the elastic degradation model with plastic deformation. Percent failure loads are indicated for each pair of maps and all maps share the same color scale. . . . .	86
5.9	(a) The PS state map for 20% failure load. (b) The list of assumptions which allow for the creation of (c) an elastic modulus map of the substrate. . . . .	87
5.10	The substrate's elastic modulus maps for all the failure load increments. . . . .	89
5.11	(a-d) are the PS responses for selected regions as indicated on the (e) PS shift map and (f) DIC biaxial strain map for 96% failure load. . . . .	91
5.12	(a-d) are the PS responses for selected regions as indicated in Figure 5.11. . . . .	93

5.13	The variable maps and respected histograms for the (a) composite's PS coefficient, (b) yield strain, (c) linear dimensionless constant, and (d) the exponential dimensionless constant. . . . .	94
5.14	The secant PS state of the damage function. The damage function was a linear fit as discussed in the previous section, and can be represented with a single map. . . . .	95
A.1	A block diagram for the current curve fitting procedure, the curve fitting algorithm is decomposed into the 4 main subsections. . . . .	105
A.2	The "upperwave" of the R-line doublet which contains the critical points to define in order to initialize the fitting process. . . . .	106
A.3	The baseline removal process shown which utilized the determination of the lower and upper bounds in indexing. . . . .	108
B.1	(a-c) The signal to noise ratio outputs for 3 locations next to the open hole. (d) An intensity map of the sample with an inset showing the three locations of interest. (e) A logic map created by spectra which passed the SNR threshold. . . . .	111
B.2	(a) A schematic demonstrating the movement of the hole with respect to the detector's field of view. (b) A logic map converted into an array of boundary points which define the hole. The points are then used to fit a circle and track the movement of the hole. . . . .	112

B.3 (a) An illustration demonstrating the change in size and shape of the hole under increasing loads. (b) A PS map before and after the regions close to the open hole were removed. . . . . 114

## LIST OF TABLES

2.1	Experimental PS coefficients ( $\Pi_c$ ) for R1 and R2 peaks [92, 24] . . . . .	14
2.2	Model type and matrix-particle interface boundary conditions . . . . .	31

## CHAPTER 1 INTRODUCTION

This work was part of a continuing effort to develop piezospectroscopic (PS) coatings, based on stress-sensitive photo-luminescent spectral peaks for structural health monitoring which is applicable to a wide range of industries. This effort also includes an investigation of mechanics for composites with embedded PS nanoparticles and experimental testing for validation. Some newly developed relationships in the present work suggest the possibility to use the PS response as a method of determining material properties. This draws more attention to the development of smart composite coatings, which could someday supply a non-invasive method of determining a damaged zone, so a repair can be made accordingly.

The impact of this work is in its unique approach of combining PS and particulate composite mechanics. The investigation begins with an effort to replicate experimental PS coefficients of varying volume fraction alumina nanocomposites in Chapter 2. Once verified, the coating mechanics were integrated into the nanocomposite mechanics to define the multi-scale problem of nanocomposite PS coatings in Chapter 3. Additionally, the multi-scale mechanics are also shown to enable material property calculations with some simplifying assumptions. The mechanics and material property calculations developed in Chapter 3 are then applied to experimental PS data for uni-axial tensile samples in Chapter 4. Here it was shown that piezospectroscopy, with a secondary strain measurement, is a superior method to characterize material properties of composites which depend heavily on micro-mechanics.

A novel experiment that takes advantage of the spatial capabilities of piezospectroscopy and a spatial strain measurement with digital image correlation enabled the measurement of hyper-spectral PS response data in Chapter 5. Since it was demonstrated that a PS response can be equivalent to a mechanical response in Chapter 3, the principles of damage mechanics were applied independently to local PS responses. This enabled local determination of damage across the sample's surface. The imaged sample was an open hole tension composite coupon with a piezospectroscopic coating, and the results suggest that the coating was capable of sensing progression of subsurface damage. This is a convincing result that substantiates PS coatings are a powerful non-invasive damage sensor.

For this introductory chapter, a background is given which supports the motivation for the development of PS coatings for both engineering of advanced multifunctional composites and for in-service inspections. A comparison is made to some well established techniques currently used in the industry. This is followed by a description of the current state in the field of alumina epoxy composites and coatings which includes some multi-functional uses. Next, is a background of piezospectroscopy, which includes many previous laboratory applications. Finally, some damage mechanics is reviewed which can be applied to a PS response.

## **1.1 Developing Piezospectroscopy**

Piez spectroscopy is a technique to measure stress using the response of spectral emissions in a material, and this technique has been around for decades. This has been

most commonly applied to pressure sensors for diamond anvil cells [79], and indicators of residual stress build up in the oxide layer of thermal barrier coatings [87]. Despite this fact, the method has not been widely adapted for commercial applications in structural health monitoring since it has been limited to specific materials, such as chromium-doped Alumina, with intrinsic photo-luminescent emissions of high optical intensity and sensitivity to stress [41]. However, recent efforts that introduced photo-luminescent alumina nanoparticles as a constituent into a matrix material have extended the capability of the resulting nanocomposite [92]. This enables the tailoring of material properties and PS sensitivity for specific applications, such as compatibility with various structures and resistant to anticipated environmental conditions. Other material systems besides alumina-based nanocomposites have emerged such as carbon nanotube [100] or a fluorescent molecule [82] based nanocomposites.

The development of a piezospectroscopic (PS) coating for stress sensing of structures could have potential for a new, high-spatial resolution non-destructive evaluation (NDE) technique [30]. Most NDE techniques are dependent on the detection and determination of a flaw size [42]. This measured flaw size would then be referenced to a developed standard to discover if the flaw is within acceptable tolerances, or large enough to require a repair. The concept for the use of Piezospectroscopy in NDE would work in a similar way. Here, instead of determining a physical flaw size, the technique would measure the stress distributions around a flaw. This is demonstrated in Chapter 5 by recording stress gradients associated with damage progressing around an open hole composite coupon. Tolerances for piezospectroscopy applied as an NDE technique may consist of a combination of the spatial size and magnitude of the measured stress distribution. For example,

a more intense stress gradient with respect to a developed standard may indicate a more serious flaw and would require repair.

Potential uses of Piezospectroscopy are not only limited to NDE applications, but a method to assist in the engineering of advanced composites for optimized performance. It is a measure of micro-scale stress with multi-scale spatial resolution. This enables the ability to detect various failure modes that may originate at the micro-scale and propagate to the macro scale. This is demonstrated for alumina-epoxy nanocomposites in Chapter 3 and also for plasma sprayed alumina coatings in Chapter 4. In both materials, it was observed that the PS response was much more sensitive than conventional mechanical responses due to the micro-scale measurement that piezospectroscopy enables. A portion of this work is dedicated to developing and understanding the mechanisms behind both piezospectroscopy and advanced composites. To adapt piezospectroscopy into a wide range of NDE and composite design applications, the mechanics and relationships behind both piezospectroscopy and the mechanics of composites behavior must be well understood.

## **1.2 Alumina nanocomposites**

Nanocomposites in general have shown great promise for future applications in many industries. The intrinsic size effect of these micro and nano fillers give way to enhanced mechanical performance [105]. One of the many types of nano- or micro-inclusions that has been used in developing nanocomposites is the rigid ceramic, alumina. As a bulk material alumina has many interesting properties including excellent retention of strength



at high temperatures [75]. Alumina is often introduced as coatings for tribological properties because of its extremely high hardness and thermal/electrical insulation abilities. Recent papers have addressed alumina as a potential constituent in “chameleon” coatings for aerospace applications [97] which are designed to change their surface chemistry and structure in order to quickly adapt to the conditions of a space environment. These tribological coatings must be resilient for the 10-30 year lifetime in space and/or launch/re-entry cycling.

Here, alumina nanocomposites are studied for their stress sensing ability, which is uncommon among literature investigations that tend to focus on the various material properties. The development of alumina composites as PS coatings in commercial applications may still require significant commitment to research, but this work also serves as a voice to how piezospectroscopy could greatly aid in the development of alumina composites for various applications. While this work does not focus on the manufacturing or optimization perspective, its influence on mechanical performance is significant. A brief background of alumina composites and coatings will be supplied which serves as a guideline for future development of alumina composites and coatings.

With a focus on mechanical properties, alumina composites have been observed to greatly increase wear resistance when made in compression molds [10], and more modestly increase wear resistance when casted [48]. The wear resistance for alumina composites increased 600% when compared to unfilled samples [85]. Further increases in wear resistance by 3000% were observed when the nanoparticles had irregular shapes [10]. Effects of surface treatment and smaller particles were also observed to increase wear resistance [48, 88].

Introduction of alumina nanoparticles have varying effects on fracture toughness [69]. In general, the addition of particles increases the fracture toughness but there are many factors to consider when evaluating the performance. These factors include particle size [69, 107, 14, 20], particle shape [59], surface treatment [59, 107, 20], and dispersion [107]. These factors are not only limited to alumina composites but also apply to particulate composites in general.

Because these properties are so heavily dependent on micro-structural characteristics, the application of piezospectroscopy could supply a greatly enhanced understanding of the micro-mechanics. A stress measurement of the embedded particle can indicate when the matrix begins to yield, when matrix-particle interface begins to breakdown, and even how particle size and shape alter the stress transfer at these micro- and nano-scales. Chapter 2 and 3 both introduce concepts in applying a combination of piezospectroscopy and multi-scale mechanics to better characterize nanocomposites.

### **1.2.1 Alumina Coatings**

Alumina coatings are usually for applications where excellent wear/corrosion resistance or thermal/electrical insulations are needed, such as the “chameleon” coatings discussed earlier [97]. There are several ways to develop high content alumina coatings including: Microarc oxidation (MAO) [93], Chemical Vapor Deposition (CVD) [50], radio frequency magnetron sputtering [52, 17], plasma spray [38], sol-gel dip coating [43, 80], and epoxy thin films impregnated with nano-sized alumina [25]. If the application of a stress sensing coating which utilizes piezospectroscopy is considered, the  $\alpha$  phase alumina needs to

have a significant presence since it exhibits the characteristic R-lines which are discussed in the next section. The methods mentioned here have varying degrees of success for obtaining high  $\alpha$ -alumina content because the high temperatures required for some of these processes can lead to phase changes in the alumina.

In this work, both a plasma-spray alumina coating and an epoxy nanocomposite coating were investigated in Chapters 4 and 5 respectively. The plasma spray, which initially had a feedstock of 95%  $\alpha$  phase reduced to 25%  $\alpha$  phase after the deposition of the coating. One way to guarantee a high content  $\alpha$ -alumina coating is to start with it as a precursor and have a low temperature process to fabricate the coating, such as that done in Chapter 5 with a alumina-epoxy coating with 20% volume fraction alumina. This is also practical for application to a wide range of structures because exposing them to high temperatures may induce thermal damage. However, a high temperature process may be appropriate for some structures with a high thermal stability.

### 1.3 Piezospectroscopy

Alumina has been one of the most widely used PS materials. The  $\alpha$  phase of alumina contains  $Cr^{3+}$  ions at very low concentrations which give a sharp photo-stimulated luminescence (PL) doublet peaks at 14402 and 14432  $cm^{-1}$  known as the R-lines. The stress dependence of the emitted R-lines was first used in a form of ruby as a pressure gage in diamond anvil cells [79, 23, 74]. This enabled a secondary stress measurement which was non-invasive for experiments which were conducted at ultrahigh pressures [47]. Because

the non-invasive stress measurement was so successful, it was quickly adapted to other laboratory applications [73, 98, 78, 18].

One industrial application that has adapted PS for stress and damage assessment is for thermal barrier coatings (TBC) systems on turbine blades [46, 68]. In these systems, the stress-sensing capability originates from the photo-luminescent peaks of the naturally occurring oxide layer that develops with thermal cycling. This is used to measure the residual stresses of this layer and is correlated with the life of the coating as it is exposed to thermo-mechanical cycles [60].

Another application that closely aligns with the present work was using piezospectroscopy to study the load transfer mechanics in fiber composites. When sapphire [64, 67] or polycrystalline alumina [40] fibers were embedded in composites, this enabled non-invasive stress measurements of the fibers. Experiments involving pushout tests of fibers with different coatings were successful in monitoring improved interface strength between the matrix and fiber [66]. Also, small mechanical tests under a microscope [40] investigated the evolving stress distributions around a broken fiber. Both of these studies showed how piezospectroscopy can substantiate analytical and finite element models (FEM) in studies of the mechanics of reinforcements while also adapting to other applications.

The general tensorial relationship for PS shifts for a PS material is below in Equation 1.1 [35].

$$\Delta\nu = \Pi_{ij}\sigma_{ij} \tag{1.1}$$

Equation 1.1 can be applied to both the R1 and R2 lines, as they have separate sensitivities when they are loaded on the same crystallographic axis [90]. Thus, when crystallographic orientations are known from specific sample manufacturing or from the use of a polarizer [39], a complete state of hydrostatic and non-hydrostatic stress may be determined [90].

In the case of a polycrystalline PS material, an averaging effect takes place over all of the grains within the probed volume. Usually the grain size is much smaller than the probed volume determined by laser dot size, and this creates a scalar relationship with hydrostatic stress in Equation 1.2 [60, 40].

$$\Delta\nu = \frac{1}{3}\Pi_{ii}\sigma_{jj} \quad (1.2)$$

In Equation 1.2 the trace of the PS tensor ( $\Pi_{ii}$ ) for R1 and R2 are within experimental uncertainty of each other and are equal to  $7.6 \frac{cm^{-1}}{GPa}$  [35, 65, 40]. Equation 1.2 served as a starting point for much of the work provided in Chapters 2 and 3. In polycrystalline materials it is possible to obtain the non-hydrostatic component of stress from spectral characteristics such as peak broadening and others [65, 90].

This work focuses on developing the mechanics necessary to understand the PS shifts of nanocomposites with embedded PS inclusions. Recent work by Stevenson [92] and Ergin [24] both identified that with increasing volume fraction of PS particulate filler, the sensitivity of the PS effect becomes higher. The increase of the PS effect for nanocomposites will be predicted using composite inclusion mechanics and compared with the experimental works of Stevenson and Ergin.

## 1.4 Damage Mechanics with Piezospectroscopy

Piezospectroscopy offers a non-invasive micro-scale stress measurement, and with a secondary mechanical measurement, they are combined to produce a PS response. PS responses are synonymous to mechanical responses, with only one axis of the loading surface being replaced by the PS measurement. In Chapter 3, it will be demonstrated that the mechanics which apply to a mechanical loading surface need only be slightly modified to account for the PS component. With this in mind, damage mechanics normally applied to mechanical loading surfaces can now be applied to local PS responses for local material property characterization.

Damage is usually defined as the reduction in stiffness of a material through mechanical loading [2], or also by a reduction in the effective stress carrying area [63]. The latter results in an increase in stress on the remaining part of the material and is associated with a reduction in stiffness [12]. This reduction in stiffness is referred to as elastic degradation. Using the mechanical response, the elastic degradation can be quantified by using an unloading curve and calculating the resulting slope [2, 77]. In Chapter 4 unloading curves of the PS response were used to quantify the degradation of the elastic modulus of the plasma-sprayed alumina coating.

If unloading curves were not integrated in the experimental procedure, then the unloading curves may be simulated to estimate the reduced mechanical properties. Methods of simulating these unloading curves vary in complexity, ranging from simple elastic degradation models to the involved continuum damage mechanics with coupled plasticity [12, 89, 36, 104]. A simple and convenient method to simulate an unloading curve is to

assume no plastic deformation so all unloading curves return to the origin [12]. This was the method chosen for simulating the unloading curves in a alumina-nanocomposite under compression in Chapter 3. In reality, unloading is usually associated with some combination of elastic degradation and plastic deformation. In Chapter 5 this same method to simulate the unloading curves was also used, but also a secondary method was also used which combined some finite plastic deformation for comparison. The addition of some plastic deformation into the simulated response is a more accurate representation of material behavior [12].

Because piezospectroscopy is a micro-mechanical measurement, and damage mechanics is based off the propagation, nucleation and growing of micro-defects [104], it provides a more sensitive measure of damage. As observed in Chapters 3 and 4, the elastic degradation as calculated with piezospectroscopy was much greater than that as observed from the nominal mechanical measurements. Despite the initial elastic modulus calculations for both techniques being similar, the differences in the rate of degradation is evident of micro-mechanical damage directly probed *via* piezospectroscopy. This supports why piezospectroscopy not only has great potential for NDE techniques, but also great promise in engineering advanced nanocomposites.

## CHAPTER 2 MECHANICS OF PIEZOSPECTROSCOPIC NANOCOMPOSITES

This chapter will focus on describing the PS response of nanocomposites with embedded PS inclusions. Particle mechanics, which describe the stress of an embedded inclusion, must be well understood to interpret the PS response. Starting with Eshelby's original formulations for dilute system of inclusions, a procedure will be shown which slightly modifies Eshelby's equations which was motivated by the work of Kim [53], but applied in a more general sense for any equivalent composite property model. This enables more accurate predictions of PS properties of nanocomposite, and expressions derived here will be used in later chapters for material state measurements. Additionally, an effort to use Finite Element models (FEM) to predict the PS properties is presented.

### 2.1 Experimental Background

Recent work has shown an enhancement of the PS coefficients when the spectrally active material is introduced as nanoparticles into an epoxy system [92]. The PS coefficients have been observed to increase with volume fraction of alumina nanoparticles. As a result, the volume fraction could be optimized for a more sensitive stress measurement with piezospectroscopy. The basis of this change in sensitivity is due to the differing rates of load transfer into the inclusions that occurs with varying of their volume fraction.

In this work, analytical and numerical nanocomposite mechanics are compared to the experimental PS coefficients experimentally determined in the works of Stevenson and Ergin [92, 24]. These works both showed increases PS sensitivity with higher volume



fractions. In terms of the theoretical calculations, this would correspond to an embedded nanoparticle sustaining a higher mean stress per applied uniaxial compression to the composite with higher volume fractions. These results motivated and supplied substantiating values for the the theoretical modeling of nanocomposite mechanics in this chapter.

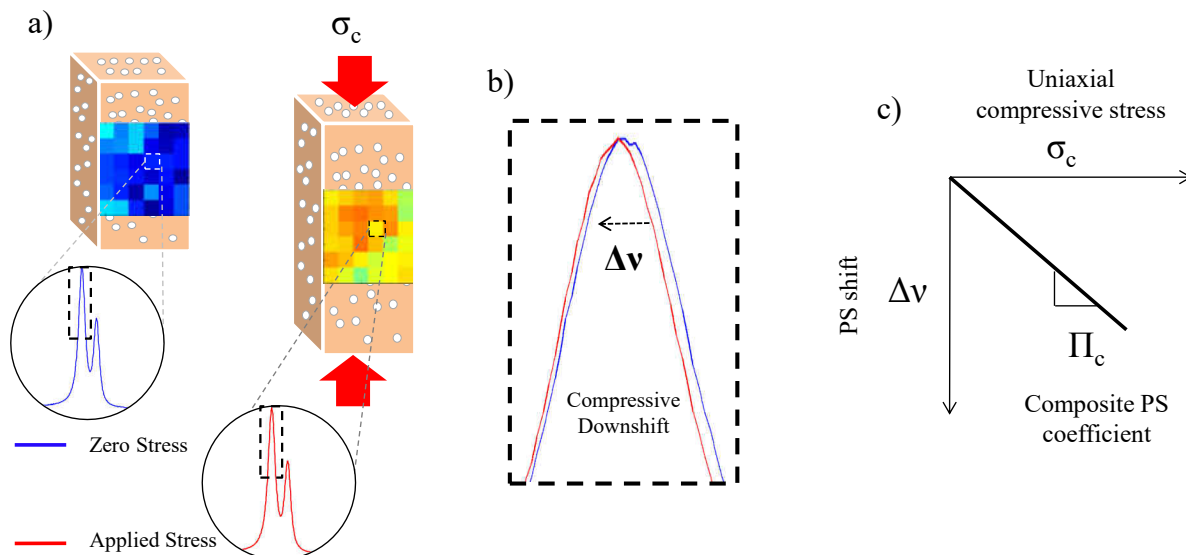


Figure 2.1: (a) A schematic representing hyperspectral imaging of a PS nanocomposite under compressive loading, (b) corresponding peak position downshifts with compressive loading, and (c) the composite PS coefficient ( $\Pi_c$ ) relating a peak position shift with applied stress.

Composite PS coefficients ( $\Pi_c$ ) values were recorded for different volume fractions of alumina nanoparticles embedded in an epoxy matrix as shown in Table 2.1 [92, 24]. The experiments were conducted with epoxy nanocomposites with embedded alumina nanoparticles (150 nm). The samples were manufactured as parallelepipeds, using ASTM standard D695 [3] with dimensions of 1/8 x 1/8 x 1/2 inch.

Table 2.1: Experimental PS coefficients ( $\Pi_c$ ) for R1 and R2 peaks [92, 24]

Volume Fraction %	R1 PS Coefficient $\frac{cm^{-1}}{GPa}$	R2 PS Coefficient $\frac{cm^{-1}}{GPa}$
5	-3.16	-2.60
20	-3.34	-3.19
25	-3.65	-3.42
34	-4.10	-3.88
38	-5.63	-5.08

## 2.2 Piezospectroscopic Nanocomposite Mechanics

The spectral shifts of the photo-luminescent (PL) R-lines for polycrystalline alumina  $\Delta\nu_{poly}$  have been correlated in literature to the hydrostatic stress  $\frac{1}{3}\sigma_{ii}$  by the PS coefficient  $\Pi_{ii}$  in Equation 2.1 [41]. For the stress sensitive peaks,  $\Pi_{ii}$  has a value of -7.59 and -7.62  $\frac{cm^{-1}}{GPa}$  for R1 and R2 in polycrystalline alumina respectively [41]. The relationship can be reduced down to the first invariant ( $\sigma_{ii}$ ) for a more general case.

$$\Delta\nu_{poly} = \frac{1}{3}\Pi_{ii}\sigma_{ii} \quad (2.1)$$

Alternatively, A nanocomposite which sustains uni-axial applied stress ( $\sigma_a$ ) will have a PS coefficient ( $\Pi_c$ ), which is the linear relationship between the uni-axial stress and the observed shift of the R-lines  $\Delta\nu_c$  as shown in Equation 2.2.

$$\Delta\nu_c = \Pi_c\sigma_a \quad (2.2)$$

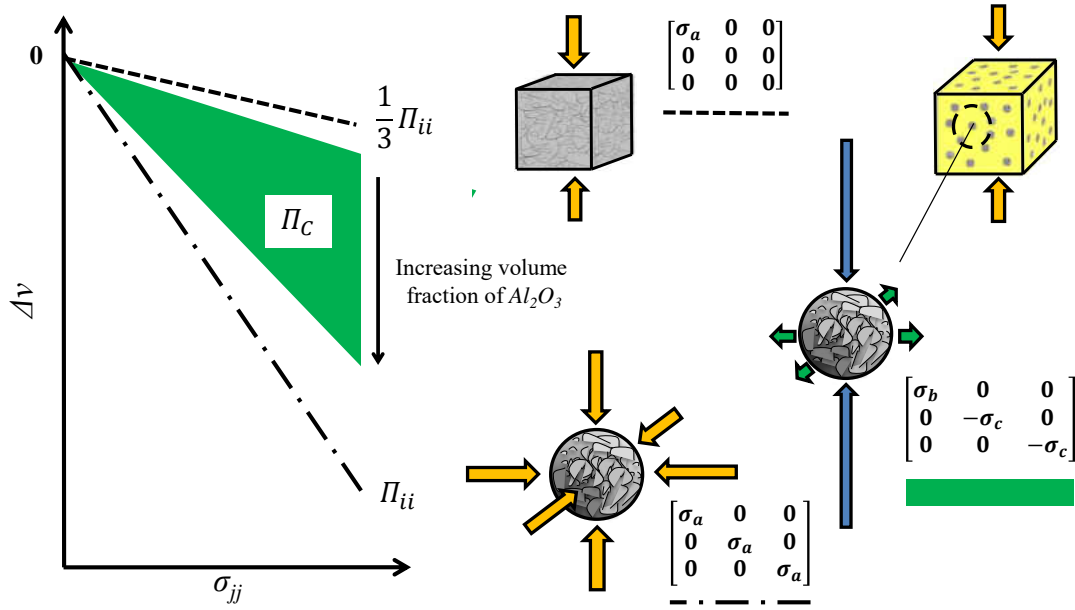


Figure 2.2: The Piezospectroscopic relationships for different loading conditions of a PS constituent.

Because this PS coefficient for the composite is higher than a polycrystalline material under the same uniaxial stress, the embedded particle's 1st invariant must be higher than the 1st invariant of the bulk polycrystalline alumina. If that same uniaxial stress was applied as pressure to the particle on all principal axes, then the observed PS coefficient would be greater than all of the observed uniaxial PS coefficients for the nanocomposites. It is noteworthy that all the ( $\Pi_c$ ) values fall between  $\Pi_{ii}$  and  $\frac{\Pi_{ii}}{3}$ . It is hypothesized that these values may act as upper and lower limits for  $\Pi_c$  because they represent idealized configurations. A schematic that demonstrates the experimental and theoretical nomenclature of the current discussion was included in Figure 2.2.

The PS coefficients increasing for higher volume fractions suggest that the applied stress converts into hydrostatic stress to the particles at a higher rate for the higher

volume fractions. To understand this phenomena, Equations 2.1 and 2.2 are equated into equation 2.3. This expression reveals that the experimental PS coefficient is directly proportional to the 1st invariant of the particle.

$$\frac{\frac{1}{3}\sigma_{ii}}{\sigma_a} = \frac{\Pi_c}{\Pi_{ii}} \quad (2.3)$$

Equation 2.3 is an important expression that reveals a direct measure of the first invariant of the particle with the experimental PS data, and can be used to correlate theoretical models to experimentally measured particle stresses. This ratio of hydrostatic stress induced on the particle per uniaxial stress on the composite will henceforth be termed the hydrostatic stress ratio. This value, on the left hand side of Equation 2.3, is able to be quantified by both analytical and numerical methods for comparison to experimentally observed nanocomposite PS coefficients.

### 2.3 Analytical formulation

The classical Eshelby model for dilute systems [26] was used to estimate the fraction of stress the nanoparticle sustains with respect to the overall composite under applied stress. The Eshelby model used here has several assumptions, and they are as follows: (1) a single particle is embedded in an infinite matrix (infinitesimal volume fraction), (2) a perfectly spherical nanoparticle, (3) perfect bonding occurs between the nanoparticle and the matrix, and (4) both the nanoparticle and the matrix phase are isotropic. This basic

model, despite its many assumptions, was shown in previous work to be closely correlated to the experimental data obtained for the lowest volume fraction of 5% [32, 28].

The formulation [15] is based on a spherical particle (p), embedded within an isotropic matrix (m). The stress inside the particle ( $\sigma^p$ ) can be calculated from multiple strain terms shown in equations 2.4, 2.5 and 2.6 where  $e$ ,  $e^o$ , and  $e^*$  represent the strain disturbed by the filler, the mechanical strain of the matrix from applied load, and the equivalent eigenstrain of the inclusion problem, respectively. Additionally,  $C$  and  $S$  represent the stiffness and Eshelby tensors, respectively [15].

$$e = Se^* \quad (2.4)$$

$$e^o = (C^m)^{-1}\sigma^m \quad (2.5)$$

$$e^* = -[(C^p - C^m)S + C^m]^{-1}(C^p - C^m)(C^m)^{-1}\sigma^m \quad (2.6)$$

Finally, by using the above strain terms, the stress inside the filler can be computed using from the applied stress to the matrix using Equation 2.7 [15]. Then, employing Equation 2.8, this yields the first invariant of the particulate ( $\sigma_{ii}^p$ ).

$$\sigma^p = C^m(e^o + e - e^*) \quad (2.7)$$

$$\sigma_{ii}^p = \frac{\text{trace}(\sigma^p)}{3} \quad (2.8)$$

The formulation using the Eshelby model above can give the hydrostatic stress ratio as defined in the previous section. This stress ratio is representative of an infinitesimal

volume fraction because of the 1st assumption of Eshelby's theoretical formulation. These results can be combined with Equation 2.3 to relate the Eshelby stress calculation to what is experimentally observed with PS.

Using the Eshelby dilute equations, the hydrostatic stress ratio can be applied in a more general sense to be a function of material properties of the matrix and inclusion. These expressions will be derived now for both the 1st stress and strain invariant, but used later in Chapters 3. The first step is to combine the three different components of strain into Equation 2.7 [15] which now relates the strain tensors between the particle and matrix in Equation 2.9 and 2.10. The result in Equation 2.10 can be obtained by applying Hooke's law to Equation 2.7 and some minor rearrangement. Similarly, the same procedure could be used to relate the stress tensors of the particle and composite.

$$F\epsilon^m = \epsilon^p \quad (2.9)$$

$$F = (C^p)^{-1}C^m[I - (S - I)][(C^p - C^m)S + C^m]^{-1}(C^p - C^m) \quad (2.10)$$

This simplified relationship can be viewed in Voigt notation in Equation 2.3. These scalar components that make up the 4th order tensor  $F$ , can be shown to relate the first strain invariants between the particle and composite phases in Equation 2.12, which are also conveniently made up of material properties of the two phases and shown in Equation 2.13. A similar expression can be shown to relate the first stress invariants of the two particles in Equation 2.14.

$$F = \begin{vmatrix} F_1 & F_2 & F_2 & 0 & 0 & 0 \\ F_2 & F_1 & F_2 & 0 & 0 & 0 \\ F_2 & F_2 & F_1 & 0 & 0 & 0 \\ 0 & 0 & 0 & F_3 & 0 & 0 \\ 0 & 0 & 0 & 0 & F_3 & 0 \\ 0 & 0 & 0 & 0 & 0 & F_3 \end{vmatrix} \quad (2.11)$$

$$(F_1 + 2F_2)\epsilon_{ii}^m = \epsilon_{ii}^p \quad (2.12)$$

$$\frac{\epsilon_{ii}^p}{\epsilon_{ii}^m} = (F_1 + 2F_2) = \frac{-3E^m(2\nu^p - 1)(\nu^m - 1)}{(2\nu^m - 1)(2E^m + E^p - 4E^m\nu^p + E^p\nu^m)} \quad (2.13)$$

$$\frac{\sigma_{ii}^p}{\sigma_{ii}^m} = \frac{-3E^p(\nu^m - 1)}{2E^m + E^p - 4E^m\nu^p + E^p\nu^m} \quad (2.14)$$

The strain based expression in Equation 2.13 will be useful in later chapters which describe the PS response with strain based mechanical measurements. The stress based expression in Equation 2.14 can be used in the current section to replicate the experimental PS coefficients from the works of Ergin [24] and Stevenson [92]. It is noteworthy that both expressions are functions of material properties of the host matrix and embedded particle. With an inverse solution, this enables the calculation of material properties from an observed PS response. These expressions will be very important later for material property and damage analysis with Piezospectroscopy in Chapter 3.

Using the material properties of the inclusion phase of  $\alpha\text{-Al}_2\text{O}_3$  ( $E^p = 300$  GPa,  $\nu^p = 0.2$ ) and an isotropic matrix phase of EPON 862 ( $E^m = 2.41$  GPa,  $\nu^m = 0.4$ ), the stress ratio can be calculated and compared to the experimental data. Using Equation 2.3 and observing Figure 2.3, the comparison shows that the Eshelby model accurately predicts the smaller volume fraction's stress ratio.

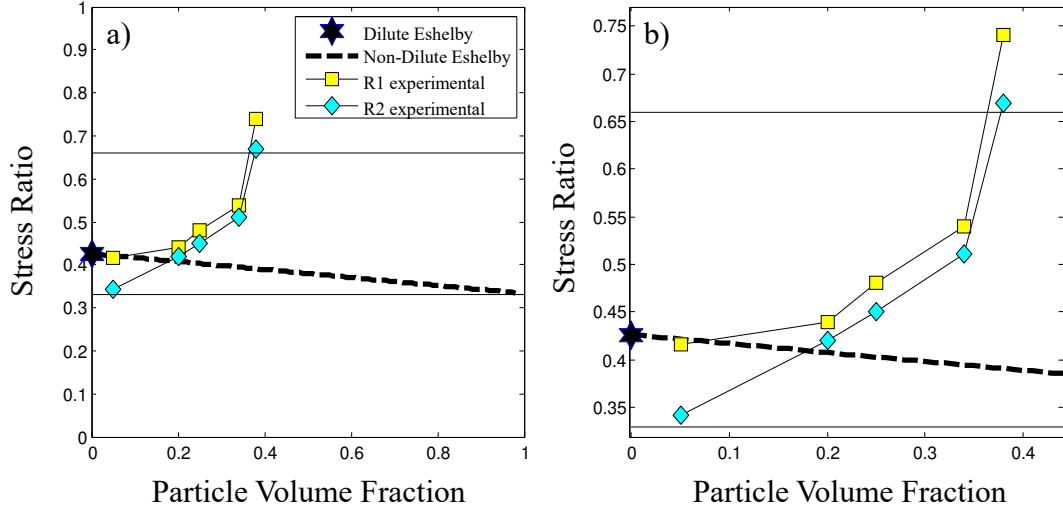


Figure 2.3: The theoretical Eshelby [15, 26] model predicting the PS properties for a composite and compared to experimental data from the works of Ergin [24] and Stevenson [92].

However, this dilute Eshelby model only takes into account an infinitesimal volume fraction because of the first assumption stated earlier. Eshelby modified his own dilute assumption for a non-dilute case. This non-dilute Eshelby model was also investigated where the eigenstrain in the particle is now a function of volume fraction  $f$  in equation 2.15 [15].



$$e^* = -[(C^m - C^p)(S - f(S - I) - C^m)^{-1}](C^m - C^p)(C^m)^{-1}\sigma^m \quad (2.15)$$

From inspection of Figure 2.3, The non-dilute Eshelby diverges away from experimental data for higher volume fractions. It is observed that the predicted stress ratio of the non-dilute Eshelby model approaches  $\frac{1}{3}$ . This is because a bulk polycrystalline alumina under uniaxial stress would show a third of as much PS sensitivity compared to then the pressure is applied in a hydrostatic fashion. This concept was previously illustrated in Figure 2.2. Figure 2.3 shows that the experimental stress ratios continue to increase with increasing volume fraction. This creates a motivation for adapting modified Eshelby solutions to more accurately predict the PS properties of composites for higher volume fractions.

## 2.4 Equivalent Composite Property Models Integrated with Dilute-Eshelby

There are many different models in literature for estimating equivalent composite properties for varying volume fractions [21, 101, 9, 106, 57, 84]. The goal of this section is to illustrate the method of using equivalent composite property models combined with the dilute Eshelby equations to better predict the PS properties for varying volume fraction. This was motivated by the work of Kim [53], who developed his own iterative technique to predict composite properties in a relatively simple way.

First, this section will review the concept illustrated by Kim [53]. Then, a new type of method will be proposed that combines equivalent composite property model with the

Dilute Eshelby equations. Several equivalent composite property models exist, but here only the equivalent composite property model of Mori-Tanaka [72, 34] was selected to demonstrate the technique.

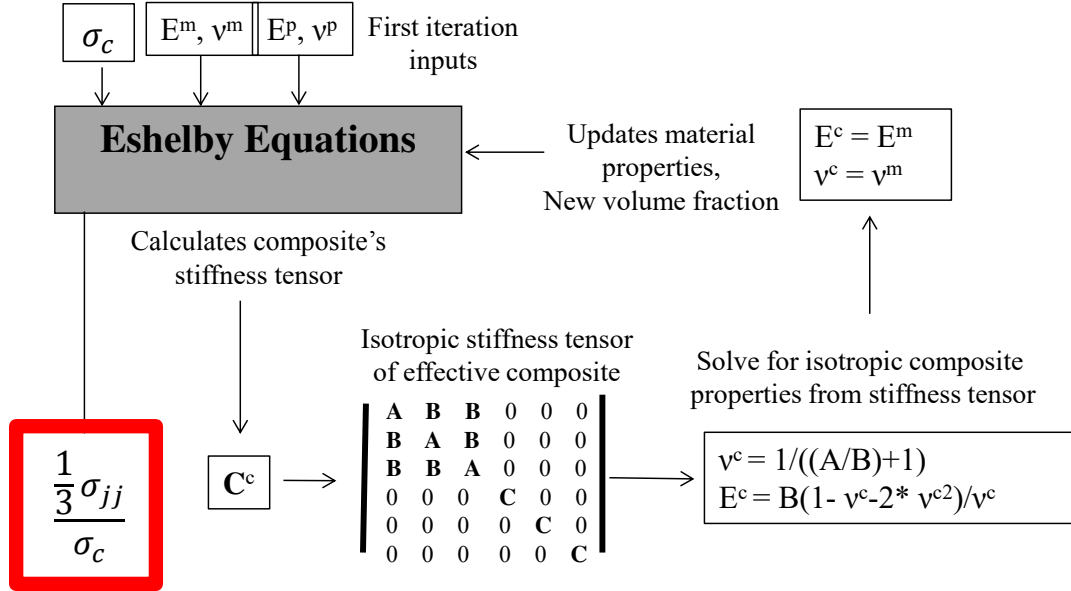


Figure 2.4: This is the iterative loop developed originally by Kim et. al [53] to predict the elastic properties of composites. Here, the iterative loop is used to calculate the PS properties for varying volume fractions.

Kim et al. [53] created an iterative programming loop that adds infinitesimal volume fractions and iterates new equivalent matrix properties for increasing volume fractions. This technique is referred to as successive embedding. The framework of this technique is described in Ref. [53], and illustrated in Figure 2.4. It is based on an assumption that the Eshelby Equations can be used with the matrix properties replaced by equivalent composite properties. Using successive embedding described in Ref. [53], equivalent

composite properties are calculated for an incremental volume fraction, and then used as the matrix properties in the Dilute Eshelby equations.

The series of Eshelby equations used to derive the hydrostatic stress ratio, shown in Section 2.3, are iterated with equivalent composite properties of Elastic Modulus,  $E^c$  and Poissons ratio,  $\nu^c$ . During this process, the equivalent composite properties converge towards the particles properties at a volume fraction of 100% alumina.

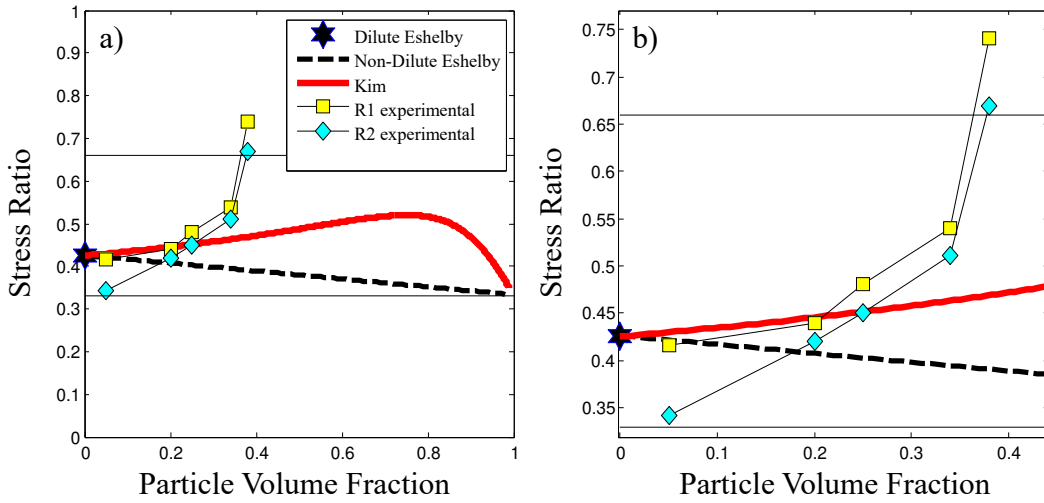


Figure 2.5: The PS properties as predicted by the non-dilute Eshelby [26, 15] compared to the results from Kim et. al [53] and experimental data from the works of Ergin [24] and Stevenson [92].

Kim’s method [53], applied to determine the hydrostatic stress in the particles, was plotted with the experimental data in Figure 2.14. The method was successful in predicting PS properties for low and intermediate volume fractions  $\leq 20\%$  with good accuracy. Most of the composite coatings that have been studied are manufactured with  $\leq 20\%$  volume fraction [30, 27]. At volume fraction of 38% alumina, the experimental results

show a dramatic increase in the hydrostatic stress ratio. This large increase for higher volume fractions is investigated in the section 2.5 using Finite Element models.

To continue development of these load transfer models, an alternative and more general method of modifying the Eshelby theory is proposed. The newly proposed method of modifying Eshelby would be compatible with different prediction schemes as shown in Fig. 2.8. A different equivalent composite property model could be treated as the new inputs for the Dilute Eshelby equations.

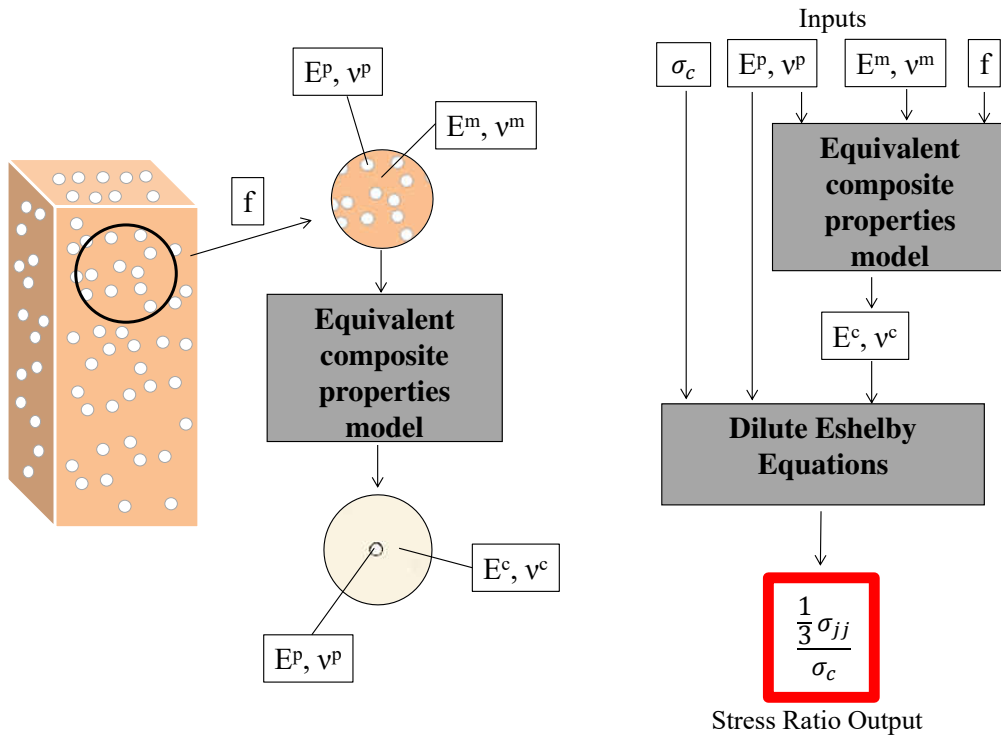


Figure 2.6: A modified Eshelby Scheme which has the potential to combine any material properties prediction model for composites.

The equivalent composite properties model chosen to demonstrate the method illustrated in Figure 2.8 was the Mori-Tanaka method [72, 34]. This model was chosen

because it assumes that the composite is isotropic and contains randomly distributed spherical inclusions. The equations which govern this model are given below.  $K$  and  $G$  represent the bulk and shear moduli respectively of the matrix ( $m$ ) and the particle ( $p$ ), with a particle volume fraction  $f$ .

$$G^c = G^m + \frac{fG^m(G^p - G^m)}{G^m + \beta_1(1 - f)(G^p - G^m)} \quad (2.16)$$

$$K^c = K^m + \frac{fK^m(K^p - K^m)}{K^m + \beta_2(1 - f)(K^p - K^m)} \quad (2.17)$$

where,

$$\beta_1 = \frac{2(4 - 5\nu_m)}{15(1 - \nu_m)} \quad \text{and} \quad \beta_2 = 3 - 5\beta_1 \quad (2.18)$$

It is desired that the Elastic modulus and Poisson's ratio are the two independent properties which describe the isotropic properties of the composite because these are normally what is measured in material testing. This is done so by Equation 2.19.

$$E^c = \frac{9K^cG^c}{3K^c + G^c} \quad \nu^c = \frac{E^c}{2G^c - 1} \quad (2.19)$$

The experimental data collected by Ergin used strain gages to measure the elastic modulus of the alumina nanocomposites [24]. This allows for an opportunity to compare the equivalent composite property models of Kim and Mori-Tanaka to some experimental values in Figure 2.7

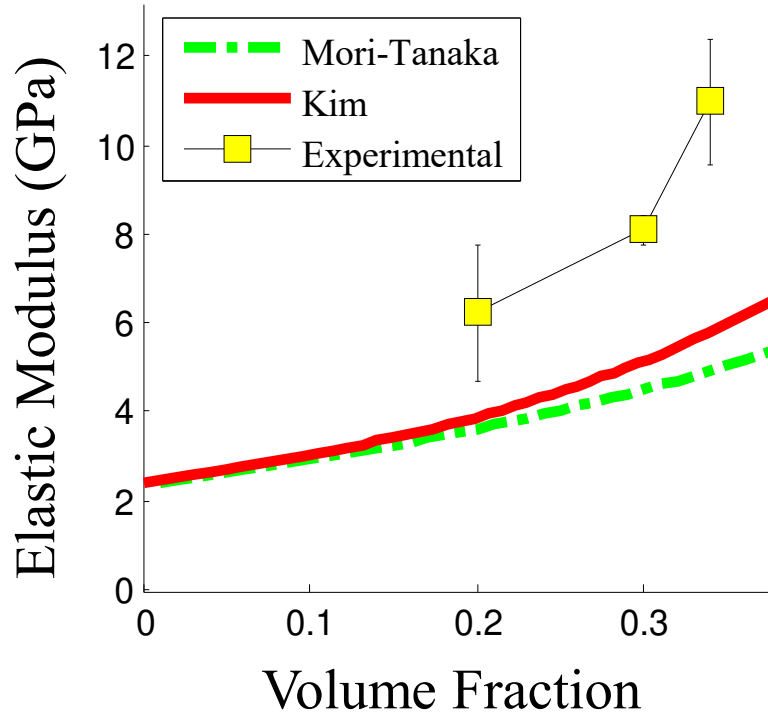


Figure 2.7: Experimental data from alumina epoxy nanocomposites from the works of Ergin [24] compared to the estimated composite properties of Mori-Tanaka and Kim.

The predicted elastic modulus values under-predict the experimental modulus values with similar magnitudes. Now, the Mori-Tanaka equivalent composite property model will be blended with the Dilute Eshelby model using the process illustrated in Figure 2.8 and compared to Kim’s method.

From these results, it is observed that using different equivalent composite property data gives varying degrees of success. There are different material property prediction schemes which have been developed in literature [106, 57] but to review and implement them all is outside the scope of the current work. From the current results, all analytical models still under-predict the stress in the particles compared to what was experimen-

tally observed for high volume fractions. The effect of micro-structural features present at higher volume fractions could potentially contribute to this difference. Alternative methods to analytically predicting the stress in the nanoparticles are possible through Finite Element Models (FEM) [86, 13, 6]. By use of an FEM of the nanoparticle system, insights may be gained as to what specific micro-structural feature leads to this dramatic increase in the stress ratio for higher volume fractions.

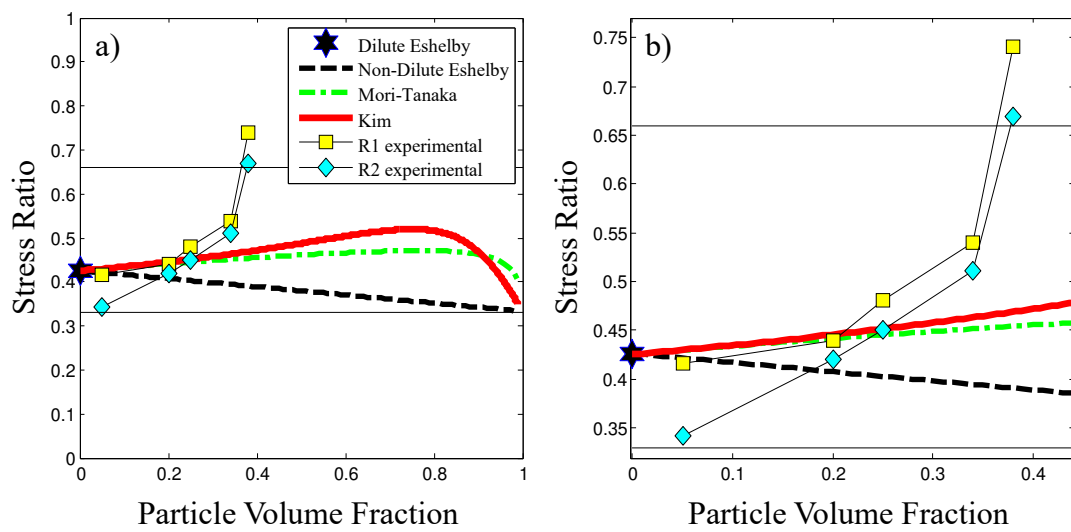


Figure 2.8: The equivalent composite properties model utilizing the Dilute Eshelby [15] compared to Kim’s method [53], Non-Dilute Eshelby, and experimental data from Ergin [24] and Stevenson [92].

## 2.5 Finite Element Analysis

In addition to the theoretical calculation, finite element simulations were performed to investigate effects of increasing volume fraction in addition to multiple micro-structural characteristics on the stress sensing properties of these nanocomposites.

As a preliminary proof of concept, a simplified two dimensional representative volume element (RVE) was created to simulate an embedded nanoparticle. Varying volume fraction of  $\alpha\text{-Al}_2\text{O}_3$  in an idealized RVE was the initial focus of the investigation to changes in the mean stress sustained.

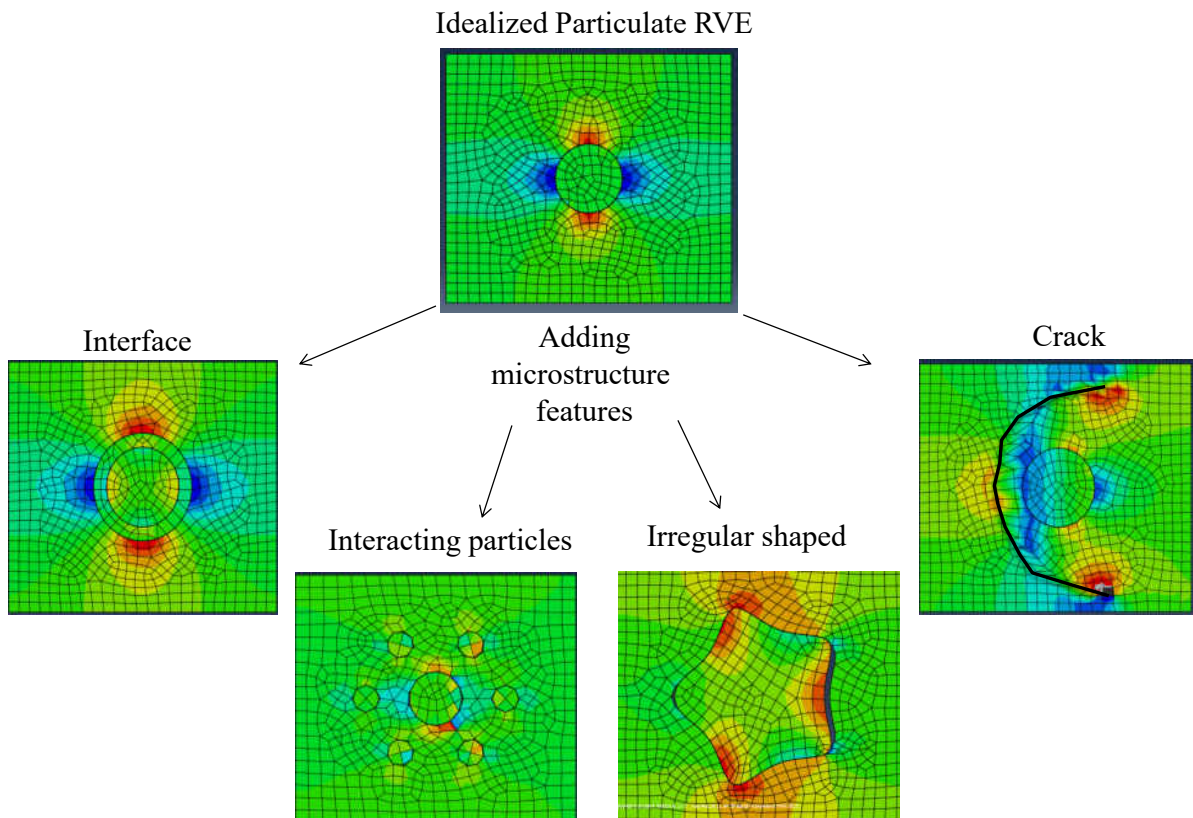


Figure 2.9: Modifying an idealized RVE by introducing a variety of different micro-structural features.



With a baseline for the volume fraction effect for an idealized RVE established, micro-structural features to simulate non-ideal conditions that stray away from Eshelby's main assumptions stated in Section 2.3 were investigated. Different micro-structural features were embedded into the nanoparticle system such as (1) irregular shaped particles (2) interacting particles (3) interface effects, and (4) microcracks to observe their effects on the particles mean stress. There are many micro-structural characteristics of the embedded inclusions. This work addresses these different types of micro-structural variables and their effect on load transfer.

### 2.5.1 Problem Statement

The approach for the finite element model is illustrated in Figure 2.10 ABAQUS<sup>®</sup> was used to carry out the FEM simulations. There was a limitation on the number of elements of the model to be under 1000 resulting in a relatively rough mesh. The parts were meshed in this work with standard, linear, plain strain elements in a quadrilateral shape. An RVE was created to simulate a nanocomposite composed of an isotropic inclusion phase of  $\alpha\text{-Al}_2\text{O}_3$  ( $E = 300$  GPa,  $\nu = 0.2$ ) and an isotropic matrix phase of EPON 862<sup>®</sup> ( $E = 2.41$  GPa,  $\nu = 0.4$ ).

Boundary conditions fixed the vertical displacement ( $u_2$ ) on the bottom surface. Then an applied pressure of only 1 kPa was applied to the top surface. The small applied pressure is to keep the model in its entirety in the elastic regime. The remaining surfaces were unconstrained.

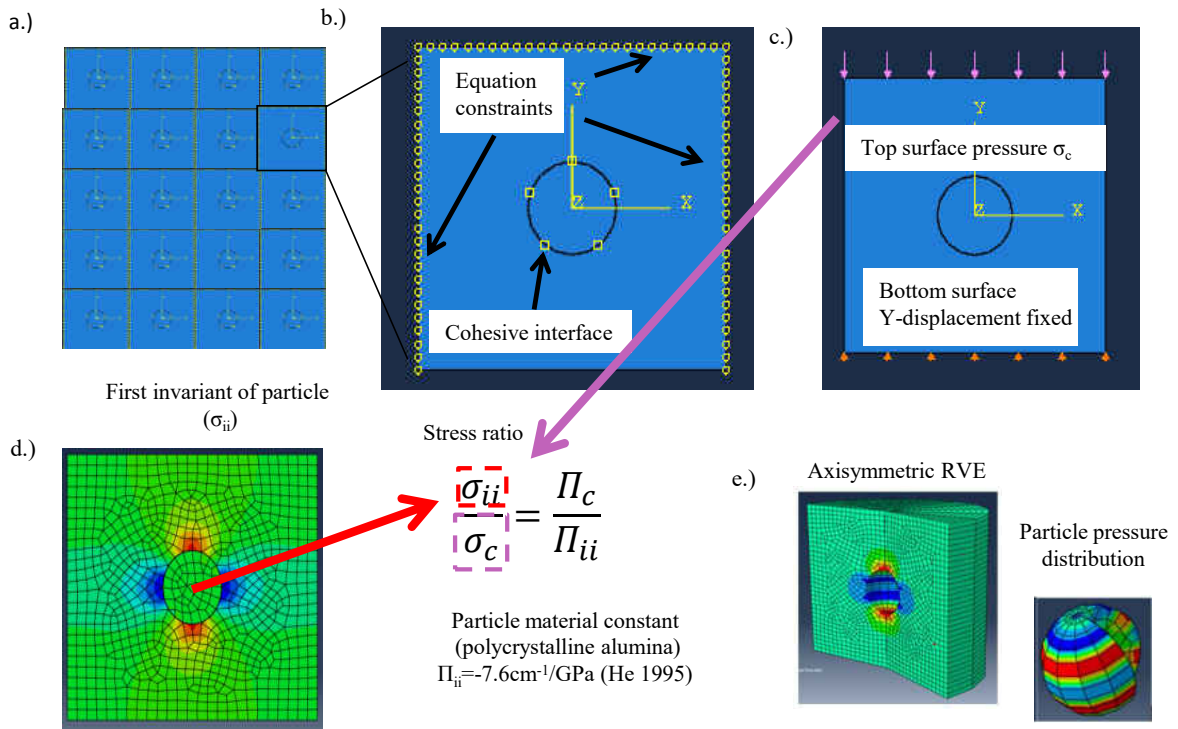


Figure 2.10: (a) The RVE for an alumina nanocomposite. (b) Details are presented for constructing the interface and constraints and (c) the loads and boundary conditions, as well as (d) meshed assembly of the matrix and particle with the method of predicting the composite's PS properties. (e) The stress ratio obtained from a 5% alumina volume fraction composite in an axisymmetric model simulated Eshelby stress ratio exactly.

The quadrilateral shape of the elements was required for introducing cracks into the epoxy so it was used for all simulation to maintain consistency. For the crack simulation, no propagation is considered because the applied stress is not reaching any critical level to initiate crack growth.

Figure 2.10b shows the equation of constraints that were created for the left, right, and top sides by picking a reference node ( $u_{ref}$ ) on each side and equating the remaining  $i$  nodes on each surface ( $u_i$ ) to have equal displacement. The equation took form  $0 =$

$u_{ref} - u_i$  forcing all of nodes assigned to a side to have equal displacement. This kept the left and right sides straight and parallel, in addition to the top surface straight and perpendicular to the sides. With the sides constrained, this satisfied the requirements for the RVE to be representative of a larger scale composite.

The matrix-particle interface was defined with default cohesive interface properties with the matrix and the particle phase as the master and slave surfaces respectively. This interface condition had the smallest difference with the experimental data for the plane strain models. Different interface values are presented in Table 2.5.1. It should be noted that an axisymmetric model with the proper boundary conditions gives an identical stress ratio as the dilute Eshelby model (0.426). While this may seem attractive to use as a starting point for testing volume fraction effects, cracks and interacting particles cannot be implemented into an axisymmetric model. Thus, a square RVE was created which utilizes a plane strain assumption and allows the freedom to introduce various micro-structural features into the RVE later.

Table 2.2: Model type and matrix-particle interface boundary conditions

<b>Model</b>	<b>Interface</b>	<b>Sliding</b>	<b>Stress Ratio</b>
Axisymmetric	rough	small	0.507
Axisymmetric	rough	finite	0.495
Axisymmetric	cohesive	small	0.426
2-D	rough	small	0.487
2-D	rough	finite	0.482
2-D	cohesive	small	0.471

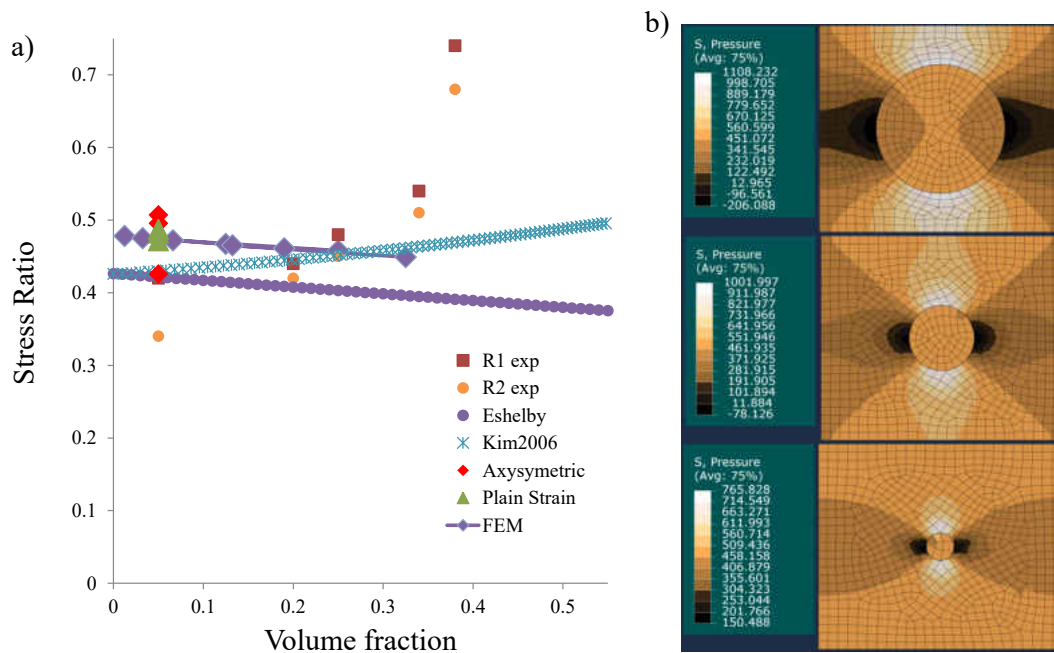


Figure 2.11: (a) Stress Ratio results for varying volume fractions and different interface boundary conditions. (b) A Variety of models predicting volume fraction effects.

The volume fractions were simulated by equating the appropriate area ratios between the matrix and inclusion shown in Figure 2.11. The average pressure for all the elements within the particle phase were averaged for the numerator on the left hand side of Equation 3.3. This divided by the top pressure allowed for a direct comparison to the experimental data.

The initial finite element results in Figure 2.11 showed a slightly decreasing mean stress ratio with increasing volume fraction. This trend is almost parallel to the non-dilute Eshelby model, suggesting it is a good baseline for the addition of micro-structural features. The mean stress ratio values all remain in the range of the intermediate volume fractions between 15-30%.

### **2.5.2 Irregular particle**

Micro-structural features for a composite can be often random and irregular. For high volume fraction composites, the agglomerates and aggregates become larger and increasingly irregular. Therefore, introducing this type of randomness into an RVE is important for realistic composite modeling.

Only limited initial data is present here in Figure 2.12 for the irregular particle data. A given particle volume fraction of  $\sim 23\%$  was given a degree of irregularity. This particle was then slightly rotated in random directions. The result was an increase in the stress ratio as compared to idealized FEM model. This type of micro-structural modification

to the RVE may be essential for modeling higher volume fractions where a large increase in the stress ratio occurs.

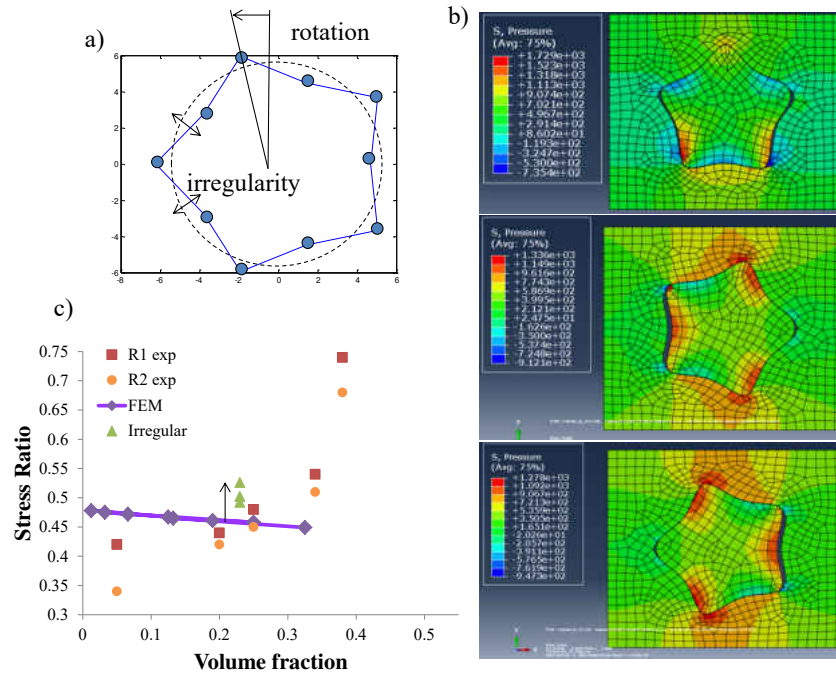


Figure 2.12: (a-b) A non circular particle generated using a Matlab algorithm which given rotation and irregularity. (b) Results are plotted for an irregular  $\sim 23\%$  volume fraction composite with varying degrees of rotation.

### 2.5.3 Interacting particles

Interacting nanoparticles are an important micro-structural feature to consider because these composites are known to contain many agglomerations with a wide variety of sizes.

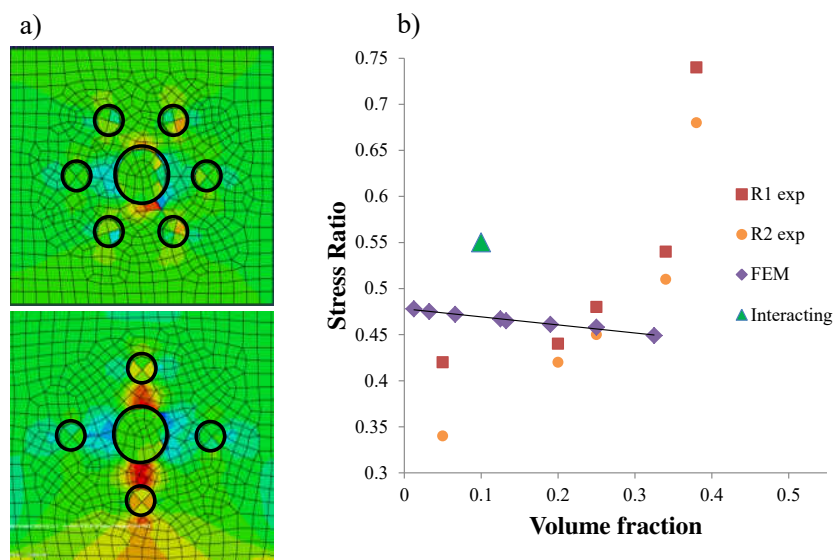


Figure 2.13: (a) Different number and orientations of interacting particles with (b) the corresponding stress ratio increase with respect to the idealized FEM model.

The method of introducing randomly orientated particles in this preliminary investigation was done by creating a circular area of smaller particle encompassing a larger particle.

Initial calculations showed that the orientation of the interacting nanoparticles is the major contributor to the magnitude of the mean stress ratio increase. Therefore, averaging of several random orientations may be necessary to accurately describe this interacting system at higher volume fractions.

#### 2.5.4 Interface effects

A system which includes a discrete isotropic interface between the matrix and particles phase has been studied with theoretical models by other researchers [70]. The challenge

with this system is that it is very difficult to measure or quantify the material properties of the isotropic interface layer [19]. Here, the interface properties used were  $E_I = 30 \text{ GPa}$  and  $\nu_I = 0.2$ .

The addition of this interface increased the mean stress ratio. Two different volume fractions were investigated, and their stress ratio dependence on interface thickness was similar. The stress ratio value increased with increasing interface thickness up to a certain limit. A maximum is reached when the interface extends to the outer boundary of the RVE. The isotropic interface could predict the phenomena at higher volume fractions. Additional interface properties could be considered such as 'soft' interface where the  $E_I$  is lower than the modulus of the matrix. Additional interface parameters could be investigated including interface elasticity effects, Isotropic constants, among others.

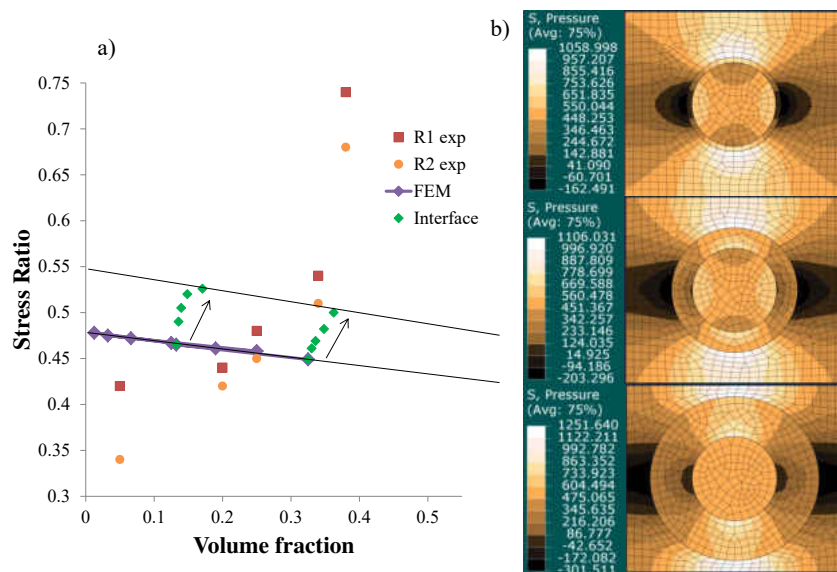


Figure 2.14: (a) The effects of an isotropic interface on the stress ratio and (b) the RVE with simulated isotropic interfaces.



### 2.5.5 Microcracks

Cracks are introduced using the XFEM interaction scheme, which all are internal to the matrix phase of the RVE. The cracks influence on the stress ratio was seen to be heavily dependent on the cracks location and geometry. The first groups of crack investigated were of straight line geometry shown in Figure 2.15a and b.

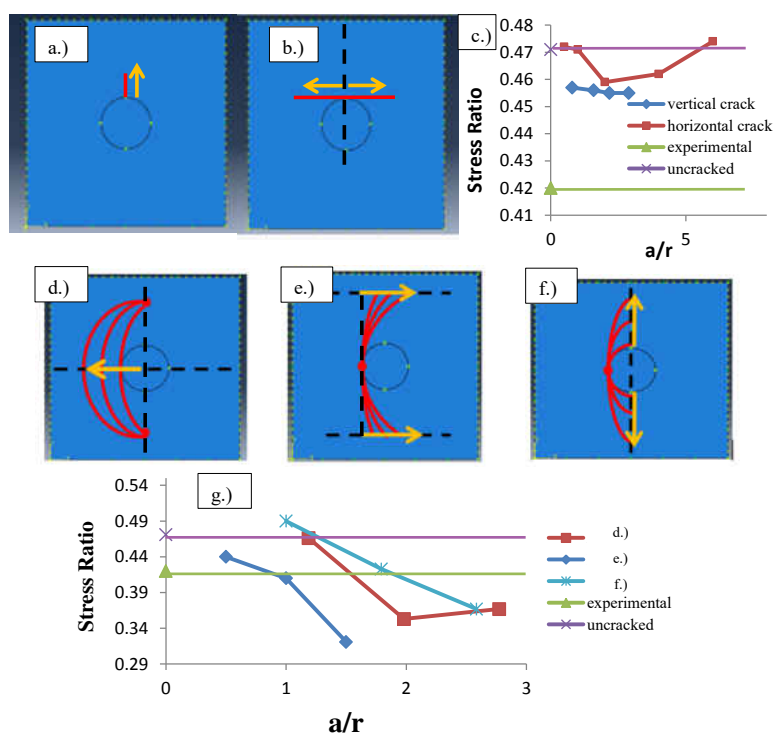


Figure 2.15: Straight cracks investigated in a (a) vertical and (b) horizontal configuration were (c) plotted with respect to the experimental data and the idealized FEM model for 5% volume fraction alumina. (d-f) Curved microcracks were investigated in terms of a few geometric parameters and (g) plotted with respect to the experimental data.

These cracks started at a point on the interface between the two phases located on the top of the particle. A vertical crack lowered the stress ratio of the particle up to

a certain crack length where the stress ratio converges to a stress ratio well above the experimentally measured stress ratio. The horizontal crack had a more sensitive stress ratio dependence that increased the stress ratio for very large and small crack lengths, with a minimum possible of being interpolated with a stress ratio similar to the vertical crack. However these simple straight edge cracks were not lowering the stress ratio down to experimentally measured values, and for some instances were increasing the stress ratio. Cracks with a starting location at a point on the side of the particle were investigated but not presented here because their stress values were exceeding the un-cracked model, and were more likely akin to matrix failure than our experimentally measured values. Stress ratios for the straight cracks on the side exceeded 0.5.

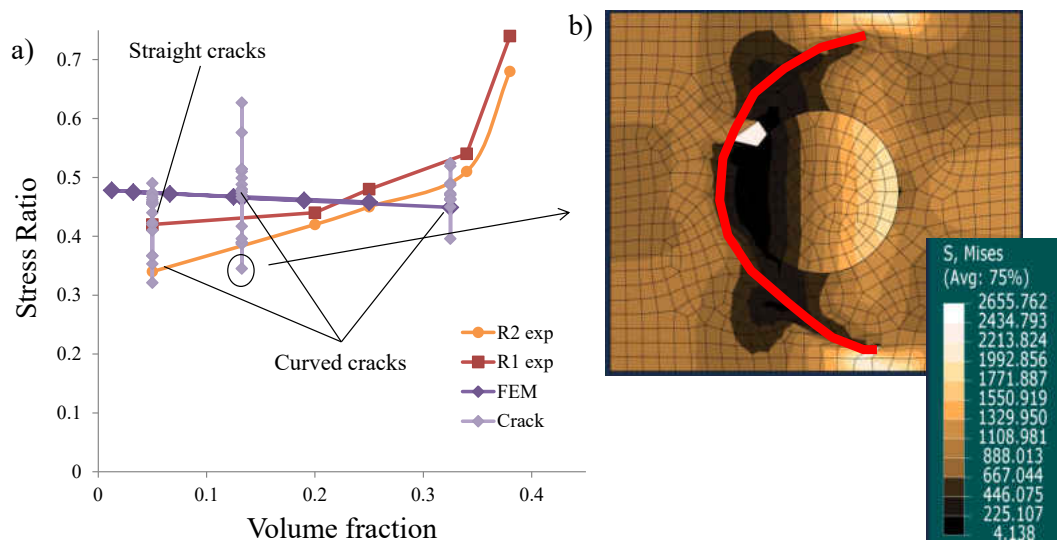


Figure 2.16: (a) Summary of the different microcrack configurations plotted with respect to volume fraction. (b) A closer look at the microcrack model that yielded a low stress ratio which correlates with lower volume fraction experimental data.

While the two prior RVE configurations investigated here only increased the stress ratio, the third included a microcrack, which could either decrease or increase the mean stress ratio depending on its orientation.

Cracks that increase the stress ratio of the particle could be ones which develop during the mechanical failure of the epoxy, resulting in more stress distributed to the inclusion as the host matrix fails. Conversely, cracks which have particular geometry, tend to decrease the stress ratio, who are more inclined to be developed as a manufacturing defect in the micro-structure. These could arise from differences in the coefficient of thermal expansion between the two phases, the way the two phases were mixed together, settling during cure cycle, etc.

The orientation of a crack could yield its origin, such as being a product of mechanical failure or from the settling and curing of the composite. A resulting decrease in the mean stress ratio could potentially aid in describing the imperfect interface between the matrix and particle phase, which could dominate particle mechanics for smaller volume fractions of a nanocomposite.

The introduction of curved cracks into the RVE were shown to have large changes in the stress ratio observed in Figure 2.16. Several different classifications of curved cracks were created here to observe various effects on the crack geometry and stress ratio. A few different instances of these geometries were tested to see which ones correlate highest with the experimentally measured value. If the crack geometries are tuned, all the configurations studied are able to exhibit the same stress ratios as the experimental data.

## 2.6 Conclusion

The Eshelby model is accurate in representing the piezospectroscopic (PS) properties for low volume fractions, but modifications were needed to predict intermediate volume fractions. An iterative technique developed by Kim that uses the framework of the Eshelby model is able to predict the PS properties for intermediate volume fractions. This prompted the development of a similar scheme that is able to apply a variety of equivalent composite property models to the Dilute Eshelby equations. The Mori-Tanaka prediction for composite properties was used as a demonstration here. The current analysis with the combined equivalent composite property models with the Dilute Eshelby gives accurate results for low and intermediate volume fractions ( $\leq 20\%$ ) which are most commonly used for alumina nanocomposite coatings.

However, these combined analytical models do not accurately predict the properties for high volume fractions ( $\geq 25\%$ ). The finite element models provided new directions to investigate high volume fractions by introducing micro-structural characteristics into the RVE. The introduction of isotropic interfaces, irregular and interacting particles improved correlation with experimental data for higher volume fractions. Microcracks included in the model were capable of creating correlation with experimental data for lower volume fractions. Future models which seek to accurately represent the micro-structures of these high volume fraction composites will likely require a combination of the investigated micro-structural effects.

## CHAPTER 3 COATING AND DAMAGE MECHANICS FOR PIEZOSPECTROSCOPIC MATERIALS

This chapter focuses on developing the necessary mechanics which describe both coating and damage mechanics for piezospectroscopic (PS) materials. First, the multi-scale mechanics of PS coatings will be described followed by the fundamentals of piezospectroscopy. Then, testing methods of different PS coatings will be presented and their related mechanics will be derived. Combining the coating mechanics with PS mechanics allows for the solution of material properties with an observed PS response. By solving for material properties using the PS response, damage mechanics can be applied. To demonstrate and validate the technique, the mechanics will be applied to previous experimental work on alumina epoxy nanocomposites. The success of this technique shows great promise for piezospectroscopy being an additional method to characterize mechanical properties. This motivated the extension of the technique to the experiments conducted in Chapters 4 and 5 to quantify damage of coatings and underlying substrates.

### 3.1 The Mutli-Scale Problem of PS Nanocomposite Coatings

The goal of this section is to analytically relate the PS measurements to the strain or stress experienced by the underlying substrate. A variety of different mechanics are needed including piezospectroscopy, particle, and coating mechanics. A combination of these mechanics are needed to correlate the secondary mechanical measurement to the PS shift. Usually the secondary measurement is strain from a strain gage, fiber

Bragg grating (FBG), or digital image correlation (DIC). In general, DIC is the preferred secondary mechanical strain measurement because it can obtain high spatial resolution measurements and can supply a complete 2-D strain tensor. DIC combined with the high spatial resolution of piezospectroscopy, allows for an ideal calibration method of PS coatings.

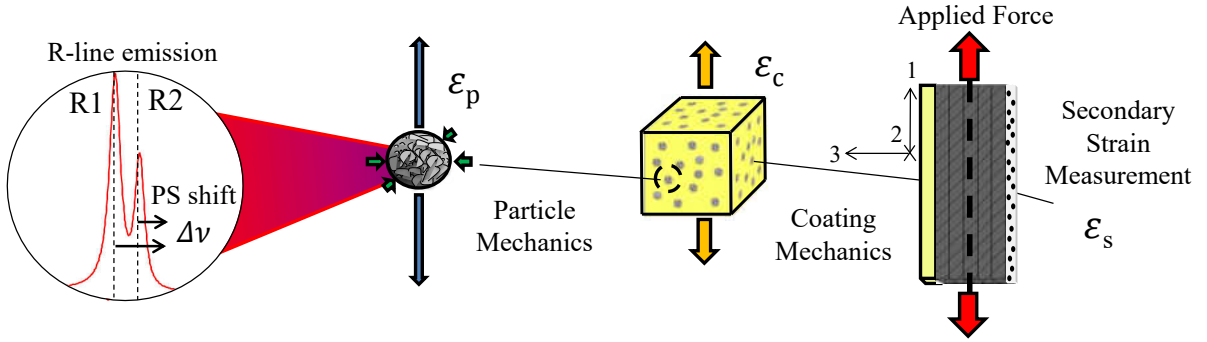


Figure 3.1: A series of illustrations that show the connection between the multi-scale problem for a PS nanocomposite coating.

### 3.2 Fundamentals of Piezospectroscopy

The spectrally active system in the  $\alpha\text{-Al}_2\text{O}_3$  micro-structure is a substitutional impurity of  $\text{Cr}^{3+}$ . The PS relationships are defined by the PL emission frequency changing with respect to local stress [41]. Generally PS properties are anisotropic when a single crystal grain is considered. However, for a polycrystalline material, the grain sizes are usually very small with respect to the probed volume. Therefore, an averaging of all the randomly oriented grains averages the principal components of the PS tensor. Historically, all of the PS relationships have been made with respect to stress out of convenience [95]. However,

the PS relationship can equivalently be expressed in terms of strain for isotropic materials using the bulk modulus ( $K$ ), where  $3K\epsilon_{ii} = \sigma_{ii}$ . In this work, it is necessary to switch between reporting with the stress and strain based PS coefficients depending on the nature of the secondary mechanical measurement. Equation 3.1 defines the first order tensorial relationship between the peak shift and the 1st invariant of stress/strain in a  $\alpha\text{-Al}_2\text{O}_3$  polycrystal. The trace of the PS tensor ( $\Pi_{ii}$ ) has a value of 7.59 and 7.61  $\text{cm}^{-1}/\text{GPa}$  for R1 and R2 respectively for  $\alpha\text{-Al}_2\text{O}_3$  [41]. It has been proposed that the differences between R1 and R2 are due to measurement uncertainty and they both could be equal to 7.6  $\text{cm}^{-1}/\text{GPa}$  [35, 65, 40].

$$\Delta\nu = \frac{1}{3}\Pi_{ii}\sigma_{ii} = K^p\Pi_{ii}\epsilon_{ii} \quad (3.1)$$

Equation 3.1 will now be slightly rearranged to be consistent with terminology used in the following sections. To express the linear relationship of the PS response, ratios are required which describe the transfer of stress/strain from the particle to the coating and to the substrate. This appears as Equations 3.2 and 3.3 for the stress and strain respectively in the particle.

$$\frac{\Delta\nu}{\sigma_{ii}^p} = \frac{1}{3}\Pi_{ii} \quad (3.2)$$

$$\frac{\Delta\nu}{\epsilon_{ii}^p} = K^p\Pi_{ii} \quad (3.3)$$

It is noted that the PS shift can be related to either the particle stress/strain or coating stress/strain depending if the coating is purely polycrystalline or a nanocomposite. Using

the assumption that the coating is purely polycrystalline,  $\sigma_{ii}^p$  in the above equations can be replaced by  $\sigma_{ii}^c$ .

### 3.3 Piezospectroscopic Coating Mechanics

This section will derive the necessary relationships between the recorded PS response and the secondary mechanical measurement. First, the 1-D coating mechanics is derived with a PS shift that are used for experiments in uni-axial tension. Then a derivation of a bi-axial strain state to a PS shift is performed which is applied to a open hole tension experiment in Chapter 5, and has the potential to be applied to a wide array of structures.

#### 3.3.1 Coating Mechanics for 1-D systems

The mechanics for 1-D PS coating-substrate system is derived. In Chapter 4, uni-axial test specimens manufactured to ensure 1 dimensional stress in the test section are described. This enables some known *a-priori* mechanics to relate PS measurements. Figure 3.2 contains an 1-D experimental schematic with secondary mechanical measurements of strain and nominal stress. This produces a PS response for both of the secondary mechanical measurements and each with their own linear relationship. The mechanics of the stress and strain based PS responses are both derived here. For the strain-based response, the relationship is defined in Equation 3.4.



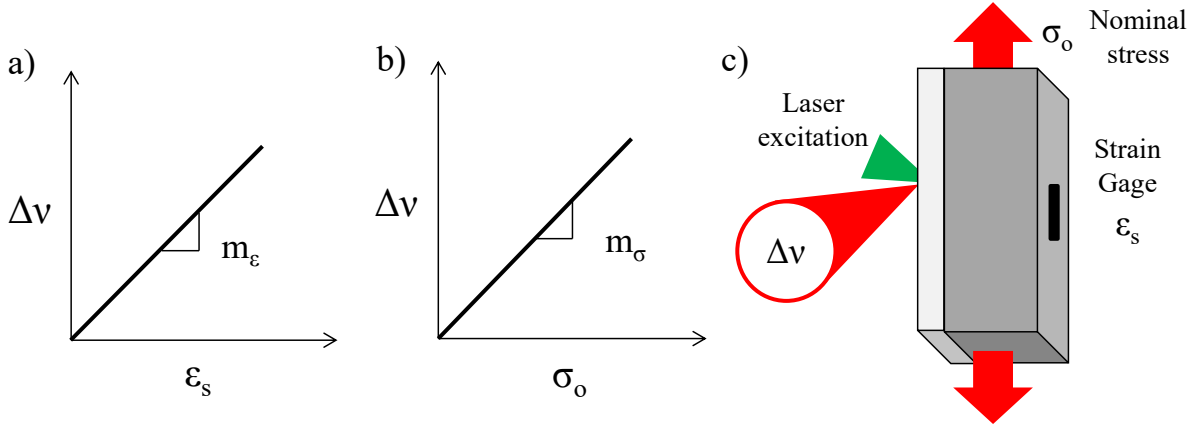


Figure 3.2: (a) Strain based and (b) stress based PS responses for different secondary mechanical measurements from (c) a 1-D tensile test.

$$m_\epsilon = \frac{\Delta\nu \sigma_c \sigma_s}{\sigma_c \sigma_s \epsilon_s} \quad (3.4)$$

For the stress based PS response, the relationship is defined in Equation 3.5. It should be noted that these above expressions are for a purely polycrystalline alumina coating. If a nanocomposite coating were to be considered then an additional ratio would need to be included as derived in Chapter 2.

$$m_\sigma = \frac{\Delta\nu \sigma_c}{\sigma_c \sigma_o} \quad (3.5)$$

Next, the ratios that make up these relationship are derived here. Consider an element of the test section in Figure 3.3 where we have a 1-D stress in the coating ( $\sigma_c$ ), substrate ( $\sigma_s$ ). The two phases have thicknesses ( $t$ ) and Elastic Moduli ( $E$ ). The strain at the interface of the two materials are equal as shown in Equation 3.7.

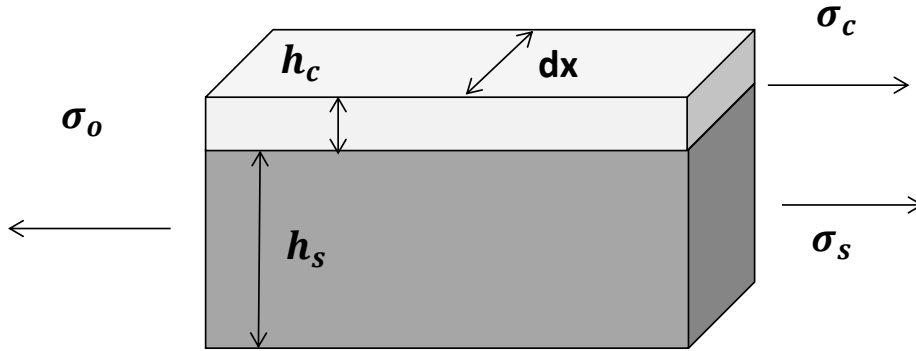


Figure 3.3: An element to perform a force balance in relating the PS shifts to coating mechanics.

$$\epsilon_c = \epsilon_s \quad (3.6)$$

From Equation 3.7, the ratio components that make up the linear relationship for the strain based PS response can be shown.

$$\frac{\sigma_s}{\epsilon_s} = E_s \quad , \quad \frac{\sigma_c}{\sigma_s} = \frac{E_c}{E_s} \quad (3.7)$$

To continue finding the ratio components for the stress based PS response in Equation 3.5 a force balance must be performed on the element in Figure 3.3. This gives Equation 3.8 that relates the nominally applied stress ( $\sigma_o$ ) to the stress in the two materials.

$$\sigma_o(t_c + t_s)dx = \sigma_c t_c dx + \sigma_s t_s dx \quad (3.8)$$

From equating the interface strains, this can now be rearranged to produce an expression which relates the fraction of stress partitioned into the coating based on the geometry and material properties of the element in Equation 3.9.

$$\frac{\sigma_c}{\sigma_o} = \frac{E_c(t_c + t_s)}{E_s t_s + E_c t_c} \quad (3.9)$$

It is convenient to have the PS response defined as a function consisting of different material properties. This allows for a solution of function of material properties if the PS response is experimentally measured. In the case of the stress based PS relationship, the nominal stress allows for a force balance of both material states, which gives an expression containing the geometrical and material properties of the element. With the strain based PS response, the relationship provided a direct material property measurement of the coating. However, for the determination of the substrate properties through the PS response for 1-D systems, it is required to use a stress based PS response.

### 3.3.2 Coating Mechanics for 2-Dimensional Systems

With the 1-dimensional coating mechanics developed, a more general derivation will be performed for systems under biaxial loading. When a sample geometry produces a non-uniform stress/strain gradient across the surface, such as for the open hole tension sample in Chapter 5, then the spatial determination of a PS shift needs to be complemented with a secondary mechanical measurement that is also spatial. Digital image correlation (DIC) is a very well developed strain mapping measurement that provides an excellent means

to calibrate the spatial variations of PS. In Chapter 5, DIC was demonstrated to be successfully used in-tandem with spatial PS measurements on a symmetric coupon with the two measurements taken on opposing faces. The mechanics of relating these two measurements will be derived in this chapter.

The derivation is performed with the end goal to relate PS shift to biaxial strain ( $\epsilon_1^s + \epsilon_2^s$ ). Biaxial strain is chosen because it can be related to the first strain invariant with a plane stress assumption. The response of a PS shift plotted with biaxial strain requires similar conversions as in the previous section. The difference is using a strain based PS coefficient, and a new coating mechanics term. The two step conversion process can be shown in Equation 3.10 where there is an assumption that the coating is pure  $\alpha\text{-Al}_2\text{O}_3$ . Similar to the 1-D derivation earlier, if a PS nanocomposite coating is considered, an additional term must be included as shown for the particulate mechanics in Equation 3.11. The subscript  $ii$  denotes the first invariant.

$$\Delta\nu = \left( \frac{\Delta\nu}{\epsilon_{ii}^c} \frac{\epsilon_{ii}^c}{\epsilon_1^s + \epsilon_2^s} \right) (\epsilon_1^s + \epsilon_2^s) \quad (3.10)$$

$$\Delta\nu = \left( \frac{\Delta\nu}{\epsilon_{ii}^p} \frac{\epsilon_{ii}^p}{\epsilon_{ii}^c} \frac{\epsilon_{ii}^c}{\epsilon_1^s + \epsilon_2^s} \right) (\epsilon_1^s + \epsilon_2^s) \quad (3.11)$$

Each term that makes up the relationship between PS shift and biaxial strain in Equation 3.10 will be shown. The strain based PS coefficient is used to relate the PS shift to the first invariant of the coating in Equation 3.12.

$$\frac{\Delta\nu}{\epsilon_{ii}^p} = \Pi_{ii} K_p \quad (3.12)$$

The second component of the relationship between PS shift and biaxial strain contains the coating mechanics contribution. This term takes several steps to derive, starting with the constraints of the 2-D element in Figure 3.4. These constraints are listed in Equation 3.13 which equate the normal stresses and the interface strains.

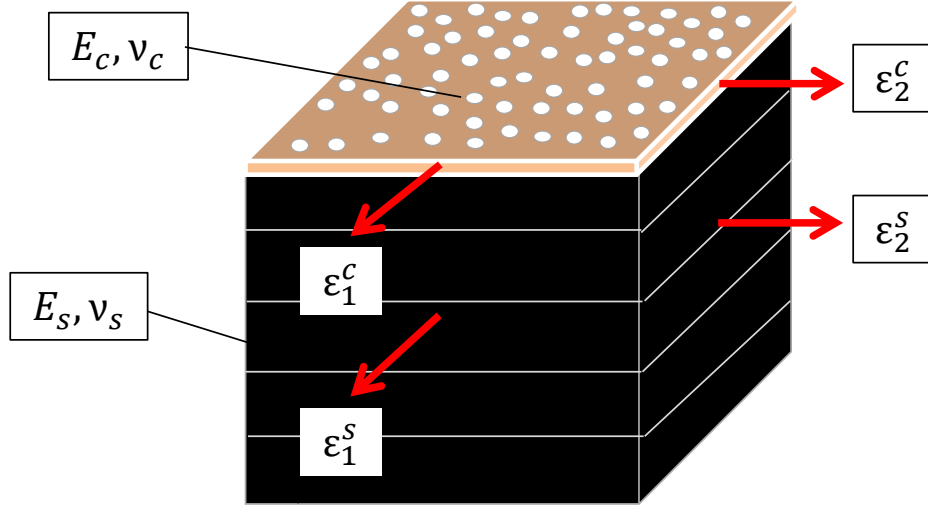


Figure 3.4: An 2-D element to perform the interface relationships between the coating and substrate in relating the PS shifts to coating mechanics.

$$\sigma_3^s = \sigma_3^c, \quad \epsilon_2^s = \epsilon_2^c, \quad \epsilon_1^s = \epsilon_1^c \quad (3.13)$$

If the coating is assumed to be in a state of plane stress, then according to the first constraint, the stress normal to the surface for both the coating and substrate must be zero. Using the remaining two constraints, Hookes law for the two phases can be used to determine a relationship between the biaxial stress of the coating and substrate in Equation 3.14.

$$\sigma_1^s + \sigma_2^s = \frac{E_s(1 - \nu_c)}{E_c(1 - \nu_s)}(\sigma_1^c + \sigma_2^c) \quad (3.14)$$

For a material in plane stress, it can be shown there is a relationship between biaxial strain and stress in Equation 3.15.

$$\sigma_1^i + \sigma_2^i = \frac{E_i(1 - \nu_i - \nu_i^2)}{(1 - \nu_i^2)(1 - 2\nu_i)}(\epsilon_1^i + \epsilon_2^i), \text{ for } i = c, s \quad (3.15)$$

By plugging in Equation 3.15 into 3.14 for both the coating and substrate, the relationship between the biaxial strain for the two phases can be shown in Equation 3.16.

$$\epsilon_1^s + \epsilon_2^s = \frac{(1 - \nu_c - \nu_c^2)(1 - \nu_c)(1 + \nu_c)(1 - 2\nu_c)}{(1 - \nu_s - \nu_s^2)(1 - \nu_s)(1 + \nu_s)(1 - 2\nu_s)}(\epsilon_1^c + \epsilon_2^c) \quad (3.16)$$

In order for the relationship to be compatible with the PS response in Equation 3.10, the biaxial strain of the substrate must be related to the first strain invariant of the coating. Due to the plane stress condition of the coating, the biaxial strain can be directly related to the first strain invariant in Equation 3.17.

$$\epsilon_1^c + \epsilon_2^c = \frac{1 - \nu_c}{(1 - 2\nu_c)}\epsilon_{ii}^c \quad (3.17)$$

Finally, by combining Equation 3.17 with 3.16, the coating mechanics contribution to the PS response can be shown in Equation 3.18.

$$\frac{\epsilon_{ii}^c}{\epsilon_1^s + \epsilon_2^s} = \frac{(1 - \nu_s - \nu_s^2)(1 - \nu_s)(1 + \nu_s)(1 - 2\nu_s)}{(1 - \nu_c - \nu_c^2)(1 - \nu_c)^2(1 + \nu_c)} \quad (3.18)$$

Now the PS relationship is fully defined with a combination of PS and coating mechanics. The current assumption in Equation 3.10 is that the coating is purely  $\alpha\text{-Al}_2\text{O}_3$ . In order to include the particulate mechanics term if a nanocomposite coating is used, Equation 3.11 must be used with the expression derived in Chapter 2.

### 3.4 Mechanical Property Measurements with Piezospectroscopy

A major motivation of the current work is to quantify the mechanical properties of a composite, coating, or underlying structure through the observed PS response. In this section, the PS response will be analyzed to determine the nanocomposites elastic modulus. The material properties of the particle are assumed to be constant under any loading conditions because of their extremely high compressive strength properties [75]. The particles properties were taken to be  $E^p = 415.9$  GPa and  $\nu^p = 0.234$ . Therefore, when a nanocomposite's PS response changes it must be the result of changing mechanical properties of the nanocomposite matrix.

A previous experiment conducted by Ergin [24] examined the higher to intermediate volume fraction range where the large increases in PS sensitivity was expected to occur [92]. Strain gages were also deployed in this study to get a measure of the elastic modulus. In Figure 3.5, the PS response and the mechanical response for three volume fractions of alumina epoxy nanocomposites are shown.

The PS response will correspond to a combination of mechanical properties between the particle/coating/substrate system, or in the case of a nanocomposite, just the parti-

cle/composite system. As discussed in Section 2.4, the matrix material properties of the Eshelby equations can be exchanged with equivalent composite properties for greater accuracy. Therefore, Equation 2.13 can be rewritten as Equation 3.19 to enable composites mechanical properties to be a function of the observed PS response.

$$\frac{\epsilon_{ii}^p}{\epsilon_{ii}^c} = \frac{-3E^c(2\nu^p - 1)(\nu^c - 1)}{(2\nu^c - 1)(2E^c + E^p - 4E^c\nu^p + E^p\nu^c)} \quad (3.19)$$

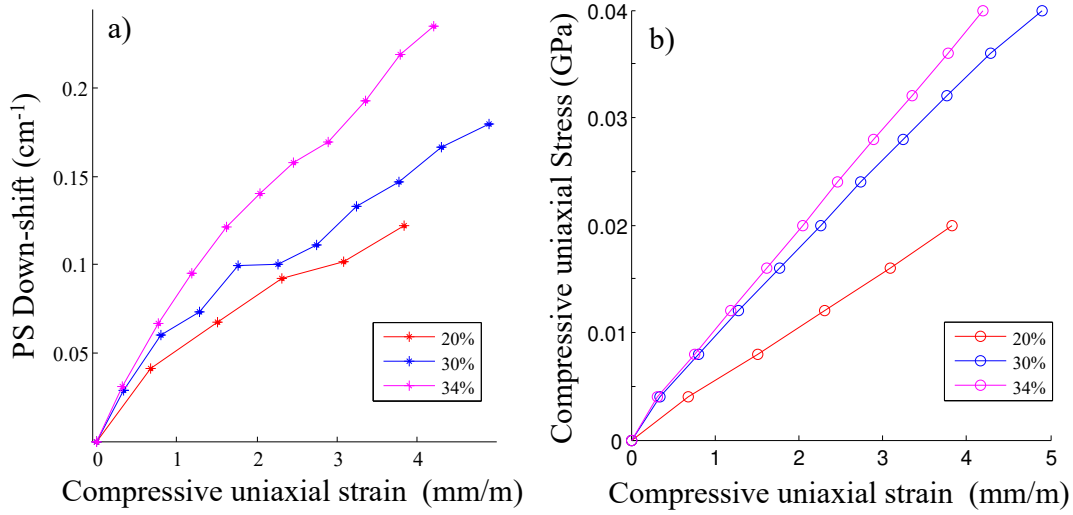


Figure 3.5: Experimental PS response and Mechanical response for varying volume fraction of alumina in epoxy nanocomposites from the work of Ergin [24].

The PS response in Figure 3.5 can be fully expressed when strain ratio of composite to particle is combined with PS relationship to the particle in Equation 3.20.

$$\Delta\nu = \frac{\Delta\nu}{\epsilon_{ii}^p} \frac{\epsilon_{ii}^p}{\epsilon_{ii}^c} \epsilon_{ii}^c \quad (3.20)$$

The PS response is defined by the linear relationship between  $\Delta\nu$  and a secondary mechanical measurement with a strain gage ( $\epsilon_1^c$ ). This would be a linear fit to the PS



response in Figure 3.5 for each volume fraction. The magnitude of this relationship is dependent on the interpretation of the secondary mechanical measurement because it is desired to relate the uni-axial strain gage measurement ( $\epsilon_1^c$ ) to the composite's first strain invariant ( $\epsilon_{ii}^c$ ). This can be done depending on the assumptions for the nanocomposite under compression.

If uni-axial stress is assumed, then  $\epsilon_{ii}^c$  can be found with the nanocomposite's Poisson's ratio ( $\nu^c$ ). Since the value of  $\nu^c$  needs to be estimated, this introduces more uncertainty into the elastic modulus calculation. By observation of the results in Figure 3.6 this created a hardening effect of the composites modulus more than doubling the magnitude of modulus values determined by uniaxial strain because the Poisson's effect effectively decreases the first strain invariant. However, when uniaxial strain is assumed, the composite's Poisson's ratio must be zero because  $\nu^c = \frac{\epsilon_2^c}{\epsilon_1^c}$  and  $\epsilon_2^c = 0$ . The reported modulus values for both cases are shown in Figure 3.6.

From inspection of Figure 3.6, the uni-axial strain appears to correlate better to both the strain gage determined modulus, as well as the modulus predicted with the Mori-Tanaka analytical solution. Additionally, the uncertainty is observed to be much larger due to the inclusion of  $\nu^c$  into the modulus calculation with the PS response. This leads to the conclusion that it is appropriate to assume uni-axial strain for a modulus prediction with the PS response.

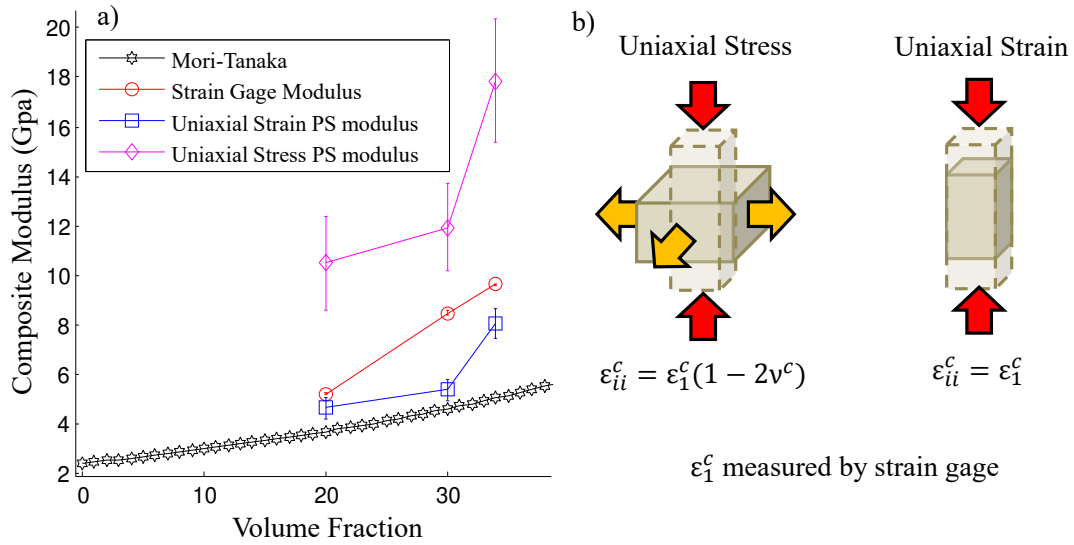


Figure 3.6: (a) Composite modulus based from calculation of the PS response with uni-axial stress/strain, the load cell/strain gage response, and the analytical Mori-Tanaka solution [72]. (b) A schematic is shown to give a physical representation on the differences between the uni-axial stress and strain assumption used to calculate the composite modulus with the PS response.

### 3.4.1 Damage Monitoring with the PS response

This section will investigate the changing PS relationship as increasing load is applied, and how that reflects changes in material properties during loading. In the previous section, the elastic modulus was calculated from a linear fit to the entire PS and mechanical response in Figure 3.5. Now, the elastic modulus will be incrementally calculated for every increasing load by simulating an unloading curve with zero plastic deformation. As discussed in Chapter 1, this simulation of an unloading curve will give an estimation

of the material state at that point. Therefore, the non-linear behavior in Figure 3.5 result in an elastic degradation of the composites material properties.

Figure 3.7a illustrates the PS response for the 20% volume fraction alumina nanocomposite, and is used to explain the method of obtaining the degradation of the elastic modulus from analysis of the PS response. If there is an assumption that there is no plastic strain, then the unloading curves can be simulated to return to the origin for every point and will be referred to as the PS state. Consider  $i$  data points on the PS response, then the  $i^{th}$  PS state ( $\Pi_i^c$ ) is proportional to the  $i^{th}$  elastic state  $E_i^c$ . By taking the linear relationship in Equation 3.20, it can be rearranged to solve for the  $i^{th}$  elastic state from the  $i^{th}$  PS state in Equation 3.21.

$$E_i^c = \frac{-E^p \Pi_i^c (2\nu^c - 1)(\nu^c + 1)}{(2\nu^p - 1)(2\Pi_i^c - 4\Pi_i^c \nu^c + 3K^p \Pi_{ii} - 3K^p \Pi_{ii} \nu^c)} \quad (3.21)$$

The assumption that the particles are resilient to any changes in its material properties still remains, which includes  $\Pi_{ii}$  since it is a property of the alumina particle. Also, the Poisson's ratio of the composite is zero for the case of uniaxial strain described in the previous section. These assumptions enable the direct solution of an elastic modulus for the composite with a measured PS state  $\Pi_i^c$  using Equation 3.21. This procedure illustrated in Figure 3.7 was repeated for the PS response for each volume fraction and compared to the degradation observed in the load cell/strain gage data in Figure 3.8. Because the elastic modulus was calculated with two methods which both contain the strain gage data, the two moduli calculated will be referred to as the PS and load cell modulus.

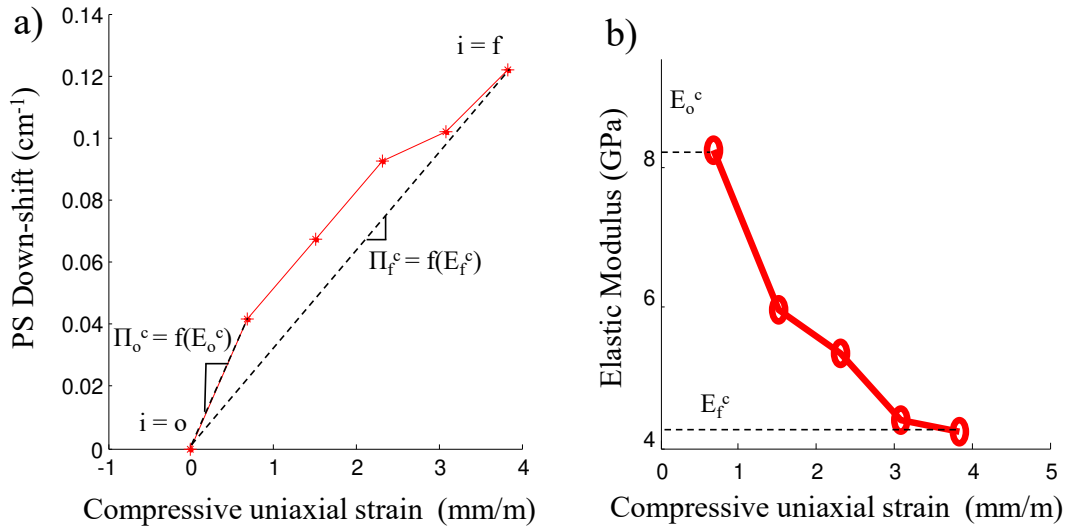


Figure 3.7: (a) The initial and final PS states marked on the PS response to be a function of the elastic states. (b) The elastic degradation computed from the PS states in (a) using Equation 3.21.

The elastic degradation appears significant for the PS modulus by inspection of Figure 3.7, reducing by an average of 50% for all volume fractions. This degradation could also be observed for the load cell modulus but its effect was not as significant. Plotted separately in Figure 3.8, both the elastic degradation from PS and strain gage data were compared for each volume fraction. Across all volume fractions, the elastic degradation of the PS modulus was significantly more than the load cell modulus.

The PS and load cell moduli values for small strain match up very well especially for 30% and 34% volume fraction. However, there are discrepancies between the rate of degradation as observed by both method and will be discussed. A strain gage is a macroscale strain measurement that represents an average of a relatively large area of the composite. The load cell data is a nominal measurement which fails to capture micro-scale

effects that the PS measurements may be picking up. For example, if initial debonding of the particle-matrix interface were to occur, this may not be realized instantly by a macroscopic measurement because it is being averaged over a large area and the small debonding region would have an insignificant effect. However, with PS response being a direct measurement of the particle strains on a smaller length scale this would be more sensitive to these microscale effects.

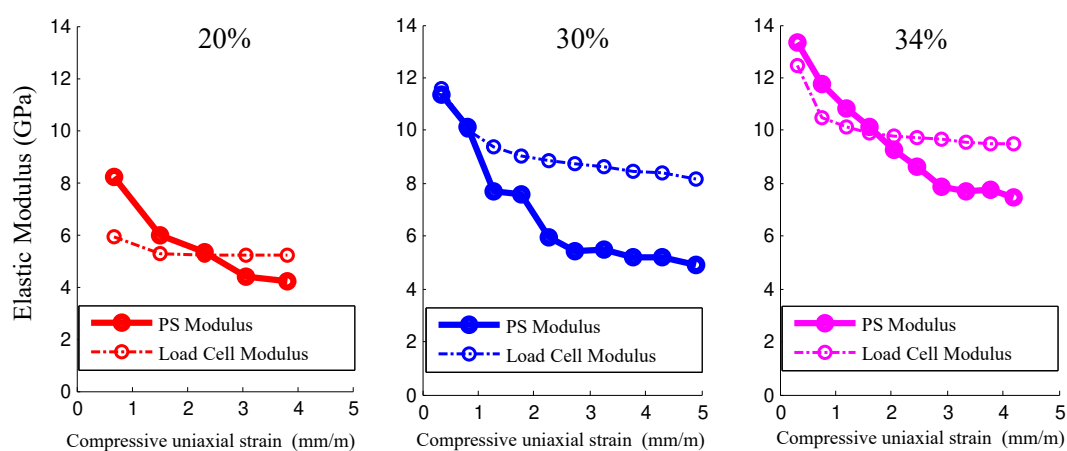


Figure 3.8: The degradation of the elastic modulus calculated from both the load cell/strain gage and PS response data for each volume fraction. The mechanics was applied to data obtained in previous work [24].

The increased elastic degradation as observed by the PS response could be a product of the micro-mechanics of the composite. At zero load and the first load steps, the modulus values appear to match up relatively well between the mechanical and PS methods. The method described here was an approximation of actual material behavior. In reality, the unloading curves include a combination of plastic deformation and elastic degradation [12]. Here, zero plastic strain was assumed which amplifies elastic degradation.

However, the same assumption was applied to both methods of calculating degradation, so the differences between the two methods are still a noteworthy observation. This difference is proposed to be a result of PS being sensitive to micro-mechanical changes in the particle-matrix interface.

### **3.5 Conclusion**

Results have shown that mechanical property measurements are possible with the PS shift and a secondary strain measurement. Using a multiscale mechanics approach, the different length scales of the particle-coating-substrate system can all be related by simple ratios of the stresses between these materials. These methods indicate a significant improvement in the understanding of PS mechanics for nanocomposites and nanocomposite coatings. With elastic modulus measurements validated to be accurate, it was shown how damage mechanics can be applied to the PS response. Now, with this improved understanding, the equations and methods described here can be applied to a wide range of alumina composite experimental data with complementary PS measurements.

## CHAPTER 4 PIEZOSPECTROSCOPY OF PLASMA SPRAY COATINGS

This chapter investigates the stress sensing of a plasma sprayed alumina coating on an aluminum substrate using piezospectroscopy. Plasma sprayed coatings have been studied extensively in literature, so a brief review of their mechanics and how they are experimentally measured will be given. Following a report of the observed PS response of the plasma sprayed coating under cyclic loading, calculations for elastic modulus of the coating will be applied from derivations in Chapter 3. These results will be compared with elastic modulus measurements from conventional strain measurement techniques and their implications will be discussed.

Plasma-spray coatings have a unique micro-structure composed of various types of microcracks and weakly bonded interfaces which dictate their non-linear mechanical properties. The intrinsic photo-luminescence (PL) characteristics of  $\alpha\text{-Al}_2\text{O}_3$  within these coatings offer a diagnostic functionality, enabling these properties to be probed experimentally at the micro-scale, under substrate loading. The piezospectroscopic (PS) measurements from the coatings are capable of revealing micro-structural stress at high spatial resolution. Here, for the first time, the evolution of stresses within air plasma spray (APS) coatings under increasing substrate loads were captured using piezospectroscopy. With mechanical cycling of the substrate, the PS properties revealed anelastic and inelastic behavior and a relaxation of residual tensile stress within the APS coatings. With decreasing substrate thickness, the coating was observed to sustain more stress, as the substrate's influence on the mechanical behavior decreased. The findings provide an

insight into the micro-structural response that can serve as the basis for model validation and subsequently drive the design process for these coatings.

## 4.1 Introduction

Plasma-spray coatings have been commonly used in the fields of corrosion and wear resistance and as thermal barrier coatings for thermal protection [16]. When included as a constituent in these coatings,  $\alpha$ - $Al_2O_3$  contributes strength at high temperatures, thermal stability, and high hardness [75]. The performance of these coatings is heavily dependent on the complex micro-structure that results from the thermal spraying process [38]. The state of stress and evolution thereof is important because of its influence on the functional properties of the coating [33].

Macro-scale stresses in plasma-sprayed coatings are characterized with a variety of methods including strain gauges [37, 83, 22] and laser displacement sensors [22, 76] for mechanical and thermal testing respectively. High-resolution micro-structural strain measurements for these coatings are available with neutron scattering [1, 51], or synchrotron X-ray diffraction (XRD) [51, 55], but piezospectroscopy is a technique that provides micro-structural strain measurements with the benefit of accessibility. Measurements are achieved with the integration of spectroscopy and loading systems for *in-situ* mechanical testing [31].

This work aims to use the spectral peaks from  $\alpha$ - $Al_2O_3$  in plasma-spray coatings to probe the micro-structural stresses in the coating directly while the substrate is subjected



to tensile loads. Effects due to the variation of substrate thickness as well as the effect of cyclic loading on the coating stress are investigated. The benefits of the PS measurements over the conventional strain measuring techniques listed above will be discussed.

## 4.2 Experimental

In this study, the pure feedstock contained 95% and 5%  $\alpha$  and  $\gamma$   $Al_2O_3$  respectively. Phase transformation occurred during processing and XRD results established that the final content was 75%  $\gamma$  and 25%  $\alpha$  phase. The 200-300  $\mu$ m thick coating was applied to aluminum 2024 dogbone-shaped specimens manufactured according to ASTM E8-04 standard [4] with 1/8, 1/5 and 1/4 inch substrate thicknesses.

The tensile cyclic loading conditions shown in Fig. 4.1c were scaled with respect to the yield stress of aluminum and stress amplitudes progressively increased to 15, 30, and 60% yield. The 1/5 inch substrate was precycled twice to 60% yield before the cyclic conditions in Figure 4.1c were applied to investigate the effects of additional loading and unloading. The steps in the loading cycle represent the force control hold for 5 minutes, allowing the probe to collect the spectral maps highlighted in Figure 4.1b. A fiber Bragg grating (FBG) sensor, shown in Figure 4.1b, was attached directly to the plasma coating to verify good adhesion between the coating and the substrate.

The hyperspectral data was obtained using an unique experimental setup [31] consisting of an integrated spectrometer, XYZ-stage, and a mechanical load frame shown in Fig. 4.1a. The maps were collected in a 12x6 snake scan pattern over a 3x1.5 mm

area outlined in Fig. 4.1b. These peak shift maps (Fig. 4.1d) were recorded for every mechanical force controlled hold (Fig. 4.1e). The spectral map edges were truncated to remove any effect of variable coating thickness on the right edge or the presence of the adhesive from the FBG on the left edge. The PS peak shift data were obtained from deconvolution of the R-lines [81] as an average of 56 data points with reference to their local zero load peak position.

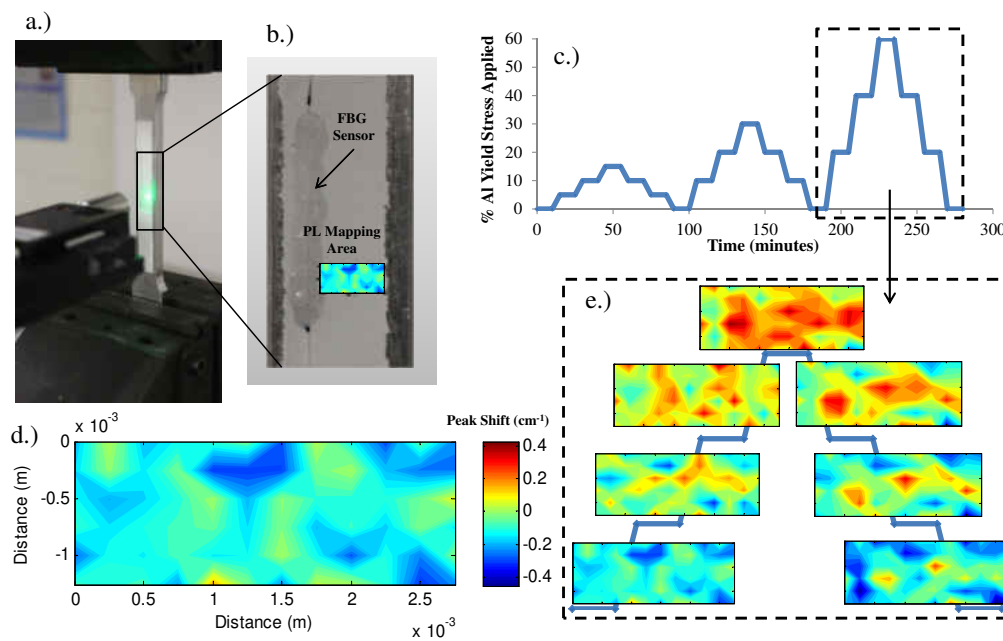


Figure 4.1: The coupled load frame and spectrometer probe setup (a), view of the gauge section (b), the tensile load cycle (c), peak shift distribution map before the third cycle begins (d), and a highlighted section of the load cycle with corresponding peak shift distribution maps (e). [29]

### 4.3 Results

The average difference between stress measured by the FBG sensor and the stress applied was approximately 6% throughout all mechanical cycles. This small difference between the applied mechanical stress and the stress measured by the FBG fiber is depicted in Fig. 4.2a and validates that the coating remained adhered to the substrate for the duration of the test.

The micro-structure of the APS coating must be considered when one interprets Fig. 4.2b. The extremely rapid cooling of molten splats from the APS process creates a layered splat micro-structure with complex geometry [58]. This creates partial bonding between the lamellar structure and when combined with the brittle nature of the pure  $Al_2O_3$  coating, it produces inelastic [83, 22] and anelastic [61] mechanical behavior.

Anelastic behavior is defined as non-linear, reversible deformation while inelastic behavior is represented by irreversible deformation. Both of these intrinsic mechanical characteristics to APS coatings were seen to be carried into the PS properties. The inelastic behavior was more evident in PS data (Fig. 4.2b) as compared to the FBG data (Fig. 4.2a) highlighting the ability to probe the micro-mechanics more directly with the piezospectroscopic measurements. Upon releasing the mechanical load, the PS measurements indicate the coating was releasing strain energy because of the relative downshift in peak position when returning to zero load. This could be a sign of relaxation of the coating's tensile "quenching stress" from rapid cooling of the molten ceramic during the APS process [51, 56, 55]. This relaxation is likely to occur from the breaking of weak bonds from the extremely brittle nature of  $Al_2O_3$ , sliding of splat interfaces during me-

chanical loading, or opening and closing of microcracks. The complex micro-structure is shown in scanning electron microscopy (SEM) images shown in Figure 4.3.

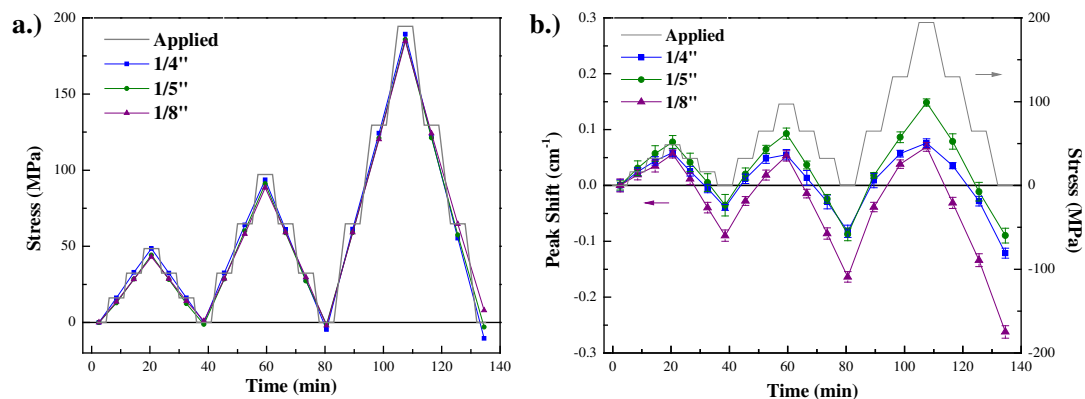


Figure 4.2: FBG sensor stress on the coating surface (a) and the PL peak shift for R1 (b) for all three substrate thicknesses. The error bars represent one standard deviation of the peak shift in the mapped area. [29]

Non-recoverable deformation occurred for all three substrates. However, the sample that was pre-cycled twice to 60% yield showed recoverable deformation in Fig. 4.4c when the inelastic behavior became anelastic with continued mechanical cycling. The two other substrate thicknesses of 1/8 and 1/4 inch have similar inelastic behavior with some recoverable response until new stress amplitudes were reached. With increasing stress amplitudes, the PS non-linearity increases.

PS properties are normally defined by just a first order PS coefficient. Preferably R2 is used for stress measurements because it behaves linearly with stress [87]. However, for the APS coating studied here R1 and R2 were both non-linear. For the lower stress amplitude cycles there was a first order relationship, but for larger amplitude cycles a higher order relationship was observed.

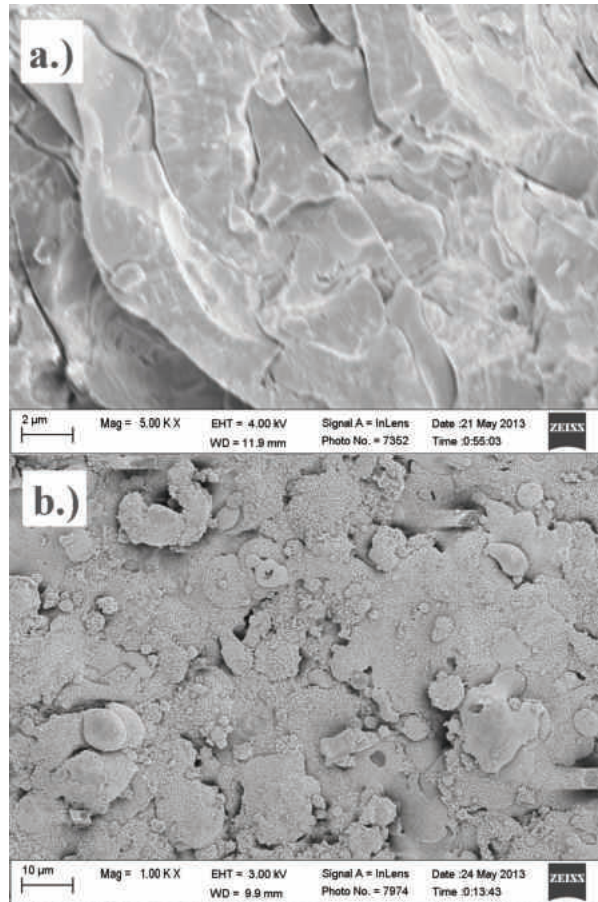


Figure 4.3: SEM images of the APS  $Al_2O_3$  coating on the 1/5 inch substrate with a cross sectional (a) and top surface (b) view. [29]

Normally, higher order PS coefficients only arise in the presence of extremely large stresses [23]. However, the APS coating's micro-structural features provide a variety of stress concentrations in the form of horizontal and vertical microcracks [56]. Non-linearities in macroscale measurements for APS coatings have been attributed to a combination of unique geometrical/micro-structural features [22] as seen in Fig. 4.3. Even for the brittle  $Al_2O_3$ , there is expected to be some finite amount of plastic deformation occurring during crack propagation [8], and could contribute to this non-linear mechanical behavior which has been called "pseudoplastic" [76].

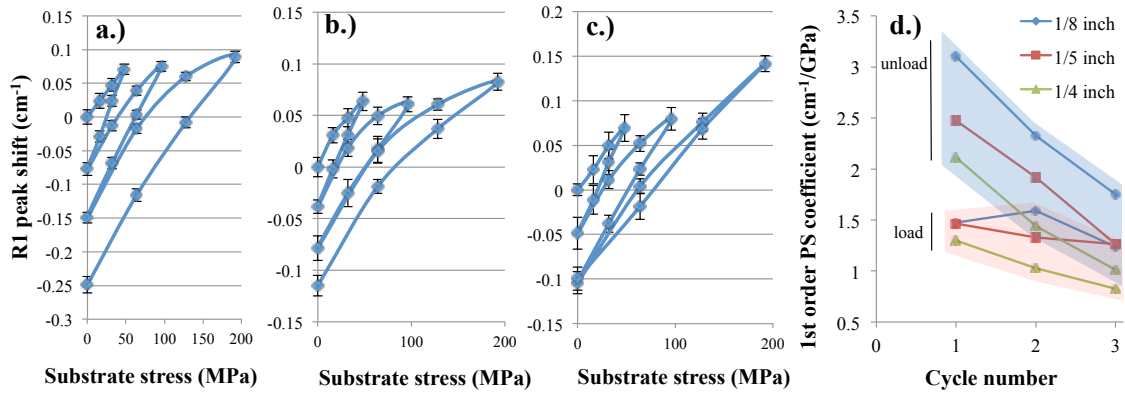


Figure 4.4: The cyclic response of the peak shift with respect to substrate stress for the 1/8 inch (a), 1/4 inch (b), and the precycled 1/5 inch substrate (c). The first order PS coefficients for each substrate thickness as a function of cycle number (d). The error bars represent one standard deviation of the peak shift in the mapped area. [29]

Figure 4.4d shows the first order PS coefficient decreasing with subsequent cycles and increasing stress amplitudes. Additionally, the PS coefficients are significantly different for loading and unloading. Consistently, the PS coefficients are larger for unloading. A stiffening behavior during unloading attributed to microcrack interfaces sticking to each other upon load reversal has been modeled in literature [61]. Also, it has been established that Young's modulus increases under compression for APS coatings because of the reduced density of microcracks from crack closures [56]. The variation in PS coefficient serve as a representation of this micro-structural behavior. A schematic for some of this behavior was illustrated in Figure 4.5.

Competing effects that control the PS coefficient were observed. Upon release of the mechanical load, the coating relaxes and gradually approaches a compressive state leading to an increased stiffness for APS coatings [61, 56]. This increases the PS coefficient as

observed between the differences for loading and unloading in Fig. 4.4d. However, the brittle nature of the  $Al_2O_3$  micro-structure makes it susceptible to various forms of micro-structural damage upon mechanical loading [56], which would decrease the PS coefficient. Overall, the additional damage with increasing stress amplitude appears to be overcoming the stiffening effect from a more compressive state. However, a constant stress amplitude fatigue study may be necessary to understand the convergence in the PS coefficient with multiple cycles. The possibility of convergence is supported by the PS response of the 1/5 inch substrate in Fig. 4.4c. This substrate thickness, preloaded twice to 60% yield, had a convergent PS coefficient for loading and unloading in the last cycle.

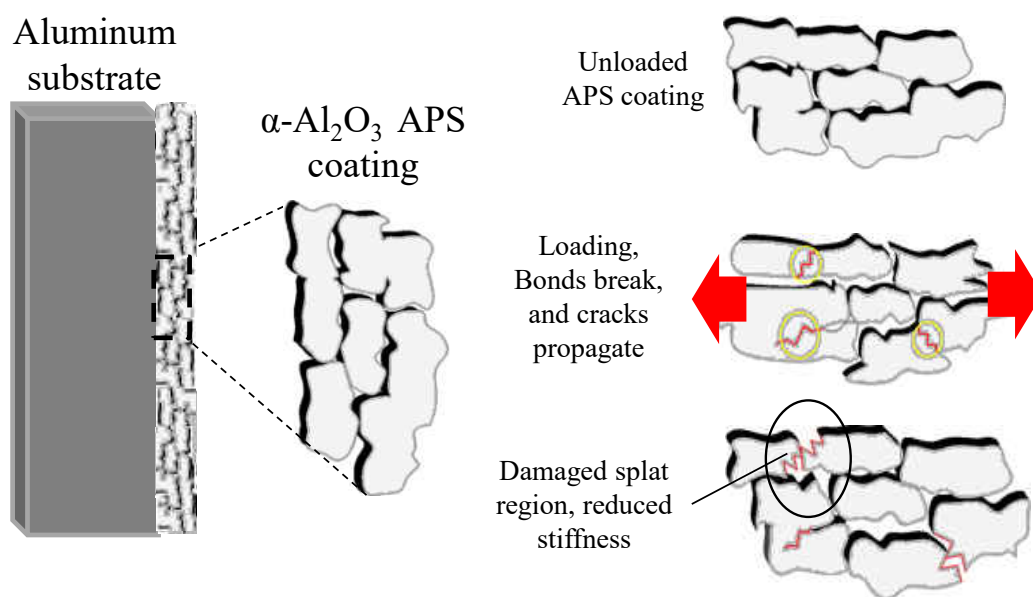


Figure 4.5: A schematic of the coating-substrate system and some insights into the micro-mechanical damage mechanisms suggested by the behavior of the PS response. [30]

Substrate thickness had substantial effects on the PS coefficient observed in Fig. 4.4d, where thinner substrates resulted in higher PS coefficients. An increasing ratio of coating

to substrate thickness causes the plasma spray coating to sustain more stress as the substrates influence on the mechanical response diminishes.

#### 4.4 Elastic Modulus of the Damaged Coating

Results suggest that the anelastic and inelastic PS response of the plasma spray coating were the result of damage to the coating itself. The experiment was designed so that the properties of the substrate do not change because the applied loads were kept well below the yield stress of aluminum. With these assumptions, the PS and FBG response for the unloading curves can be compared to observe the reduced elastic modulus. Using the PS response of the unloading curves applied to Equation 3.4 derived in Chapter 3 the change in PS coefficient can be converted into a change in elastic modulus. The results of calculating the elastic modulus from the two methods are shown in Figure 4.6.

The degradation of the elastic modulus is clearly observed with the PS response, but not observed with the mechanical response of nominal stress and FBG strain.

This further emphasizes the PS response is a more reliable method to characterize the mechanical properties of these coatings. Difference between the mechanically determined modulus and the PS modulus are proposed to originate from two main sources. (1) The FBG represents a macroscopic strain measurement that is on the order of the length of the grating  $\sim 1$  cm. (2) The epoxy used to adhere the FBG to the coating surface likely infused into the coating's micro-structure and improved the toughness of the coating by sustaining load, and reducing the stress transferred into the alumina constituent.



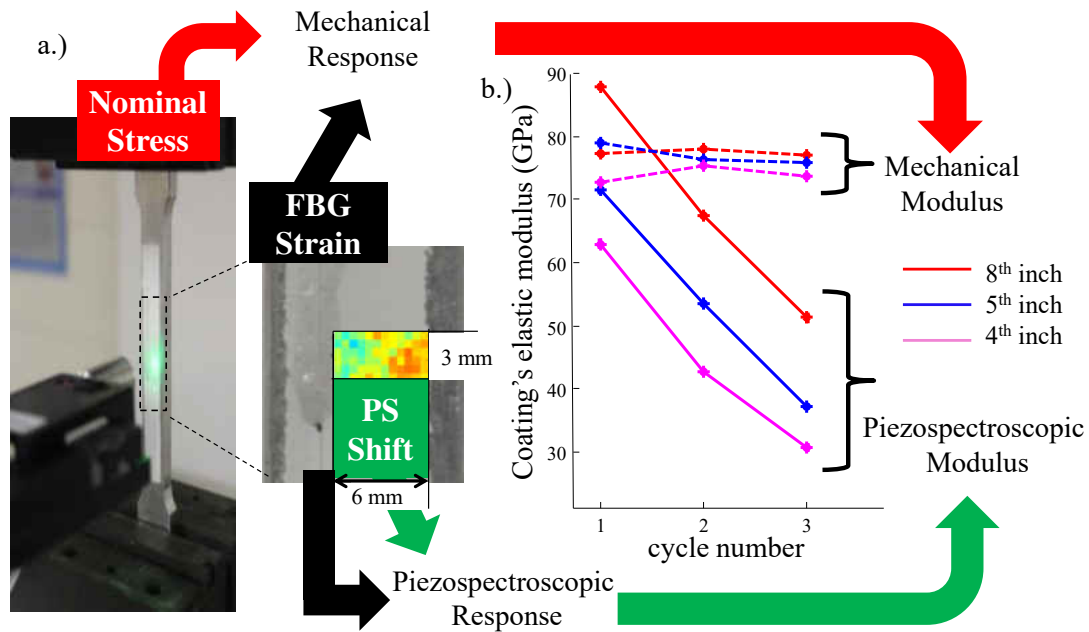


Figure 4.6: (a) A schematic illustrating the two sources of the elastic modulus measurements and (b) a comparison between the elastic modulus calculated from the two methods.

With results from the mechanical tests, additional information about the microstructure was desired. A high resolution PL map was taken for with  $40\ \mu\text{m}$  spatial resolution after the mechanical cycling in Figure 4.7a. SEM images were also taken of the coatings for further characterization in Figure 4.7b. The variation in peak position across the surface was investigated in Figure 4.7b.

The micro-structure of the APS coating was very complicated as observed from SEM images in Figure 4.7b. The extremely rapid cooling of molten splats from the APS process creates partial bonding between the lamellar splat structure [58]. When combined with the brittle nature of pure  $\text{Al}_2\text{O}_3$ , and applied mechanical loading, a variety of peak shift gradients are likely the result of microcrack propagation. Other peak position gradients

could be caused by phase distributions of  $Al_2O_3$ . Because the rate at which the splats cool determine its phase [102], peak position gradients are expected in locations such as at the coating's edge where the splats are presumed to cool faster. The high resolution peak position image of the coating's surface help substantiate that the incremental downshift for new stress amplitudes are the result of splat bonds breaking.

A relatively lower peak position was observed on the left side of the coating which was a region between the FBG and the edge of the coating. This demonstrates the invasive nature of the epoxy which adhered the FBG to the coating.

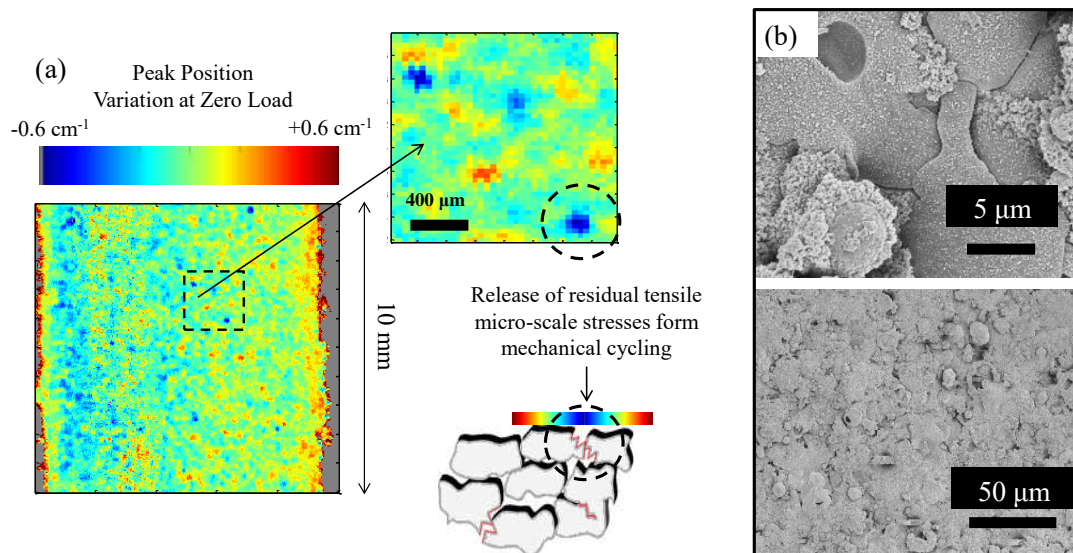


Figure 4.7: (a) Peak position photoluminescence map and (b) SEM images of the APS coating surface.

It is proposed that because the area under the FBG was hardened by the epoxy infusion into the splat micro-structure, the region adjacent to the FBG suffered enhanced damage. This may also combine with a weaker alumina micro-structure closer to the edge of the coating which cooled faster [102].

## 4.5 Conclusion

The coating's micro-mechanics were observed *via* piezospectroscopy with mechanical cycling of the substrate, demonstrating the capability for observing the  $Al_2O_3$  micro-structural behavior. The addition of reinforcing materials into the APS feedstock, such as Aluminum particles [103] or Carbon nanotubes [7], has been shown to increase fracture toughness, prolong fatigue life and decrease the non-linear behavior [56]. PS could be used to assess, through micro-structural studies, the mechanical improvement from these reinforcements more effectively than conventional mechanical measurements.

In conclusion, the plasma-spray  $Al_2O_3$  coating showed distinct PS properties indicative of the complex micro-structural changes under substrate load. The ability to observe the micro-mechanics of coating deformation under mechanical cycling of the substrate with micron level spatial resolution substantiates that PS measurements are advantageous for engineering these coatings. Here, it was shown how piezospectroscopic data serve as micro-mechanical measurements that can supplement the design of plasma spray coatings. Future work will target higher spatial resolutions, cyclic fatigue tests, and SEM studies correlating microcrack density with the convergence or variation of the PS coefficient.

## CHAPTER 5 PIEZOSPECTROSCOPY OF COATED OPEN HOLE TENSION

### SAMPLES

This chapter focuses on a unique experiment to demonstrate the ability of a PS stress sensing coating. Here, the stress-sensing behavior of an alumina-epoxy nanoparticle coating applied to a composite substrate in an open hole tension (OHT) configuration, is shown under tensile loads. The evolution of stress-sensitive PS shift maps were validated with a biaxial strain field which was concurrently measured through digital image correlation (DIC). It is proposed that the many failure mechanisms were observed with the PS coating including matrix micro cracking, initial fiber failure, and progression of fiber failure. Using the mechanics described in Chapter 3, the elastic modulus of the composite was calculated spatially during loading, and by applying the principles of damage mechanics, the elastic degradation during mechanical loading was observed. This chapter demonstrates the effectiveness of utilizing piezospectroscopy with high spatial resolution capabilities and applied nanocomposite mechanics. Applications for piezospectroscopy range from non-invasive structural integrity monitoring in the aerospace and civil fields to advanced mechanical characterization in emerging materials research.

### 5.1 Experimental Setup

To develop the most effective PS nanocoatings, the host matrix for the  $Al_2O_3$  nanoparticles should have some degree of transparency, the  $Al_2O_3$  nanoparticles should be well dispersed, and the coating should have excellent adhesion to the substrate. The PS

nanocoating investigated in this work was manufactured by Elantas PDG, Inc. by mixing 150 nm  $\alpha$ - $Al_2O_3$  nanoparticles (Inframat Corp.) with 99.8% purity in epoxy to achieve a 20% volume fraction of particles. The coating was applied to an OHT composite substrate consisting of laminated IM7-8552 unidirectional tape manufactured and tested in accordance with ASTM standards [5].

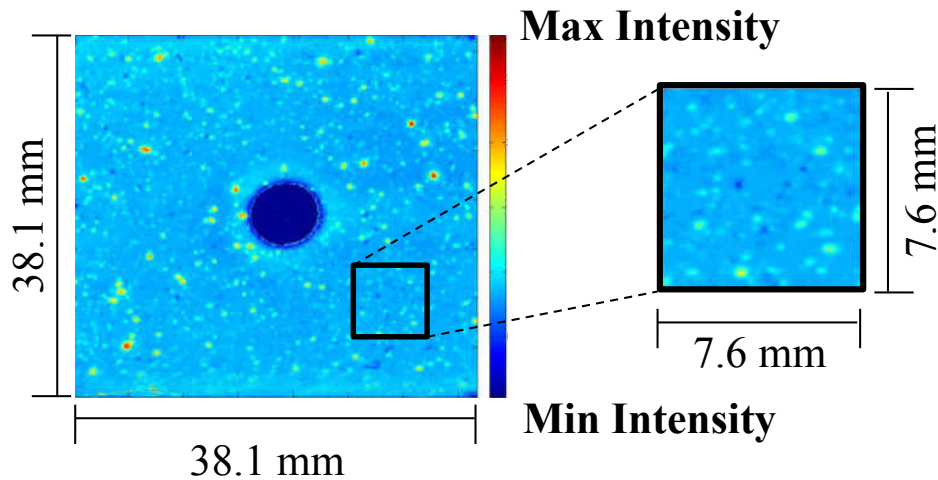


Figure 5.1: High spatial resolution intensity map quantifies coating dispersion.

Nanoparticle dispersion is of high concern as the nanoparticles have a tendency to agglomerate, thus affecting the load transfer mechanics [49, 32, 28]. To inspect the quality of the dispersion, a high resolution PL intensity map was taken similar to previous work [91], with a spatial resolution of 70 microns as shown in Figure 5.1. This map revealed adequate dispersion with the average size of agglomerations in the micron range.

The sample was loaded at a rate of 0.05 in/min and held at discrete force increments as shown in Figure 5.2a using displacement control during holds. This maintained constant substrate strain and avoided creep during the higher loads, but this prompted stress

relaxation as observed in Figure 5.2a. During each hold, PS and DIC measurements were collected on the front and back side of the substrate, respectively.

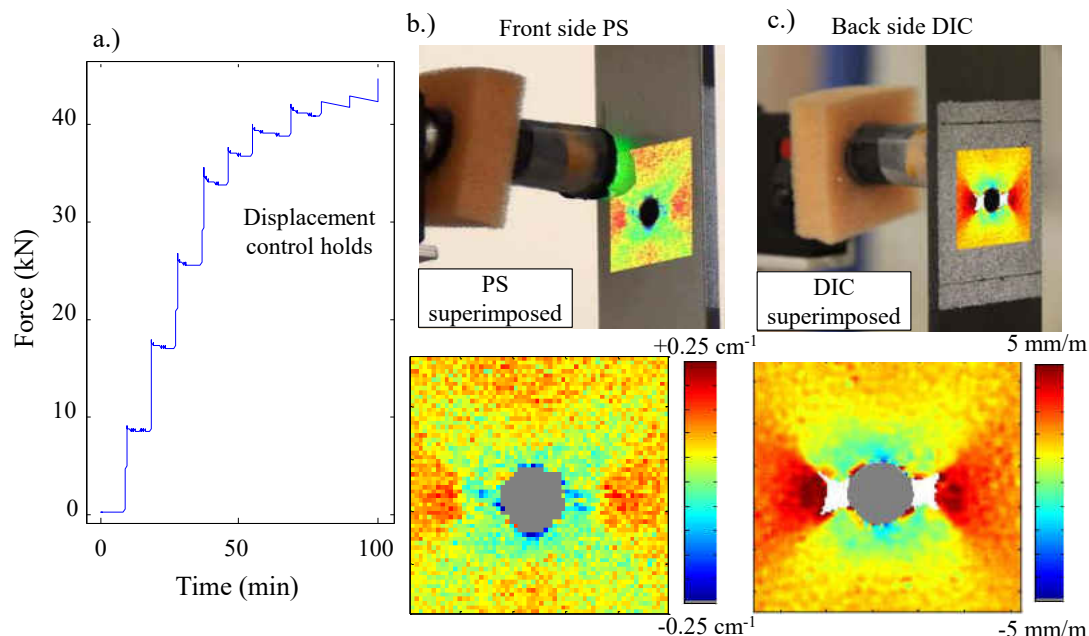


Figure 5.2: (a) The load history plot indicating the displacement control holds. (b) Front side PS and (c) backside DIC data were collected on opposing faces. PS shift and biaxial strain ( $\epsilon_x + \epsilon_y$ ) maps are shown for 96% failure load. The hood around the optical probe was implemented to reduce the noise resulting from room lights.

PS data were collected with a prototype portable spectrometer system designed to have field capability with a 1200 groove/mm grating and a CCD (Princeton Instruments). Excitation was achieved using a low power, 1.5 mW laser of 532 nm wavelength with an exposure time of 100 ms per collection. A back scattering configuration was used with a long working distance objective mounted on an optical probe. The PL spectra on a 60x60 grid during a snake scan, implemented using a synchronized translation stage with a measurement area of 25.4 square mm, corresponds to a spatial resolution of 0.4 mm.

With these settings each map is collected within about 8 minutes. The DIC measurements were relatively instantaneous compared to piezospectroscopy. Its images were collected at the start of every hold for comparison with piezospectroscopy.

The PS shift and DIC biaxial strain maps were shown in Figure 5.2b and c. Here it was indicated there was good qualitative agreement between the two techniques. The most significant difference between the two measurement techniques occurs in the region adjacent to the open hole.

In these areas, the DIC was indicating an extremely high tensile strain for this material, which was filtered out and presented as the whited out areas in Figure 5.2c. In this region where the DIC algorithm breaks down, PS was recording large PS shift gradients these locations. One noteworthy finding is that the PS shifts in this area are negative which is normally an indicator of compressive stress, but here may be indicating a stress relaxation behind a progressing crack tip. This phenomenon, as well as other features in the PS data, will be explored and discussed in the following section.

## 5.2 Results

The results of this experiment are extensive because of the massive amount of data and the significant amount of interpretation it requires. This section will begin with an in depth qualitative comparison between the two methods by inspection of PS shift and DIC biaxial strain maps. Next, correlations between the observed characteristics in the PS response to the mechanical behavior of these composites. At that point it will become

clear that a PS coating is capable of may be indicating the progression of subsurface failure modes within the composite.

### 5.2.1 Qualitative Inspection

This section begins with a qualitative inspection and comparison of the PS shift and DIC biaxial strain maps. This will be followed by several proposals of what the PS data is indicating by its unique evolution throughout the tensile test. This will serve as an initial inspection of the data before a more detailed and robust analysis is preformed on the unique data set collected in this experiment. Figure 5.3 shows the PS and DIC maps collected for all the mechanical loads. It can be observed that the two measurement methods are similar, but have distinct differences which will be discussed.

At the start of the test, it can be observed that the DIC shows a gradual increase in the intensity of the strain distribution around the open hole, while the PS results show a rapid increase at the first load then approaches a steady state for the next few loads.

The next interesting artifact of Figure 5.3 is the negative peak position gradient that emerges adjacent to the open hole at 76% failure load. It is known *a-priori* that this region should be experiencing large tensile strains, and this is also what is indicated by DIC. A very similar initial failure region seen in the 0° ply was observed in a simulation of a quasi-isotropic open hole tension specimen [11]. At 76% failure load, the composite coupon has likely sustained damage and this negative peak position gradient close to the open hole may be an indicator of initial fiber failure.



At 88% failure load, a relative negative PS shift was observed across most of the sample surface with respect to the PS shift at 82% failure load. This would be equivalent to a maximum nominal stress value that has been reached on an engineering stress/strain curve. This location is an important turning point in the mechanical test that may indicate the onset of critical damage. Literature has described a redistribution of stress occurring once subsurface damage has developed [71].

Next, at 92% failure load, two events were observed. (1) A large propagation of the negative PS shift gradient adjacent to the open hole. (2) The DIC algorithm calculates unreasonably high strain and was filtered out with white pixels. There are likely major structural changes occurring within the substrate that cause both of these events.

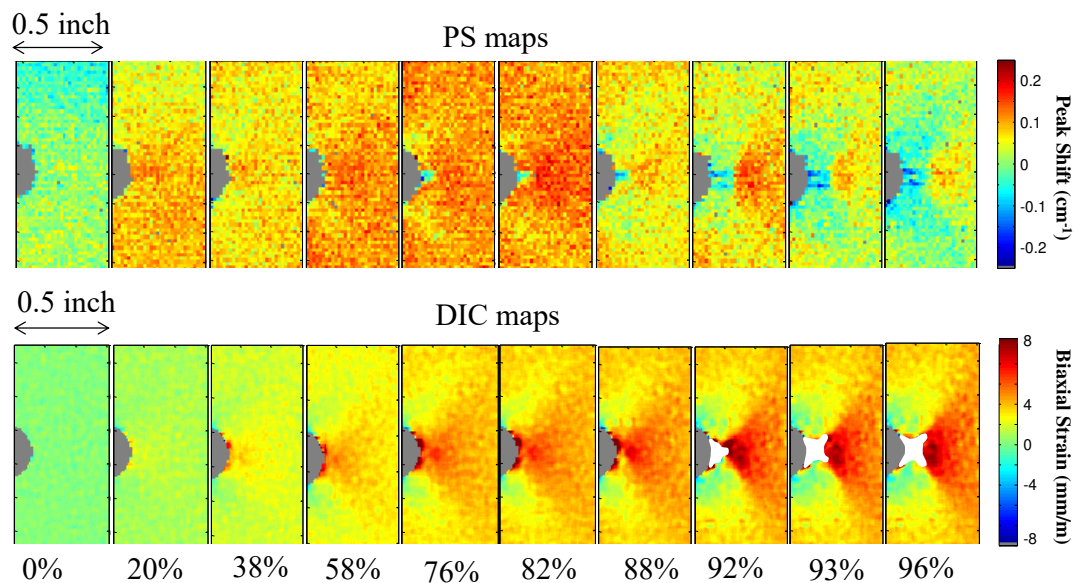


Figure 5.3: The evolution of PS shift and biaxial strain maps for half of the open hole tension sample with percent failure loads listed.

The remainder of the test exhibits a continued propagation of the negative PS shift gradient, and an increase in size for the region where the DIC algorithm becomes un-

reliable. From inspection of the test as a whole, the PS shift maps do not show many gradients across the surface until the last few maps. Before then, only a small gradient close to the hole was observed starting at 76% failure load. These gradients are proposed to be induced by initial cracking of the composite, represented as local reductions in the substrates stiffness. The coincidence, of the DIC algorithm break down with the large propagation of the PS shift gradient, support that this is an indication of damage.

### 5.2.2 Inspection of the Damaged Zone

In the previous section, it was observed that a critical region exists just adjacent to the open hole where both the DIC algorithm breaks down and large PS shift gradients exist. A detailed examination and discussion of the PS shift maps in this critical region was highlighted in Figure 5.4. The highlighted regions were plotted with increasing loads to qualitatively observe the PS shift gradients in this region with more detail.

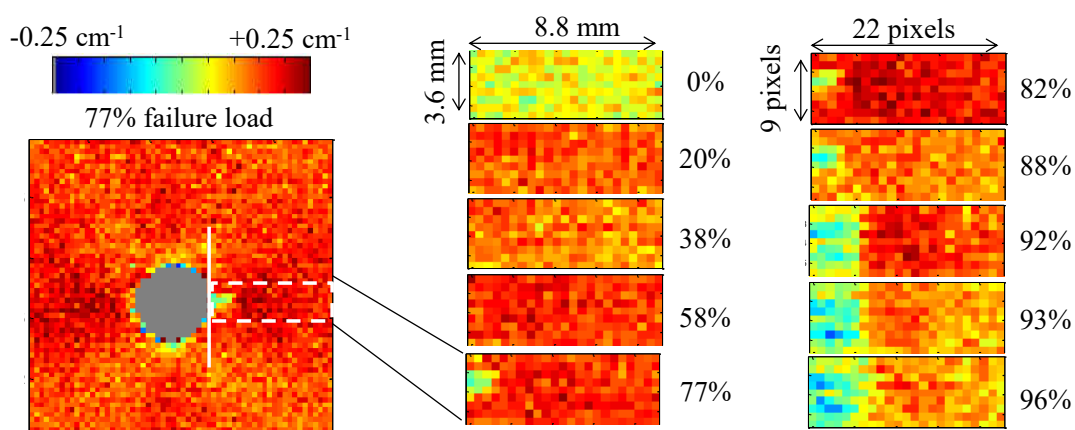


Figure 5.4: PS shift maps for a region close to the open hole which was highly damaged during loading. The percentage of failure load is indicated to the right of each map.

PS measurements at 0%, 58%, 77%, 92% and 96% of failure load were selected for further analysis shown in Figure 5.5a. For each map, the PS shifts were averaged in the vertical direction as a function of distance from the open hole. The averages are shown in Figure 5.5b. The PS shifts at 58% failure load show the expected upshift with increasing tensile load. The error bars for the 58% failure load are the standard deviation over the vertical distance and are representative of all loads.

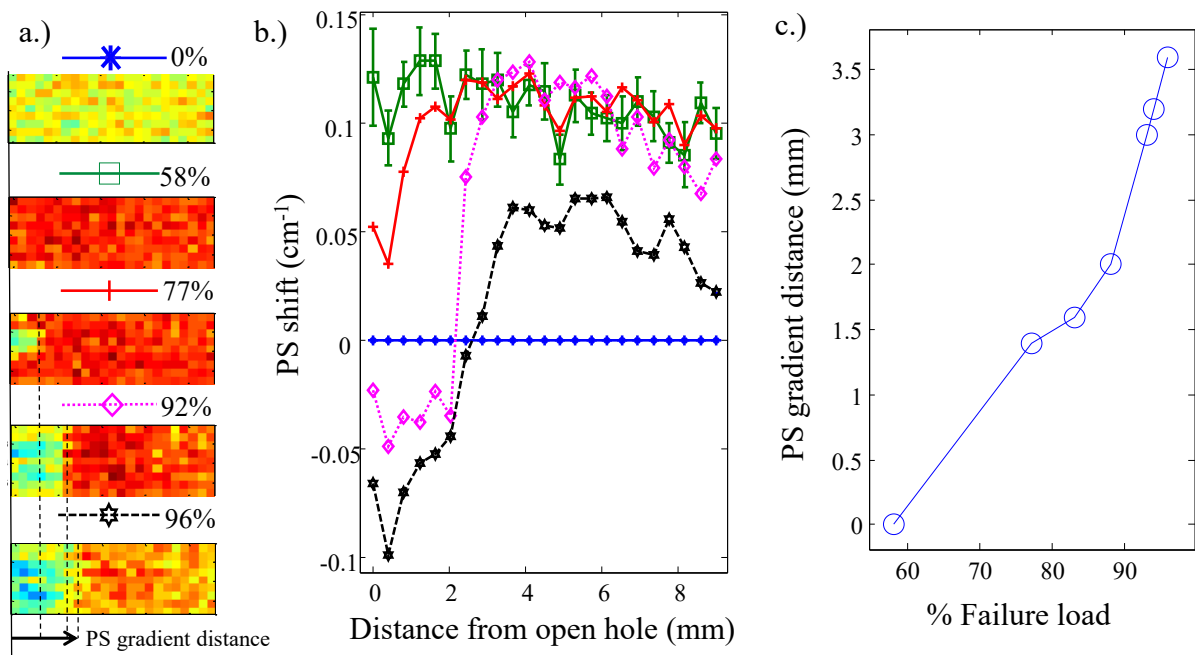


Figure 5.5: (a) Selected PS shift maps of highlighted region for further analysis. (b) The PS shifts of selected highlighted regions plotted with respect to distance from open hole. (c) PS gradient distance from pixel count and across the highlighted region.

At 77% of failure load, the PS shifts are still positive; however they are lower in magnitude in comparison to 58% of failure load. At 77% failure load there is also the introduction of relative downshift near the hole edge. The red line in Figure 5.5b shows the PS shift is approximately  $0.05 \text{ cm}^{-1}$  at the edge of the hole and then steadily increases

to a constant value of  $0.1 \text{ cm}^{-1}$  at  $2 \text{ mm}$  distance from the hole. This continues from 77% to 92% with an increasing PS shift gradient magnitude. As the composite approaches failure, the PS shift gradient is so large that the PS shifts become negative (below the zero load reference). Usually negative PS shifts would indicate compressive stresses on the particles, but the sample is in tension. The cause of the negative PS shifts is suspected to be a loss in local substrate constraints to the coating.

Figure 5.5c is a quantification of the size of the region that is most affected by the PS shift gradient. At each load, the number of pixels which are affected by the PS shift gradient are counted starting at the hole and ending where the PS shift gradient reduces and the PS shifts reach a steady state. Figure 5.5 shows that the growth of the PS gradient is steadily increasing with applied load and could be an indicator of the damaged area size.

### 5.2.3 Correlation to Progressive Composite Failure

This section will focus on the comparison of the observed PS response to what is expected of a composite sample when loaded until failure. When investigating the evolution of the PS patterns throughout the tensile test in Figure 5.3, a variety of phenomena were observed. To assist in the discussion, the results of the loading test were broken into 4 different regimes, chosen to be similar to other works describing the progressive failure of composites [44]. Additionally, a local PS response was chosen which was at a distance away from the open hole and plotted in Figure 5.6c to be analogous to a mechanical stress/strain response of a composite.

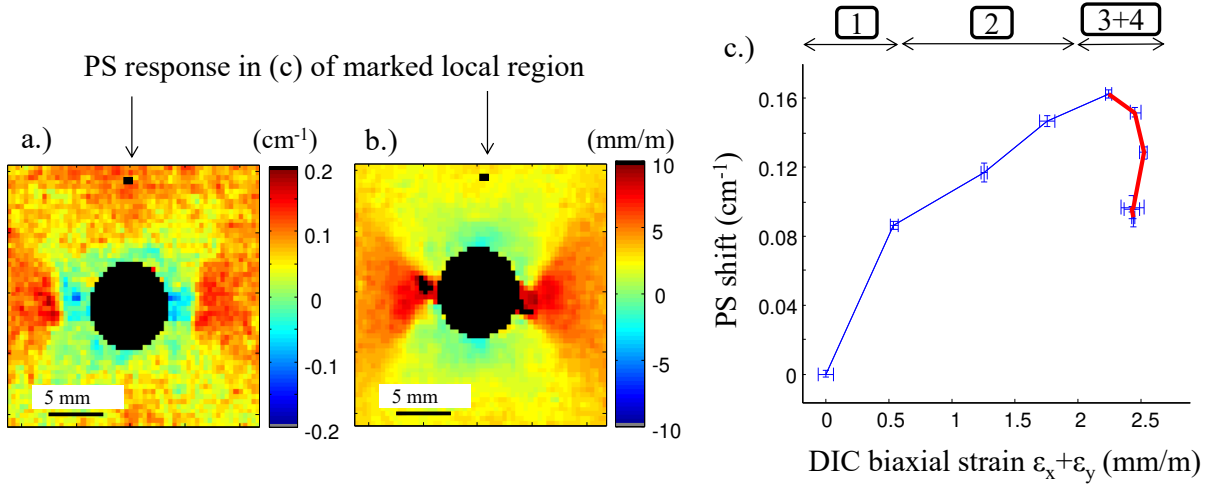


Figure 5.6: (a) The PS shift map and (b) DIC biaxial strain map for 92% failure load. (c) The PS response for the marked region in (a) and (b). These figures were created with a post processing procedure described in the Appendix.

In brevity, the four regions as shown in Figure 5.6c correspond to (1) linear continuous upshifts without the observation of damage, (2) change in slope of the PS shifts, (3) initiation of asymmetric PS shifts transverse to the open hole, and (4) widespread propagation of negative PS shifts emanating from the open hole.

Figure 5.6c shows that as the tensile load is increasing, the PS shifts are positive until a maximum PS shift is reached, at which point further application of tensile load provides a softening of the PS shift. This phenomenon, referred to as PS drop, is intended to be analogous to load drops during failure initiation in mechanical testing [44], but in terms of a PS shift rather than load. Since piezospectroscopy provides a spatial measurement, local initiation of failure mechanisms could be observed.

The mechanical response of a typical fiber composite has 4 regions as it reaches failure as described by Hufner [44]: (1) linear elastic behavior (2) onset of matrix micro cracking

(3) onset of fiber failure and (4) progression of fiber failure. These four regions may correlate to the observed PS response mentioned earlier. The PS drop, associated with the start of the third region at 77% failure load, could be an indicator of initial fiber failure. Further work is required to confirm this hypothesis and any other conclusions of how to relate the four regions of composite failure progression to the four regions of PS behavior seen in Figure 5.6c.

From comparing the observed PS response in Figure 5.6c to the typical mechanical behavior of a composite explained by Hufner [44], the similarities are evident. The PS response may be directly proportional to the mechanical behavior of a local region on the composite. If this is the case, piezospectroscopy may be the key to experimentally probing the local progression of failure in these composites where significant efforts have been made to simulate them [11]

### **5.3 Applied Damage Mechanics**

Previously it has been shown through the PS shift maps and the PS response, damage mechanisms are being observed. This now provides the basis for the next part of the analysis which is applying damage mechanics to the PS responses across the sample. A detailed analysis will be performed which attempts to combine the multi-scale mechanics with simple damage mechanics developed in Chapter 3 to the data collected from the open hole tension experiment.

### 5.3.1 Elastic Degradation and Plastic Deformation

The goal is to use the PS response to estimate the degradation of material properties. The PS state must first be determined before a material property calculation, outlined in Chapter 3, can be applied. The PS state will be defined as the slope of the simulated unloading curve (in the absence of experimental unloading data) in the PS response. In this work, the PS state was determined using two different methods: (1) purely elastic degradation, and (2) elastic degradation with plastic deformation.

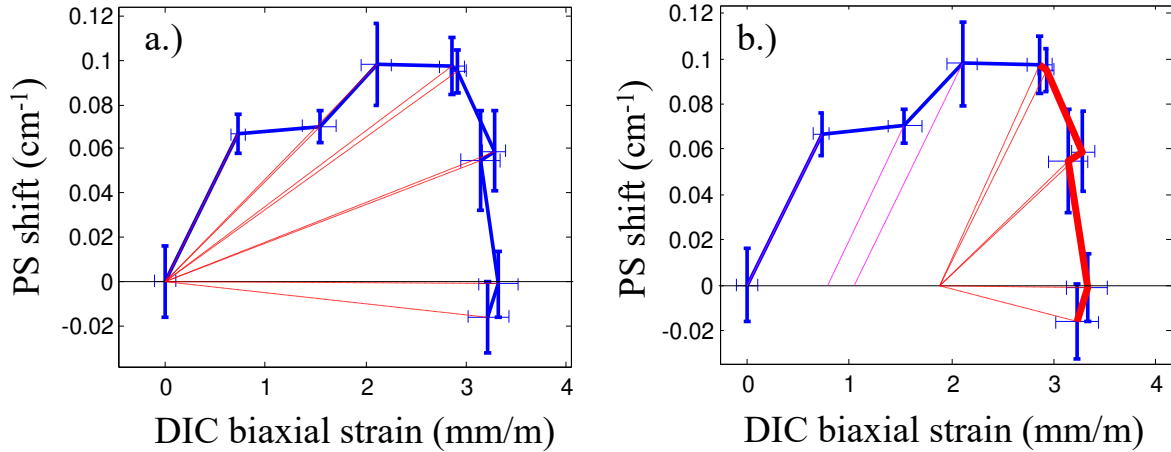


Figure 5.7: (a) The simulation of the unloading curves for a PS response using purely elastic degradation and (b) elastic degradation with plastic deformation until the max PS shift.

Purely elastic degradation simulates a PS state which returns to the origin as shown in Figure 5.7a. This would be equivalent to zero plastic deformation. This is an approximation of actual material behavior, but it is a simple one that allows for preliminary analysis [12]. The second model simulates some plastic deformation until the maximum

PS shift is reached. The initial PS state was applied to all loads until the maximum PS shift. Further loading past the maximum PS shift then kicks in elastic degradation, as shown in Figure 5.7b. This trigger of the maximum PS shift was intended to be a simple indicator of the onset of critical damage occurring.

The two different models were applied to each PS response across the sample's surface. Then, maps of the PS state can be created for every loading point. The two methods are compared in Figure 5.8 for selected loads. Both methods are identical for 20% failure load. A general observation is that the PS state is lower to the left and right of the hole when compared to above and below the hole.

A closer look unveils that a negative PS state is present in areas directly above and below the open hole. These areas are in a compressive strain state as measured by DIC, but record a tensile PS shift. The result is a negative PS state, which is indicated by white pixels. At the higher loads, a large portion of the sample's surface also has a negative PS state, due to the negative PS shifts and tensile DIC strains.

The elastic degradation (ED) model shows a rapidly degrading PS state, while the elastic degradation model with plastic deformation (EDP) remains relatively unchanged in comparison up to 82% failure load. With close observation, the EDP model does have degradation in the region just adjacent to the open hole where the PS shift gradients appear at 76% failure load as described in the previous sections.

At 82% failure load, the PS shift has generally reached its maximum for most of the sample's surface. Therefore, at the next load increment of 88% most of the elastic degradation has been triggered for the EDP model. Further application of load further



reduces the PS state across the samples surface. Some patterns are observed in the maps for the higher failure loads. Areas of white pixels are regions of negative PS states as discussed earlier and they appear to make patterns of  $\pm 45^\circ$  from the open hole. These patterns are very similar to the matrix cracking patterns observed from an x-ray image of an open hole composite [71]. This is more readily distinguishable in the EDP model than in the ED model.

The region directly above the open hole that originally recorded negative PS states now record a positive PS state. This is because the PS shifts are not negative and the DIC strain has remained negative. The result is a positive PS state that may indicate this region as been unloaded due to growing crack fronts emitting from the open hole and no longer bear load.

Because the PS state is directly proportional to the mechanical properties of the particle-coating-substrate system as described in Chapter 3, the observation of a degrading PS state would be similar to a degrading elastic state. The ED model would indicate a rapidly degrading state, while the EDP model shows more resilient PS state due to the added trigger which initiates the elastic degradation. The composite substrate's material properties likely have not degraded as much as the ED model indicates. Rather, the rapid decline of the PS state in the ED model is likely from the highly inelastic mechanical behavior of particulate composites [94, 54]. Therefore the EDP model would be more practical to calculate the material properties and will be used in the next section.

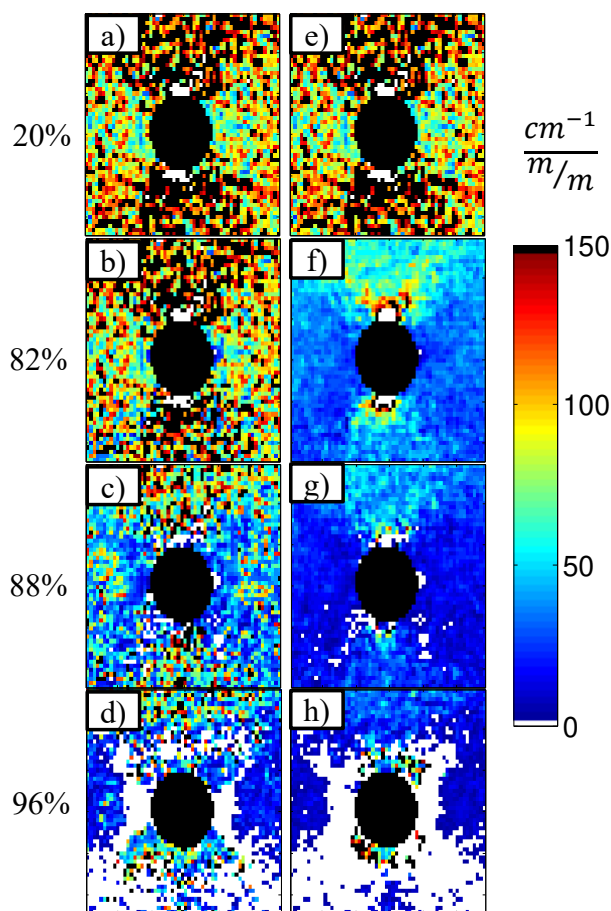


Figure 5.8: (a-d) Selected loads for the elastic degradation model and (e-h) the elastic degradation model with plastic deformation. Percent failure loads are indicated for each pair of maps and all maps share the same color scale.

### 5.3.2 Material Property Calculations

Now that the method of how to simulate the unloading of a PS state has been chosen, the goal is to convert these PS state maps into material property maps based on the mechanics discussed in Chapter 3. The relationship between the PS shift and biaxial strain is the PS state which was a function of several parameters including the material properties of the particle, coating, and substrate. From here, several assumptions are needed to obtain

a unique solution of the substrates elastic modulus. Figure 5.9 summarizes some of the assumptions for the material property calculations performed in this work.

The first and major assumption is that there is no coating and effectively the substrate itself is treated as a nanocomposite. This is a valid assumption because the coating itself has a very small modulus in comparison to the substrate, and is also much thinner, making it mechanically insignificant. This allows for a reduction in the number of variables. By doing so, the coating's material properties were replaced with the substrate material properties, similar to the procedure with the equivalent composite properties replacing the matrix properties in Chapter 2. The coating mechanics are then satisfied by converting the first invariant of the first strain invariant into a biaxial strain using a plane stress condition using Equation 3.17.

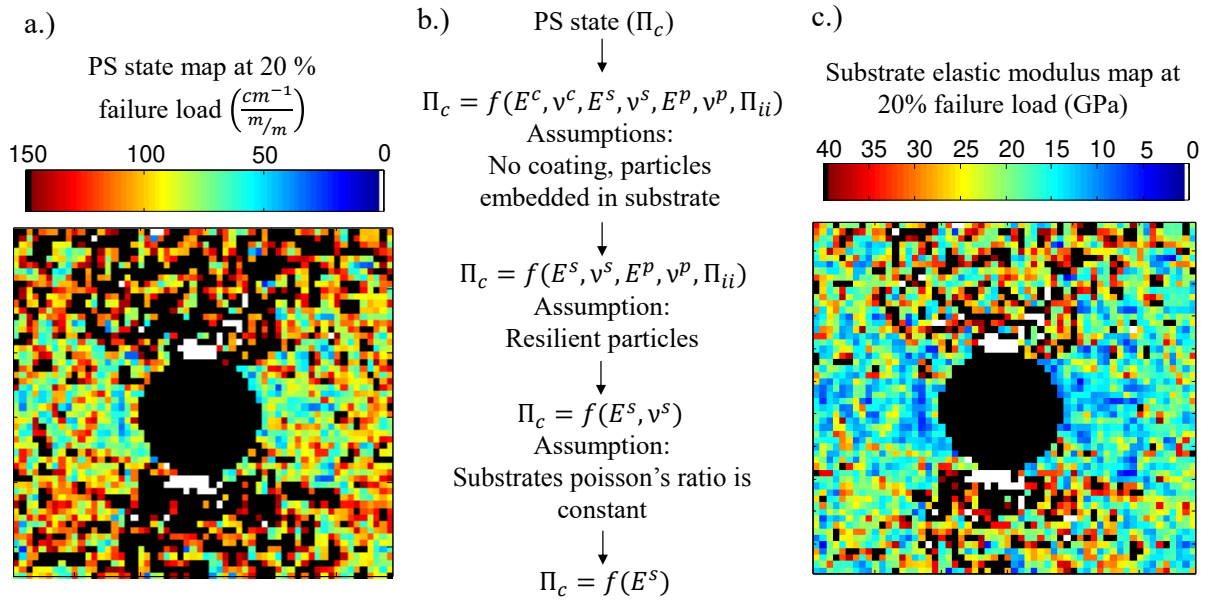


Figure 5.9: (a) The PS state map for 20% failure load. (b) The list of assumptions which allow for the creation of (c) an elastic modulus map of the substrate.

It was also assumed that the particles have resilient material properties and are not damaged throughout loading. This is a valid assumption because the  $\alpha$ -alumina particles are very rigid with an elastic modulus of 416 GPa and a Poisson ratio of 0.234 [75]. This further reduces the number of variables to only the substrate's isotropic properties. An additional assumption is made which is that the substrate's Poisson's ratio remains constant throughout loading with a value of 0.32 for this IM7-8552 unidirectional tape [11]. This is a reasonable assumption for low loads, but it has been observed that the Poisson's ratio of fiber composites change once matrix cracking and fiber-matrix interface debonding initiates [15]. This assumption can be improved since it has been reported in literature that scalar damage models can be inaccurate because of the change in Poisson's ratio [36].

Using the procedure and assumptions described here, an elastic modulus map was created and presented in Figure 5.9 for 20% failure load. The modulus maps for all the load increments are plotted in Figure 5.10. By inspection of the calculated moduli values for low loads in Figure 5.10, regions far away from the open hole agree with the modulus of the composite coupon without the presence of an open hole (38.6 GPa). Considering the open hole should reduce the modulus of the composite coupon, the material state values calculated for the first load point, at a distance away from the open hole, matched up well.

The relative degradation of the calculated modulus produces patterns that are similar to the observed damage in previous works in literature [11, 71]. The similar patterns are the initial onset of a failure region just adjacent to the open hole at 76% failure load, and the intrinsic X-pattern outward from the open hole at the higher failure loads. Despite

the many assumptions used in this study, the calculated modulus at low loads resembled the expected values, validating the procedure of estimating material state with PS as a success.

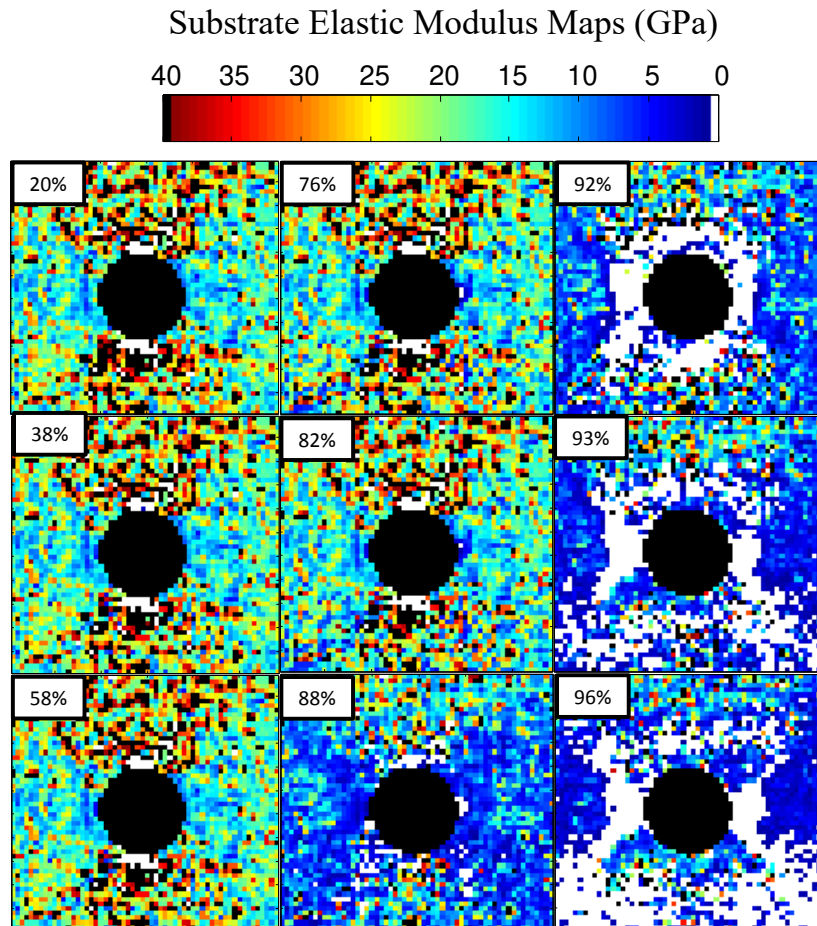


Figure 5.10: The substrate's elastic modulus maps for all the failure load increments.

#### 5.4 Modeling the PS response

Across the sample's surface the PS responses were all very different depending on their location with respect to the open hole. The many different types of responses are at-

tributed to the varying degrees of non proportional and non uniform loading across the surface. This section is devoted to attempting to model the wide array of different PS responses with a set of functions. First, a selected few PS responses were chosen for observation as shown in Figure 5.11(a-d). The PS responses was presented in two segments as the yield and the damage segment. The yield segment begins at zero load until the PS shift increases to a maximum. The damage segment initiates at the max PS shift and ends at the final load.

These two segments will be represented with yield and damage functions respectively. These functions will then be evaluated and improvements will be discussed. The functions enable a representation of the PS response, which then allows for a determination of the secant PS state. This is significant because most plasticity and continuum damage theories involve the secant modulus, which should be proportional to a secant PS state ???. Finally, a secant PS state map will be created and discussed.

#### **5.4.1 Yield and Damage Functions**

The behavior of particulate composites is very inelastic [94, 54], and the addition of nanoparticulates with significant volume fractions further increases the ductility and non-linearity [69]. The data collected for the PS responses here was very sparse in the low loads and therefore appears to initiate yielding immediately. Therefore, the Ramberg-Osgood yield function was used because it works well without a defined yield point [62], and is shown in Equation 5.1.

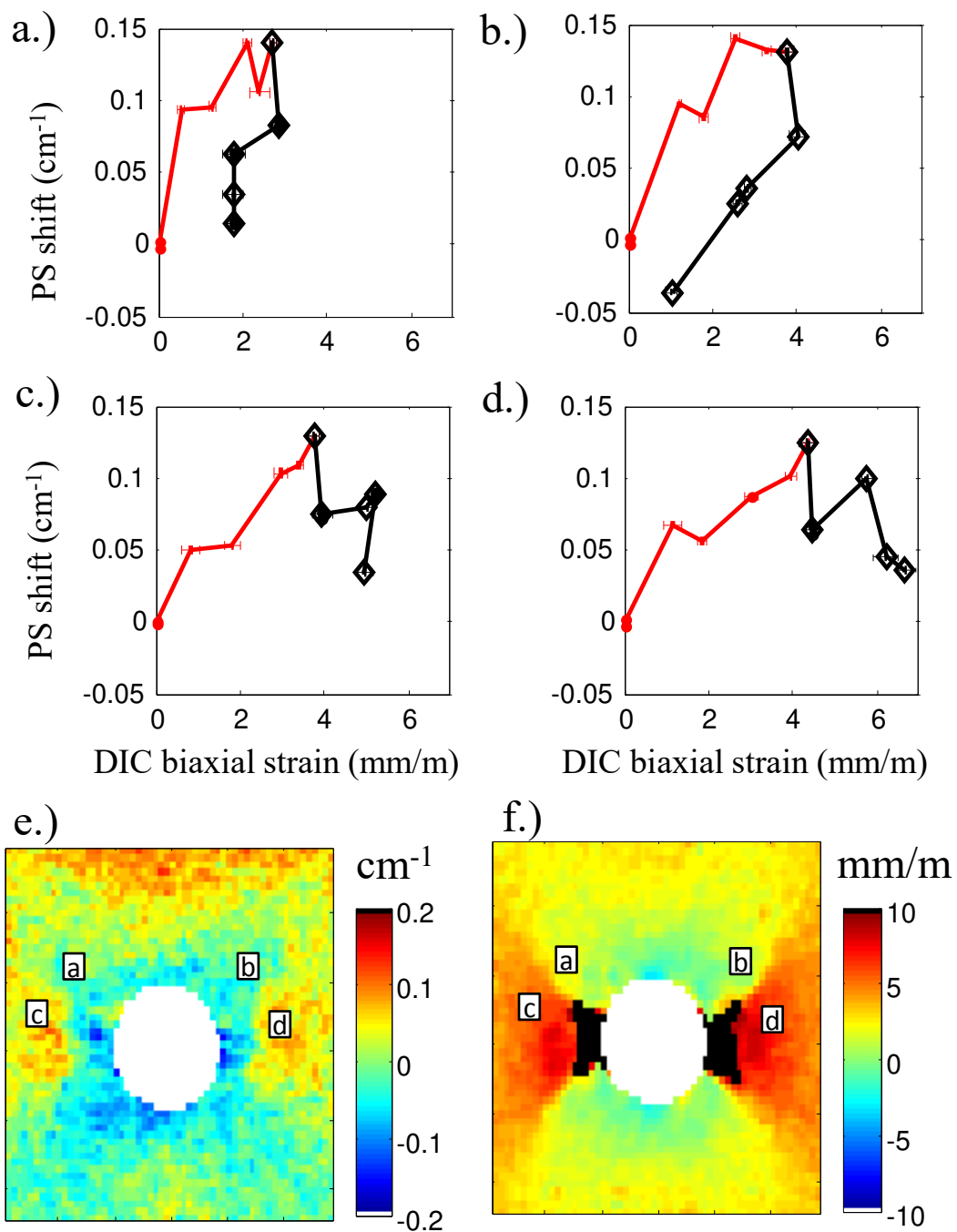


Figure 5.11: (a-d) are the PS responses for selected regions as indicated on the (e) PS shift map and (f) DIC biaxial strain map for 96% failure load.

$$\epsilon = \frac{\sigma}{E} + \alpha \frac{\sigma_y}{E} \left( \frac{\sigma}{\sigma_y} \right)^m \quad (5.1)$$

The formula in Equation 5.1, is normally used for a strain-stress plot, but was modified here for a strain-PS shift plot in Equation 5.2 because it was desired to plot DIC strain with PS shift. This reformulation of the Ramberg-Osgood formula is appropriate because the PS shift is directly proportional to stress or strain. In this instance when PS shift replaced stress, the elastic modulus ( $E$ ) was converted into a composite PS coefficient ( $\Pi_c$ ) which consists of the multipliers discussed in Chapter 3. This formula modeled the PS response from zero load until the maximum PS shift was reached.

$$\Delta\nu = \Pi_c \epsilon + \alpha \epsilon_y \Pi_c \left( \frac{\epsilon}{\epsilon_y} \right)^m \quad (5.2)$$

The remaining damage segment was fitted with a linear line connecting the maximum PS shift fitted by Equation 5.2, and the last data point of load history. This is a rough approximation which fails to take into account intermediate behavior in the damage segment, but the slope of this line reveals important information concerning the post maximum PS shift response which will be discussed in the next section. The current method of modeling the PS response in two segments was appropriate for the current analysis. The fits of these functions to the PS response is shown in Figure 5.12, and are the same PS responses which were shown in Figure 5.11.

Equation 5.2 was fitted to the PS response with a non-linear least squares algorithm. The variables used to fit Equation 5.2 to the PS response included the parameters  $\alpha$ ,  $m$ ,  $\epsilon_y$ , and  $\Pi_c$ . As this yield function was fit to every spatial point around the open hole,



this enabled the creation of maps which plotted the variables of the function. Displayed in Figure 5.13 are the variable maps and their respected histograms to observe their distribution.

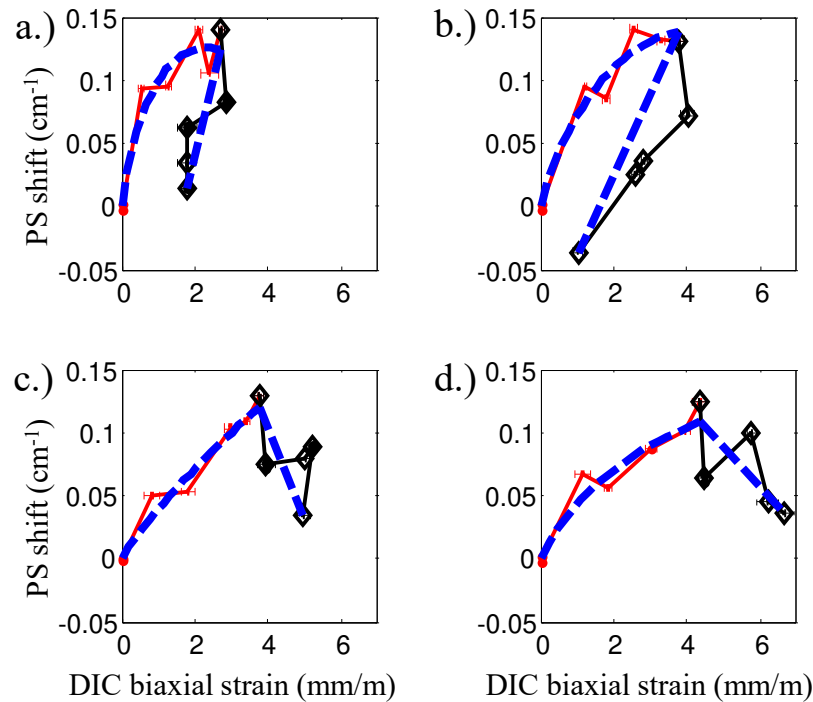


Figure 5.12: (a-d) are the PS responses for selected regions as indicated in Figure 5.11.

The variable with the clearest pattern with respect to the open hole is the yield strain in Figure 5.13b and this also exhibited a very normal distribution. The pattern coincides with regions which experienced large tensile strains to the left and right of the open hole. Additionally, regions above and below the hole had negative yield strain values, as they are actually under compression. This region also was distinguishable for the composite PS coefficient and for the exponential constant. It exhibited a small negative PS coefficient, with very slow decay.

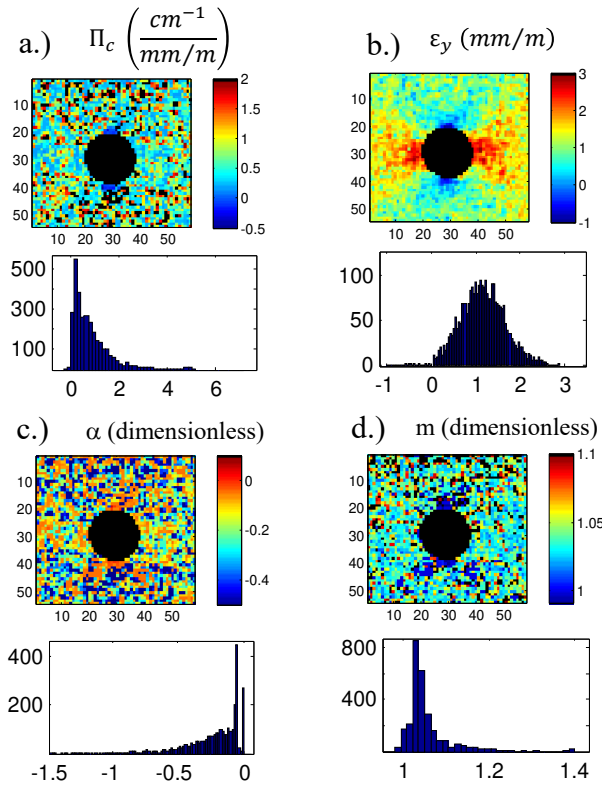


Figure 5.13: The variable maps and respected histograms for the (a) composite's PS coefficient, (b) yield strain, (c) linear dimensionless constant, and (d) the exponential dimensionless constant.

#### 5.4.2 The Secant PS State

With the PS response modeled, a focus will be directed towards the secant PS state. The secant state is usually a major contributing factor in determine the degradation and plastic deformation in many theories [94, 54, 12]. This section will focus on the damage segment of the PS response. That is mainly, the slope of the damage function fitted in the previous segment and observed in the post max PS shift in Figure 5.12.

PS secant state map  
of damage function

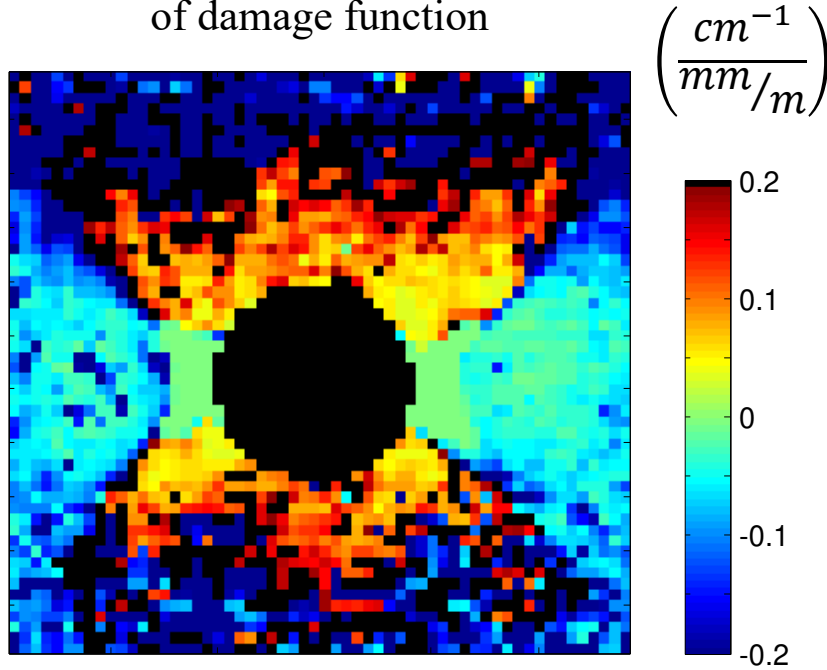


Figure 5.14: The secant PS state of the damage function. The damage function was a linear fit as discussed in the previous section, and can be represented with a single map.

Despite the simplicity of the damage function used here, significant patterns are observed in the secant map of the damage function in Figure 5.14. A distribution of negative and positive secant values are observed in symmetry about the open hole which indicate softening and hardening respectively [62]. It appears that positive secant values tend to be close to the open hole which would indicate a hardening during failure. Alternatively, the negative secant values away from the open hole would indicate softening during failure.

The positive and negative values can also be interpreted as unloading and continued loading respectively. Outward cracks from the open hole are known to develop in these composites samples [71]. The regions between the open hole and the crack are effectively

unloaded, and the regions outside of the crack are still load bearing. Because this secant map was created in the post max PS shift segment of the PS response, the regions indicating a positive secant modulus are effective reductions of stress carrying area of the sample [12] due to crack formation.

## 5.5 Conclusion

The PS and DIC measurements had excellent qualitative agreement. The observation of large PS shift gradients in regions known *a-priori* to exhibit significant cracking makes piezospectroscopy an attractive method for monitoring damage. Correlations with the general PS response and PS shift gradients across the surface were very similar to literature which describes the general mechanical response [44] and subsurface and surface damage [11, 71].

This work combined the spatial measurement of stress (piezospectroscopy) with a spatial measurement of strain (DIC) for the first time. This allows for damage mechanics to be applied to every spatial location independently enabling calculation of local material property and estimation of elastic degradation using the mechanics as described in Chapter 3. Despite the many assumptions, elastic modulus calculations were fairly accurate with respect to the undamaged composite properties. With simple yield and damage functions, the PS response was modeled, and the secant PS state revealed the size of the area which lost stress-carrying capacity due to crack propagation.

## CHAPTER 6 CONCLUSION

This work was part of an effort to expand the uses of piezospectroscopy to a wide variety of engineering applications. The development of this technology has required a re-visitation of fundamental PS, particle, and coating mechanics, which establish the relationships necessary to calculate material properties from the PS response. Then through the application of the derived mechanics, the ability to measure stress, damage, and material properties with PS nanocomposites and coatings were validated.

This work brought significant contributions to the emerging field of piezospectroscopic nanocomposites and coatings. Here, the fundamentals for interpreting the spectral R-line shifts in terms of embedded inclusion stresses were related to effective composite stresses. It was shown, that multi-scale mechanics that relate the PS shifts to composite stresses enabled the determination of mechanical properties of the composite. The comparisons of these calculated mechanical properties were very similar to the observed mechanical properties from the load cell data. With the material property relationships to the PS response established, damage mechanics were applied to observe the degradation of the elastic modulus. By comparison of the load cell and PS calculated moduli, for a simple elastic degradation model, it was observed that the degradation was much more pronounced with the PS data.

With the mechanics demonstrated on epoxy nanocomposites, the integration of coating mechanics to the multi-scale problem was applied to experimental data for plasma sprayed alumina coatings. Cyclic tensile experiments enabled the measurement of the degrading elastic modulus for both the load cell and PS data. Similar to the nanocomposite

data, the elastic modulus of the plasma spray sample was shown to degrade rapidly for the PS modulus when compared to the load cell measured modulus.

Because it is known that the mechanical behavior of these epoxy nanocomposites and alumina plasma spray coatings are very inelastic, the similarities in the quickly degrading PS measured modulus in comparison to the conventionally measured modulus with a load cell, suggest that the PS measurements are very sensitive to micro-structural changes in the material. Additionally, it is proposed that the PS measured modulus is a more accurate representation of micro-mechanical behavior. Piezospectroscopy, because of its accessibility and ability to probe micro-scale stresses, would be superior to any other conventional method to characterize micro-mechanical behavior of materials containing  $\alpha$  alumina or other materials with PS properties.

For an epoxy nanocomposite coating, very profound results were reported for a novel experiment which combined the spatial capabilities of piezospectroscopy with a spatial calibration of digital image correlation. This experiment was performed on a open hole tension composite coupon, with a load history which focused on the failure regime in detail. The results showed excellent qualitative agreement between the DIC and PS measurements. Additionally, the PS shift maps showed strong PS shift gradients in areas known *a-priori* to have intense damage. The observed PS shift gradients agreed well with literature that investigated the failure mechanisms numerically and experimentally for such composites with an open hole. This includes the observation of initial fiber failure, redistribution of stress due to subsurface damage, and large cracks propagating outward from the open hole.

With spatial measurements of DIC and piezospectroscopy, local PS responses were independently analyzed to obtain local material property values. With a damage model applied which combined elastic degradation with some plastic deformation, the degrading material properties were observed across the samples surface. Additionally, a secant PS state map was calculated for the damage segment of local PS responses to indicate two distinct regions across the open hole sample. One region close to the open hole, exhibited a relaxation behavior due to the loss of load carrying capacity. The remaining regions experienced a softening due to the increased damage associated with the load bearing portion of the sample.

This work has demonstrated that piezospectroscopy is not only an excellent tool to measure stress, but also to calculate material properties. Through the development of some simple mechanics, and the application thereof to experimental mechanical tests, piezospectroscopy has shown promise to being adapted to a wide array of engineering applications. It has been shown to be an excellent measure of micro-mechanics for the epoxy nanocomposites and plasma sprayed alumina coatings. An even greater feat, is that piezospectroscopy has been shown to be an excellent sensor for subsurface damage propagation in a carbon fiber composites. Many intrinsic patterns of damage for these composites were observed as PS shift gradients across the surface of the sample.

It has been shown that many future engineering applications are possible with piezospectroscopy for both laboratory and in-service settings. There is great promise for this technique to be used in laboratories for characterizing and developing enhanced micro-mechanics for alumina composites and has also exhibited great potential for in-service non-destructive evaluation (NDE) of structures by the application of a PS nanocomposite

coating. Certainly, the laboratory applications will need to be developed before piezospectroscopy is utilized as a future in-service NDE technique. Future areas of development include high quality PS coatings containing evenly dispersed  $\alpha\text{-Al}_2\text{O}_3$  nanoparticles, integration of a full field PL imaging system with a high powered excitation source while maintaining field mobility, and continued calibration testing for various coating-substrate systems. The extension of this technology will require multi-disciplinary inputs ranging from nanocomposite manufacturing, novel experimental methods, and the application of multi-scale damage mechanics. This work has been successful in combining multi-scale mechanics with experimental observations of PS nanocomposite coatings to indicate the possibility to detect subsurface damage with such coatings. The implications are wide reaching for many engineering disciplines for both in-service damage inspection and laboratory characterization of damage mechanisms in advanced nanocomposites.



**APPENDIX A**  
**CURVE FITTING**

## APPENDIX A CURVE FITTING

This chapter is devoted to the unique data analysis required to conduct this research. As Piezospectroscopy becomes more and more developed the volume of data becomes larger and the robustness of data analysis must be improved to handle the different array of data sets as well as the speed to reduce computational time. Previously, curve fitting was done with a genetic algorithm (GA) which proved to be very reliable for a wide array of data sets. However, the GA was very slow, requiring roughly two minutes for the analysis of a single spectra on a personal computer. With the advancement of measurement techniques, PS maps typically have on the order of one thousand spectra. Additionally, mechanical tests usually compare multiple PS maps on the order of 10, which would put the estimated time for data processing of all the spectra for all loads at just under 14 days. There became a need to improve the speed of analysis. This was done with a built in non linear least squares function in matlab which reduced the analysis time of a single spectra to roughly 100ms. An improvement of nearly 3 orders of magnitude.

First, the curve fitting of two pseudo-Voigt functions for experimental R1 and R2 will be reviewed. This involves the creation of a subfunction that handles the baseline removal in addition to the several initial guesses needed for this function. The pseudo-Voigt function will be defined and described. Then the architecture of the curve fitting algorithm will be discussed. Then briefly, the subfunctions will be defined as they are, and the potential for methods of improving the algorithm will be discussed.

### A.1 The pseudo-Voigt function

The pseudo-Voigt function originated from the Voigt profile [45, 96] which was introduced by Wertheim et al. [99]. The Voigt function is a summation of Gaussian ( $G$ ) and Lorentzian ( $L$ ) line-shapes. The pseudo-Voigt assumes equal line-widths of both Gaussian and Lorentzian contributions. The weights of these two functions are determined by the Gauss Ratio [96]. This is a standard function used among spectral curve fitting analysis and is mathematically shown in Equation A.1.

$$\Phi(\nu) = 2A [\Phi_G(\nu) + \Phi_L(\nu)] \quad (\text{A.1})$$

Here,  $\Phi_G$  and  $\Phi_L$  represent the  $G$  and  $L$  functions. They both produce the spectral intensities  $\Phi$  as a function of the wavenumber  $\nu$ .  $A$  represents the integrated intensity under the spectral function. The  $G$  and  $L$  function are shown in Equation A.2 and A.3.

$$\Phi_G(\nu) = \frac{GR}{W} \sqrt{\frac{\ln 2}{\pi}} \exp\left(-4 \ln 2 \left(\frac{\nu - C}{W}\right)^2\right) \quad (\text{A.2})$$

$$\Phi_L(\nu) = \frac{LR}{\pi W [1 + 4(\frac{\nu - C}{W})^2]} \quad (\text{A.3})$$

The pseudo-Voigt function has a total of 4 independent variables which can produce intensities  $\Phi$  from spectral wavenumbers  $\nu$ . These 4 variables are shared between both the Gaussian and Lorentzian components. They are as follows:  $\nu$  is the emission wavenumber,  $C$  is the peak position of the spectral line,  $W$  is the FWHM of the spectral line,  $A$  is the Area under the spectral line, and  $GR$  is the Gauss ratio. The Gauss ratio varies from

zero to one, where zero is purely  $L$ , and one is purely Gaussian. The Gauss Ratio is also can be represented by the Lorenz Ratio where  $GR = 1 - LR$ .

The pseudo-Voigt function has now been defined, but the R-line doublet consists of two convoluted pseudo-Voigt functions. The doublet function  $\Phi_{doublet}$  consist of two overlapping pseudo-Voigts of  $R1$  and  $R2$  shown in Equation A.4. This equation is the function used to fit the experimental R-line doublet and consists of 8 variables, where the  $R1$  and  $R2$  each have a unique set of the variables discussed previously.

$$\Phi_{doublet}(\nu) = \Phi_{R1}(\nu) + \Phi_{R2}(\nu) \quad (\text{A.4})$$

## A.2 Curve fitting Algorithm Architecture

The goal of the curve fitting algorithm is to input the experimental data for the R-line doublet, and output the pseudo-Voigt characteristics. In later chapters, these pseudo-Voigt characteristics, mainly peak position, will be used to determine the state of stress. It is very important to define the method by which we determine these peak positions, because the accuracy of our stress measurements depend on it. In Figure A.1, the block diagram for the curve fitting procedure is shown, and subfunctions are enhanced. A description of each subfunction will be given and its placement in sequence of block diagrams will be discussed.

The subfunction indexing is used to locate the major features of the R-line doublet, by locating the major features of the R-line doublet, accurate initial guesses can be

obtained, in addition to approximate upper and lower bounds for the experimental data to be fitted. To illustrate the critical points to find in the R-line doublet, Figure A.2 represents the output indexing, which are the locations of the critical points. Indexing requires the experimental data to be smoothed because the derivatives are taken to find some critical locations. However, the pseudo-Voigt functions will still be fit to the raw experimental data in a later step.

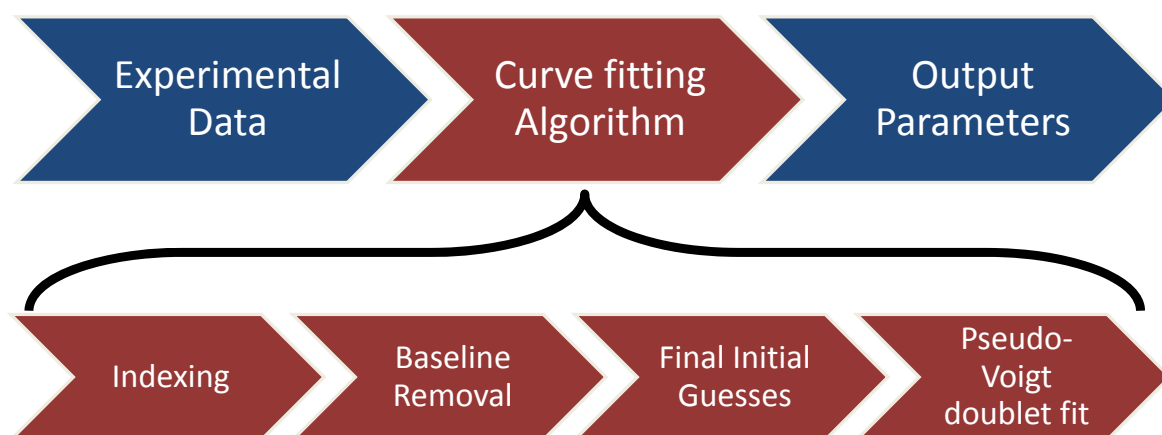


Figure A.1: A block diagram for the current curve fitting procedure, the curve fitting algorithm is decomposed into the 4 main subsections.

This function starts by identifying the maximum intensity of the spectra which would be the R1 index. From here, the region of the R-line doublet that is primary interest is the wavenumbers that are greater than R1. This is defined as the "upperwave". The current method only relies on the upperwave to determine the critical locations. It should be noted that the indexing for the upperwave is different from the indexing of the lower wave by the subtraction of the R1 index on the raw waveform.

Once the upperwave has been sectioned, the next step is finding the trough index. The trough is found by taking the derivative of the upper wave and finding the first zero

crossing. The trough index is a critical point because it supplies an approximation for a wavenumber value which will serve as a new lower index of the upperwave. This new lower bound serves to enable the use of the find maximum intensity function to the R2 index.

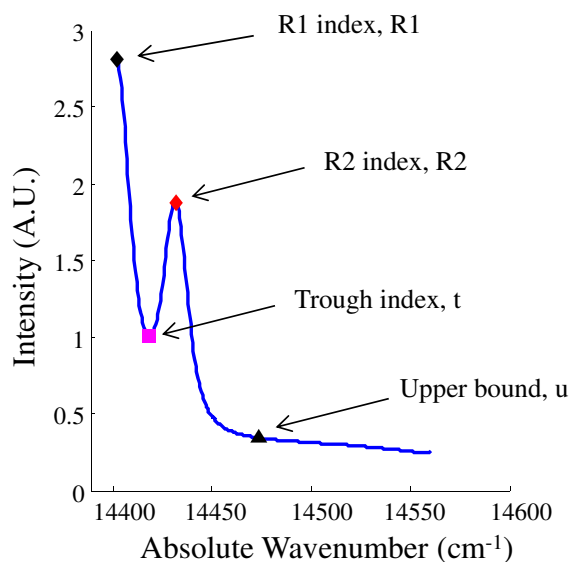


Figure A.2: The "upperwave" of the R-line doublet which contains the critical points to define in order to initialize the fitting process.

Now that the trough index ( $t$ ), the R1 index ( $R1$ ), and the R2 index ( $R2$ ) have been found these indexes will now be used to define the upper and lower bounds for the baseline removal in addition to the sectioning for the pseudo-Voigt fitting. These indexes are defined with respect to the array of raw data. The upper ( $u$ ) and lower bounds ( $l$ ) were defined in the current algorithm to be Equations A.5 and A.6.

$$u = R2 + 4.5(R2 - t) \tag{A.5}$$

$$l = R1 - 4.5(t - R1) \tag{A.6}$$

The constant of 4.5 was chosen based on observation of fits to the experimental data. The current method of determining the upper and lower bounds is a function of the separation of the two R-lines. There may be a procedure to optimize the upper and lower indexes based on some iterative process. Originally, the derivative was used to determine the upper and lower bounds by searching for the location where the derivative crossed zero. However, this was not a robust method for the large volume of different data sets studied here. Typically the derivative did not reach zero, likely due to either broad R-lines with significant  $L$  tails or neighboring low intensity peaks such as the vibronic bands.

The baseline subfunction requires the inputs of the upper and lower bounds from the indexing function. The baseline is a linear that reduces the two endpoints to zero intensity and was shown in Figure A.3. Additionally, the baseline removal also handles smoothed experimental data to determine the baseline removal intensity, but is applied to the raw experimental data. This allows for robust method for data with relatively large background noise.

The baseline needed to be removed quickly to finalize the initial guesses. The full width half max, and integrated intensity are better computed with the baseline removed. The initial guesses for the peak position of R1 and R2 were already found in the indexing subfunction. The initial guess for the GR can be universally applied to all spectra as .5, both for R1 and R2.

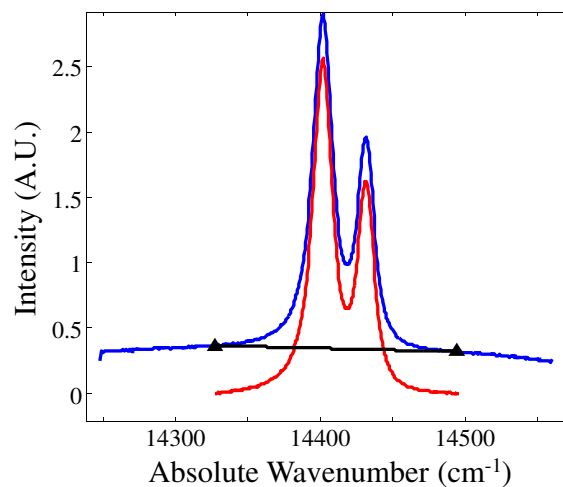


Figure A.3: The baseline removal process shown which utilized the determination of the lower and upper bounds in indexing.

All initial guesses contain an upper and lower bound which were all found by trial and error by inspection of the accuracy of the initial guesses and range from typical bounds are  $+ / - 50\%$ . Improvements in the accuracy of the initial guess were not observed to have an effect on the final solution. This was verified by inserting the final solution as new initial guesses. The result was the same answer found previously with the original initial guesses.

Future work for improving the performance of the algorithm is to investigate the effects of the determination of the upper and lower endpoints of baseline removal and data sectioning. This has been observed to greatly effect error in the fit. Future determination of the endpoints may involve an initial baseline removal, followed by refinement of endpoints with additional variables of the FWHM initial guess. This would take into account broadening of the peaks, where currently, only the peak separation is taken into account.



**APPENDIX B**  
**IMAGE PROCESSING**

## **APPENDIX B IMAGE PROCESSING**

The image processing and alignment of PS and DIC data will be addressed. This involves a subfunction which defines a local signal to noise ratio (SNR) which determines whether the data has sufficient signal to perform a curve fit. Following this, additional techniques are required to spatially correlate the PS maps between load which account for the displacement of a reference point. The open hole is a convenient reference point that is shared by the DIC and PS data. The technique defining the local coordinate system for each load, and transforming it into a global coordinate system for the mechanical test will be discussed. Additionally, this reference point was also used for the secondary strain mapping of DIC. Future work will be discussed in refining and improving the data analysis techniques.

### **B.1 Signal to Noise Ratio**

When imaging an open hole tension sample with PS, points imaged inside the hole will give weak or no PL intensity. Because some points graze the edge of the hole during the snake scan, there can be a variation of intensity leading up to the open hole. This lower signal increases uncertainty in peak position determination and is omitted from the analysis.

In order to quantify this loss of intensity to qualify the data as being part of the hole, a sub function was created to compare the intensity of the R line to the background noise. This signal to noise ratio (SNR) subfunction was demonstrated in Figure B.1a-c for areas

very close to the hole. These three points show the extremes which the algorithm searches for and qualifies as being suitable for curve fitting. It was observed that a steady state in SNR is reached once the laser dot is on the sample. Some spectra which are on the edge of the hole, the laser dot may only contain a fraction of the sample, producing a low signal. The steady state was determined to be  $\text{SNR}=65$ , in which only Figure B.1a would qualify for curve fitting and considered to be on the sample.

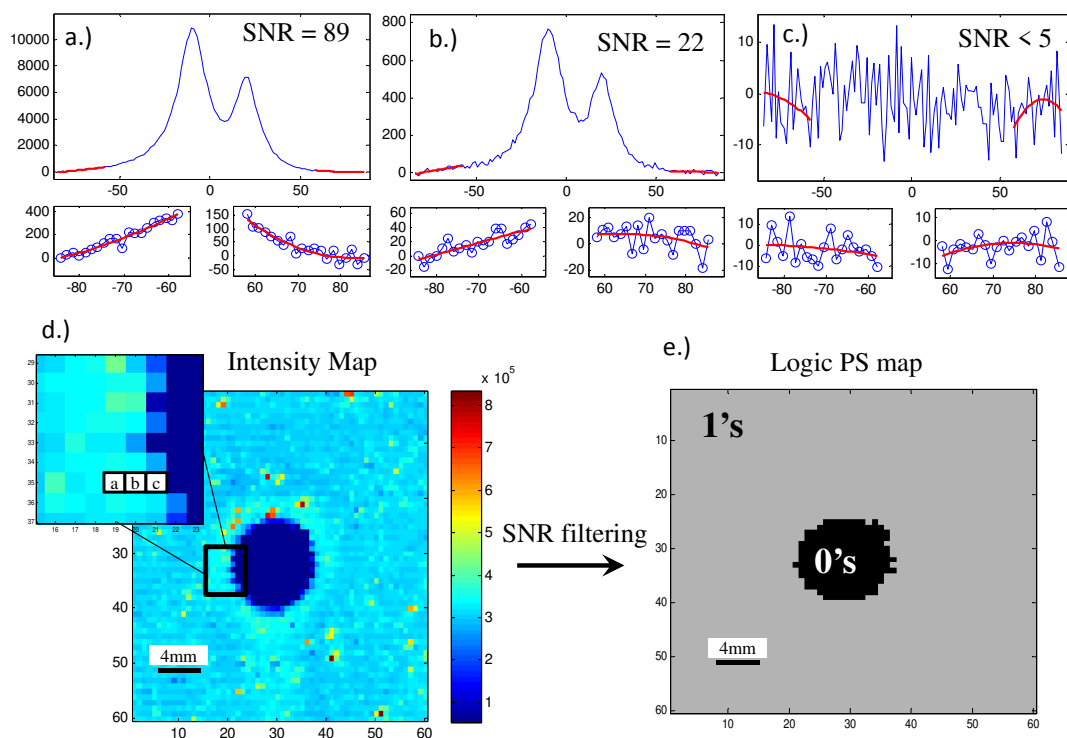


Figure B.1: (a-c) The signal to noise ratio outputs for 3 locations next to the open hole. (d) An intensity map of the sample with an inset showing the three locations of interest. (e) A logic map created by spectra which passed the SNR threshold.

With the SNR ratio defined for every measured point, now a PS logic map was created to easily identify the hole. Logic map contains a value of one for spectra with adequate SNR values  $\geq 65$ , and zeros for  $\text{SNR} \leq 65$ . The threshold for the SNR subfunction was

user defined by inspection of quality of data and reliability of PS shift measurements. Optimizing the signal, and verifying the the uncertainty of PS shift with a given signal is an area of future work.

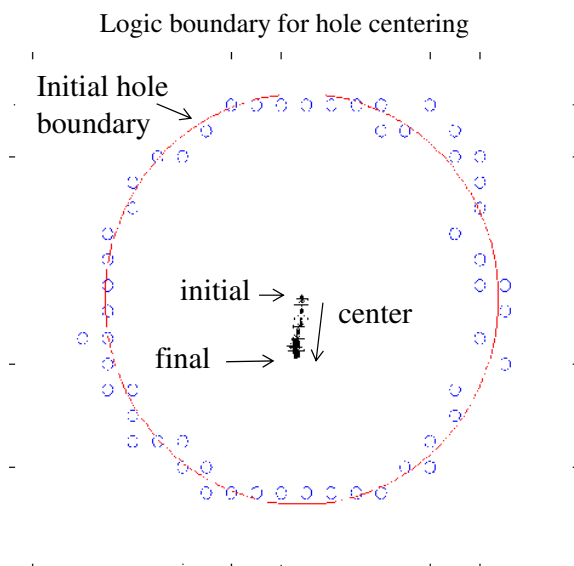


Figure B.2: (a) A schematic demonstrating the movement of the hole with respect to the detector's field of view. (b) A logic map converted into an array of boundary points which define the hole. The points are then used to fit a circle and track the movement of the hole.

## B.2 Open Hole Tension PS-DIC map Alignment

By having the hole defined with the logic map is displayed in Figure B.1, the process of aligning the holes begins. The alignment process is necessary because PS is a spatially dependent measurement, and displacement of the sample was significant during loading. The equipment which captured the spectra were in a fixed field of view, so as the sample

was loaded and displaced, the hole drifted as shown in the schematic in Figure B.2a. Using the Logic map, a series of boundary values can be defined as the hole itself. Fitting a circle to these boundary values give a center of the hole which will act as the local reference to the coordinate system to this load. By monitoring the center of the circles with increasing load, the drift of the hole was quantified and displayed in Figure B.2b.

Now, the PS maps were interpolated to all be in the sample reference frame, which accounted for the movement of the hole. It is noted that the hole not only drifts, but also grows in size and changes shape under increasing load as observed in Figure B.3. Due to the inaccuracy of the region closest to the open hole, this region was filtered out of the final plot. The map before and after the hole removal was shown in Figure B.3.

This same process for identifying the center of the hole, and interpolating to a new global reference frame was repeated for the digital image correlation data. Both sets of PS and DIC data are now centered to the hole, and a point by point correlation can be made.

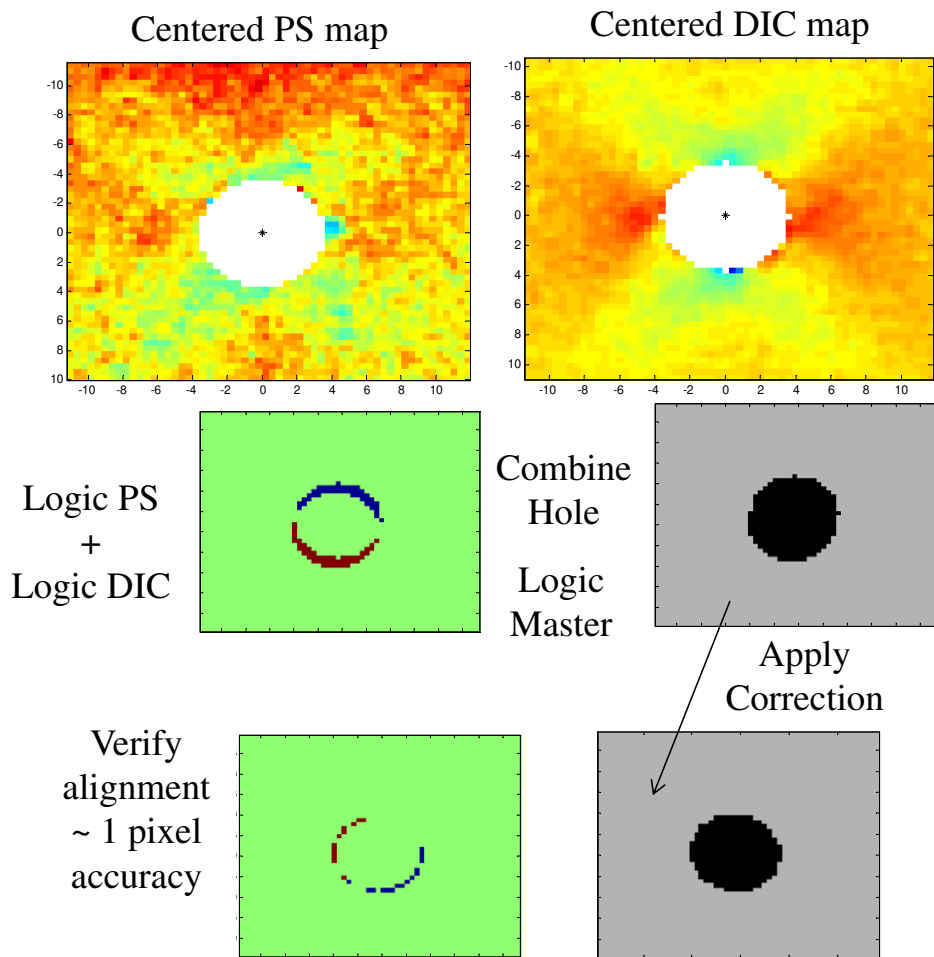


Figure B.3: (a) An illustration demonstrating the change in size and shape of the hole under increasing loads. (b) A PS map before and after the regions close to the open hole were removed.

## LIST OF REFERENCES

- [1] A. J. Allen, J. Ilavsky, G. G. Long, J. S. Wallace, C. C. Berndt, and H. Herman. Microstructural characterization of yttrium-stabilized zirconia plasma-sprayed deposits using multiple small-angle neutron scattering. *Acta Materialia*, 49:1661–1675, 2001.
- [2] M. Alves, J. Yu, and N. Jones. On the elastic modulus degradation in continuum damage mechanics. *Computers & Structures*, 76(6):703–712, 2000.
- [3] ASTM. Standard test method for compressive properties of rigid plastics D-695 (02a). Technical report, American Society for Testing and Materials, 2002.
- [4] ASTM. Standard test methods for tension testing of metallic materials, 2008.
- [5] ASTM. *D5766/D5766M-11 Standard Test Method for Open-Hole Tensile Strength of Polymer Matrix Composite Laminates*. ASTM International, West Conshohocken, PA, 2011.
- [6] A. Ayyar and N. Chawla. Microstructure – based modeling of crack growth in particle reinforced composites. *Composites Science and Technology*, 66(13):1980–1994, 2006.
- [7] K. Balani, S. P. Harimkar, A. Keshri, Y. Chen, N. B. Dahotre, and A. Agarwal. Multiscale wear of plasma-sprayed carbon-nanotube-reinforced aluminum oxide nanocomposite coating. *Acta Materialia*, 56(20):5984–5994, 2008.
- [8] E. E. Balic, M. Hadad, P. P. Bandyopadhyay, and J. Michler. Fundamentals of adhesion of thermal spray coatings: Adhesion of single splats. *Acta Materialia*, 57:5921–5926, 2009.
- [9] L. Benabou, M. Naïf Abdelaziz, and N. Benseddiq. Effective properties of a composite with imperfectly bonded interface. *Theoretical and Applied Fracture Mechanics*, 41(1):15–20, 2004.
- [10] D. L. Burriss and W. G. Sawyer. Improved wear resistance in alumina-PTFE nanocomposites with irregular shaped nanoparticles. *Wear*, 260(7):915–918, 2006.
- [11] P. P. Camanho, P. Maimí, and C. Dávila. Prediction of size effects in notched laminates using continuum damage mechanics. *Composites Science and Technology*, 67(13):2715–2727, 2007.
- [12] I. Carol, E. Rizzi, and K. William. A unified theory of elastic degradation and damage based on a loading surface. *International Journal of Solids and Structures*, 31:2835–2865, 1994.
- [13] N. Chawla, V. Ganesh, and B. Wunsch. Three-dimensional (3d) microstructure visualization and finite element modeling of the mechanical behavior of SiC particle reinforced aluminum composites. *Scripta Materialia*, 51(2):161–165, 2004.

- [14] J. Cho, M. Joshi, and C. Sun. Effect of inclusion size on mechanical properties of polymeric composites with micro and nano particles. *Composites Science and Technology*, 66:1941–1952, 2006.
- [15] T. Clyne and P. Withers. *An Introduction to Metal Matrix Composites*. Press Syndicate of the University of Cambridge, 1993.
- [16] D. Crawmer. Plasma spray coatings. In *Encyclopedia of Materials: Science and Technology (Second Edition)*, pages 7035 – 7040. Elsevier, Oxford, 2nd edition, 2001.
- [17] R. Cuffe, G. Baud, M. Benmalek, J. Besse, J. Butruille, H. Dunlop, and M. Jacquet. Characterization and adhesion study of thin alumina coatings sputtered on pet. *Thin Solid Films*, 270(1):230–236, 1995.
- [18] G. de Portu, L. Micele, Y. Sekiguchi, and G. Pezzotti. Measurement of residual stress distributions in  $Al_2O_3Y - TZP$  multilayered composites by fluorescence and raman microprobe piezo-spectroscopy. *Acta Materialia*, 53:1511–1520, 2005.
- [19] F. Deng and K. Vliet. Prediction of elastic properties for polymer-particle nanocomposites exhibiting an interphase. *Nanotechnology*, 22:165703, 2011.
- [20] J. Douce, J.-P. Boilot, J. Biteau, L. Scodellaro, and A. Jimenez. Effect of filler size and surface condition of nano-sized silica particles in polysiloxane coatings. *Thin Solid Films*, 466(1):114–122, 2004.
- [21] H. Duan, X. Yi, Z. Huang, and J. Wang. A unified scheme for prediction of effective moduli of multiphase composites with interface effects. part I: Theoretical framework. *Mechanics of Materials*, 39:81–93, 2007.
- [22] G. Dwivedi, T. Nakamura, and S. Sampath. Controlled introduction of anelasticity in plasma-sprayed ceramics. *J. Am. Ceram. Soc.*, 94:S104–S111, 2011.
- [23] J. H. Eggert, K. A. Goettel, and I. F. Silvera. Ruby at high pressure. I. optical line shifts to 156 GPa. *Physical Review B*, 40:5742, 1989.
- [24] E. Ergin. Development of nanoparticle piezospectroscopy for in-situ health monitoring. Master’s thesis, Chalmers University of Technology, 2012.
- [25] J. C. S. Eric N. Gilbert, Brian S. Hayes. Nano-alumina modified epoxy based film adhesives. *Polymer Engineering and Science*, 43 No. 5:1096–1104, May 2003.
- [26] R. Eshelby. The determination of the elastic field of an ellipsoidal inclusion, and related problems. *Proceedings of the Royal Society of London*, A241:376–396, 1957.
- [27] G. Freihofer, A. Bullock, F. Vaughn, H. Tat, J. Dustin, A. Schlzgen, and S. Raghavan. Stress and damage sensing of composite coupons with piezospectroscopic coatings. In *Proceeding of the Society for the Advancement of Material and Process Engineering 2014 conference, Seattle, WA*, 2014.



- [28] G. Freihofer, D. Fugon, A. Jones, E. Ergin, A. Schülzgen, H. Tat, and S. Raghavan. Prediction of piezospectroscopic properties with nanoparticle load transfer theories. In *Proceeding of the Society for the Advancement of Material and Process Engineering 2013 Conference, 6-9 May 2012, Long Beach, CA.*, 2013.
- [29] G. Freihofer, D. Fugon-Dessources, E. Ergin, A. V. Newkirk, A. Gupta, S. Seal, A. Schülzgen, and S. Raghavan. Piezospectroscopic measurements capturing the evolution of plasma spray-coating stresses with substrate loads. *Applied Materials and Interfaces*, 6(3):1366–1369, 2014.
- [30] G. Freihofer, A. Gupta, A. V. Newkirk, S. Seal, and S. Raghavan. Optical stress sensing alumina nanocomposite coatings for aerospace structures. In *AIAA SciTech, 55th AIAA/ASME/ASCE/AHS/SC Structures, Structural Dynamics, and Materials Conference*, 2014.
- [31] G. Freihofer, L. Poliah, K. Walker, A. Medina, and S. Raghavan. Optical stress probe: in situ stress mapping with raman and photo-stimulated luminescence spectroscopy. *Journal of Instrumentation*, 5:P12003, 2010.
- [32] G. J. Freihofer, S. Frank, E. Ergin, A. S. Jones, A. Stevenson, A. Schülzgen, S. Raghavan, and H. Tat. Measurement of load transfer within alumina nanoparticle epoxy composites using piezospectroscopy. In *Proceeding of the Society for the Advancement of Material and Process Engineering 2012 Conference, 21-24 May 2012, Baltimore, MD.*, 2012.
- [33] L. Freund and S. Suresh. *Thin Film Materials: Stress, Defect Formation, and Surface Evolution*. Cambridge University Press, 2003.
- [34] S.-Y. Fu, X.-Q. Feng, B. Lauke, and Y.-W. Mai. Effects of particle size, particle/matrix interface adhesion and particle loading on mechanical properties of particulate – polymer composites. *Composites Part B: Engineering*, 39(6):933–961, 2008.
- [35] L. Grabner. Spectroscopic technique for the measurement of residual stress in sintered  $Al_2O_3$ . *Journal of Applied Physics*, 49(5):580–583, 1978.
- [36] N. Hansen and H. Schreyer. A thermodynamically consistent framework for theories of elastoplasticity coupled with damage. *International Journal of Solids and Structures*, 31:359–389, 1994.
- [37] V. Harok and K. Neufuss. Elastic and inelastic effects in compression in plasma-sprayed ceramic coatings. *Journal of Thermal Spray Technology*, 10:126–132, 2001.
- [38] H. Hawthorne, L. Erickson, D. Ross, H. Tai, and T. Troczynski. The microstructural dependence of wear and indentation behavior of some plasma-sprayed alumina coatings. *Wear*, 203–204:709–714, 1997.
- [39] He and Clarke. Polarization dependence of the  $Cr^{3+}$  R line fluorescence from sapphire and its application to crystal orientation and piezospectroscopic measurement. *Journal of the American Ceramic Society*, 80(1):69–78, June 1997.

- [40] J. He, I. J. Beyerlein, and D. R. Clarke. Load transfer from broken fibers in continuous fiber  $Al_2O_3$ -Al composites and dependence on local volume fraction. *Journal of the Mechanics and Physics of Solids*, 47:465–502, 1999.
- [41] J. He and D. R. Clarke. Determination of the piezospectroscopic coefficients for chromium doped sapphire. *Journal of American Ceramic Society*, 78(5):1347–1353, 1995.
- [42] J. H. Heida and D. J. Platenkamp. In-service inspection guidelines for composite aerospace structures. In *18th World Conference on Nondestructive Testing*, pages 16–20, April 2012.
- [43] T. Hübert, S. Svoboda, and B. Oertel. Wear resistant alumina coatings produced by a sol-gel process. *Surface and Coatings Technology*, 201(1):487–491, 2006.
- [44] D. R. Hufner and M. L. Accorsi. A progressive failure theory for woven polymer-based composites subjected to dynamic loading. *Composite Structures*, 89:177–185, 2009.
- [45] T. Ida, M. Ando, and H. Toraya. Extended pseudo voigt function for approximating the Voigt profile. *Journal of Applied Crystallography*, 33:1311–1316, July 2000.
- [46] D. C. J.A. Nychka. Damage quantification in TBCs by photo-stimulated luminescence spectroscopy. *Surface Coatings and Technology*, 146-147:110–116, 2001.
- [47] A. Jayaraman. Ultrahigh pressures. *Rev. Sci. Instrum.*, 57:1013–1031, 1986.
- [48] Q. L. Ji, M. Q. Zhang, M. Z. Rong, B. Wetzel, and K. Friedrich. Tribological properties of surface modified nano-alumina/epoxy composites. *Journal of Materials Science*, 39(21):6487–6493, 2004.
- [49] A. S. Jones, G. Freihofer, E. Ergin, K. Lautenslager, W. Gysi, A. Schülzgen, S. Raghavan, and H. Tat. Embedded alumina nanoparticles as diagnostic coatings for structures. In *Proceeding of the Society for the Advancement of Material and Process Engineering 2012 Conference, 21-24 May 2012, Baltimore, MD.*, 2012.
- [50] M. Kathrein, W. Schintlmeister, W. Wallgram, and U. Schleinkofer. Doped CVD  $Al_2O_3$  coatings for high performance cutting tools. *Surface and Coatings Technology*, 163:181–188, 2003.
- [51] O. Kesler, J. Matejicek, S. Sampath, S. Suresh, T. Gnaeupel-Herold, P. C. Brand, and H. J. Prask. Measurement of residual stress in plasma-sprayed metallic, ceramic and composite coatings. *Materials Science and Engineering A*, A257:215–224, 1998.
- [52] A. Khanna and D. G. Bhat. Nanocrystalline gamma alumina coatings by inverted cylindrical magnetron sputtering. *Surface and Coatings Technology*, 201(1):168–173, 2006.

- [53] J. Kim and J. Lee. A new model to predict effective elastic constants of composites with spherical fillers. *Journal of Mechanical Science and Technology*, 20:1891–1897, 2006.
- [54] E. Kontou. Micromechanics model for particulate composites. *Mechanics of materials*, 39(7):702–709, 2007.
- [55] O. Kovářík, J. Siegl, J. Nohava, and P. Chráska. Young’s modulus and fatigue behavior of plasma-sprayed alumina coatings. *Journal of Thermal Spray Technology*, 14:231, 2005.
- [56] F. Kroupa. Nonlinear behavior in compression and tension of thermally sprayed ceramic coatings. *Journal of Thermal Spray Technology*, 16:84, 2007.
- [57] T. Lewis and L. Nielsen. Dynamic mechanical properties of particulate-filled composites. *Journal of Applied Polymer Science*, 14(6):1449–1471, 1970.
- [58] C.-J. Li and A. Ohmori. Relationships between the microstructure and properties of thermally sprayed deposits. *Journal of Thermal Spray Technology*, 11:365–374, 2002.
- [59] S. Lim, K. Zeng, and C. He. Morphology, tensile and fracture characteristics of epoxy-alumina nanocomposites. *Materials Science and Engineering: A*, 527(21):5670–5676, 2010.
- [60] D. Lipkin and D. Clarke. Measurement of the stress in oxide scales formed by oxidation of alumina-forming alloys. *Oxidation of Metals*, 45:267, 1996.
- [61] Y. Liu and T. Nakamura. Anelastic behavior of plasma-sprayed zirconia coatings. *J. Am. Ceram. Soc.*, 91:4036–4043, 2008.
- [62] J. Lubliner. *Plasticity Theory*. Dover Publications, 2008.
- [63] A. C. Luo, Y. Mou, and R. P. Han. A large anisotropic damage theory based on an incremental complementary energy equivalence model. *International Journal of Fracture*, 70:19–34, 1995.
- [64] Q. Ma and D. R. Clarke. Measurement of residual stresses in sapphire fiber composites using optical fluorescence. *Acta Metall. Mater.*, 41 (6):1817–1823, 1993.
- [65] Q. Ma and D. R. Clarke. Stress measurement in single-crystal and polycrystalline ceramics using their optical fluorescence. *Journal of the American Ceramic Society*, 76(6):1433–1440, 1993.
- [66] Q. Ma and D. R. Clarke. Piezospectroscopic determination of residual stresses in polycrystalline alumina. *Journal of American Ceramic Society*, 77:298–302, 1994.
- [67] Q. Ma, L. C. Liang, D. Clarke, and J. Hutchinson. Mechanics of the push-out process from *in-situ* measurement of the stress distribution along embedded sapphire fibers. *Acta metall. mater.*, 42 (10):3299–3308, 1994.

- [68] M. S. Majewski, C. Kelley, J. Lake, M. W. Renfro, W. Hassan, W. Brindley, and E. H. Jordan. Stress measurements via photoluminescence piezospectroscopy on engine run thermal barrier coatings. *Surface and Coatings Technology*, 206:2751–2758, 2012.
- [69] P. Marur, R. Batra, G. Garcia, and A. Loos. Static and dynamic fracture toughness of epoxy/alumina composite with submicron inclusions. *Journal of Materials Science*, 39(4):1437–1440, 2004.
- [70] C. Mi and D. Kouris. Nanoparticles and the influence of interface elasticity. *Theoret. Appl. Mech.*, 35:267–286, 2008.
- [71] D. Mollenhauer, E. Iarve, R. Kim, and B. Langley. Examination of ply cracking in composite laminates with open holes: A moiré interferometric and numerical study. *Composites Part A: Applied Science and Manufacturing*, 37:282–294, 2006.
- [72] T. Mori and K. Tanaka. Average stress in matrix and average elastic energy of materials with misfitting inclusions. *Acta metallurgica*, 21(5):571–574, 1973.
- [73] M. C. Munisso, S. Yano, W. Zhu, and G. Pezzotti. Spatially resolved piezospectroscopic characterizations for the validation of theoretical models of notch-root stress fields in ceramic materials. *Continuum Mechanics Thermodynamics*, 20:123–132, 2008.
- [74] R. Munro, G. Piermarini, S. Block, and W. Holzapfel. Model line shape analysis for the ruby R lines used for pressure measurement. *Journal of Applied Physics*, 57:165–169, 1985.
- [75] R. G. Munro. Evaluated material properties for a sintered  $\alpha$  alumina. *J. Am. Ceram. Soc.*, 80:1919–1928, 1997.
- [76] R. Musalek, J. Matejicek, M. Vilemova, and O. Kovarik. Non-linear mechanical behavior of plasma sprayed alumina under mechanical and thermal loading. *Journal of Thermal Spray Technology*, 19:422–428, 2010.
- [77] R. M. noz, V. Martínez, F. Sket, C. González, and J. LLorca. Mechanical behavior and failure micromechanisms of hybrid 3d woven composites in tension. *Composites: Part A*, 59:93–104, 2014.
- [78] G. Pezzotti. In situ study of fracture mechanisms in advanced ceramics using fluorescence and Raman microprobe spectroscopy. *J. Raman Spectrosc.*, 30:867–875, 1999.
- [79] G. J. Piermarini, S. Block, J. D. Barnett, and R. A. Forman. Calibration of the pressure dependence of the  $R_1$  ruby fluorescence line to 195 kbar. *Journal of Applied Physics*, 46:2774, 1975.
- [80] I. Piwoński and K. Soliwoda. The effect of ceramic nanoparticles on tribological properties of alumina sol-gel thin coatings. *Ceramics International*, 36(1):47–54, 2010.

- [81] S. Raghavan and P. Imbrie. The spectral analysis of R lines and vibronic sidebands in the emission spectrum of ruby using genetic algorithms. *Applied Spectroscopy*, 62:759–765, 2008.
- [82] S. N. Raja, A. C. K. Olson, K. Thorkelsson, A. J. Luong, L. Hsueh, G. Chang, B. Gludovatz, L. Lin, T. Xu, R. O. Ritchie, and A. P. Alivisatos. Tetrapod nanocrystals as fluorescent stress probes of electrospun nanocomposites. *Nano Letters*, 13:3915–3922, 2013.
- [83] E. F. Rejda, D. F. Socie, and T. Itoh. Deformation behavior of plasma-sprayed thick thermal barrier coatings. *Surface Coatings and Technology*, 113:218–226, 1999.
- [84] M. Salmi, F. Auslender, M. Bornert, and M. Fogli. Apparent and effective mechanical properties of linear matrix – inclusion random composites: Improved bounds for the effective behavior. *International Journal of Solids and Structures*, 49(10):1195–1211, 2012.
- [85] W. G. Sawyer, K. D. Freudenberg, P. Bhimaraj, and L. S. Schadler. A study on the friction and wear behavior of ptfe filled with alumina nanoparticles. *Wear*, 254:573–580, 2003.
- [86] J. Segurado and J. LLorca. Computational micromechanics of composites: the effect of particle spatial distribution. *Mechanics of materials*, 38(8):873–883, 2006.
- [87] A. Selcuk and A. Atkinson. Analysis of the  $Cr^{3+}$  luminescence spectra from thermally grown oxide in thermal barrier coatings. *Materials Science and Engineering A*, A335:147–156, 2002.
- [88] X. Shao, Q. Xue, W. Liu, M. Teng, H. Liu, and X. Tao. Tribological behavior of micrometer-and nanometer- $Al_2O_3$ -particle-filled poly (phthalazine ether sulfone ketone) copolymer composites used as frictional materials. *Journal of Applied Polymer Science*, 95(5):993–1001, 2005.
- [89] R. Shapery. A theory of mechanical behavior of elastic media with growing damage and other changes in structure. *Journal of the Mechanics and Physics of Solids*, 38:215–253, 1990.
- [90] X. A. Shen and Y. M. Gupta. Effect of crystal orientation on ruby R-line shifts under shock compression and tension. *Phys. Rev. B*, 48:2929, 1993.
- [91] A. Stevenson, A. Jones, and S. Raghavan. Characterization of particle dispersion and volume fraction in alumina-filled nanocomposites using photo-stimulated luminescence spectroscopy. *Polymer*, 43:923–929, 2011.
- [92] A. Stevenson, A. Jones, and S. Raghavan. Stress-sensing nanomaterial calibrated with photostimulated luminescence emission. *Nano Letters*, 11:3274, 2011.

- [93] G. Sundararajan and L. Rama Krishna. Mechanisms underlying the formation of thick alumina coatings through the MAO coating technology. *Surface and Coatings Technology*, 167(2):269–277, 2003.
- [94] G. Tandon and G. Weng. A theory of particle-reinforced plasticity. *Journal of Applied Mechanics*, 55(1):126–135, 1988.
- [95] H. Tomaszewski, J. Strzeszewski, L. Adamowicz, and V. Sergo. Indirect determination of the piezospectroscopic coefficients of ceria-stabilized tetragonal zirconia polycrystals. *J. Am. Ceram. Soc.*, 85:2855–2857, 2002.
- [96] J. Vegh. Alternative form for the pseudo-Voigt peak shape. *Review of Scientific Instruments*, 76:056107–1:3, 2005.
- [97] A. Voevodin and J. Zabinski. Nanocomposite and nanostructured tribological materials for space applications. *Composites Science and Technology*, 65:741–748, 2005.
- [98] K. S. Wan, S. Tochino, W. L. Zhu, S. Ohtsuka, and G. Pezzotti. Quantitative evaluation of probe response functions for Raman and fluorescence bands of single-crystalline and polycrystalline  $Al_2O_3$ . *Journal of Physics D: Applied Physics*, 43(20):205501, 2010.
- [99] G. Wertheim, M. Butler, K. West, and D. Buchanan. Determination of the gaussian and lorentzian content of experimental line shapes. *Review of Scientific Instruments*, 45:1369–1371, 1974.
- [100] P. A. Withey, V. S. M. Vemuru, S. M. Bachilo, S. Nagarajaiah, and R. B. Weisman. Strain paint: noncontact strain measurement using single-walled carbon nanotube composite coatings. *Nano Letters*, 12 (7):34970–3500, 2012.
- [101] Y. M. Wu, Z. Huang, Y. Zhong, and J. Wang. Effective moduli of particle-filled composite with inhomogeneous interphase: Part i - bounds. *Composites Science and Technology*, 64:1345–1351, 2004.
- [102] L. Xie, D. Chen, E. H. Jordan, A. Ozturk, F. Wu, X. Ma, B. M. Cetegen, and M. Gell. Formation of vertical cracks in solution-precursor plasma-sprayed thermal barrier coatings. *Surface Coatings and Technology*, 201:1058–1064, 2006.
- [103] Z. Yin, S. Tao, X. Zhou, and C. Ding. Microstructure and mechanical properties of  $Al_2O_3 - Al$  composite coatings deposited by plasma spray. *Applied Surface Science*, 254:1636–1643, 2008.
- [104] L. Zhang and W. Yu. On the constitutive relations for damaged elastoplastic materials coupling anisotropic damage and plasticity. In *AIAA SciTech, 55th AIAA/ASME/ASCE/AHS/SC Structures, Structural Dynamics, and Materials Conference*, 2014.
- [105] T. Zhu, A. Bushby, and D. Dunstan. Materials mechanical size effects: a review. *Materials Science and Technology*, 23(4):193–209, 2008.

- [106] R. W. Zimmerman. Elastic moduli of a solid containing spherical inclusions. *Mechanics of Materials*, 12(1):17–24, 1991.
- [107] S. C. Zunjarrao and R. P. Singh. Characterization of the fracture behavior of epoxy reinforced with nanometer and micrometer sized aluminum particles. *Composites Science and Technology*, 66(13):2296–2305, 2006.